STUDY OF INVISCID AND VISCOUS HYPERSONIC DISSOCIATING FLOWS OVER BLUNT BODIES USING THE CE/SE SCHEME

HERIBERTO SALDIVAR

Ph.D
The Hong Kong Polytechnic University

2017

THE HONG KONG
POLYTECHNIC UNIVERSITY
香港理工大學

Department of Mechanical Engineering

Study of Inviscid and Viscous Hypersonic Dissociating Flows Over Blunt Bodies Using the CE/SE Scheme

Heriberto Saldivar

A thesis submitted in partial fulfilment of the requirements for the degree of Doctor of Philosophy.

-

August 2016

Heriberto Saldivar
Study of Inviscid and Viscous Hypersonic Dissociating Flows Over Blunt Bodies Using the CE/SE Scheme
PhD. ThesisSupervisors: Chih-Yung Wen

The Hong Kong Polytechnic University
High-speed Thermo-fluid and MAV/UAV Laboratory (HTML)
Department of Mechanical Engineering
Faculty of Engineering
11 Yuk Choi Rd
Hong Kong

Certificate of Originality

I hereby declare that this thesis is my own work and that, to the best of my knowledge and belief, it reproduces no material previously published or written, nor material that has been accepted for the award of any other degree or diploma, except where due acknowledgement has been made in the text.

Heriberto Saldivar

Abstract

In this study, the hypersonic non-equilibrium flows over rounded nose geometries are numerically investigated by a robust conservation element and solution element (CE/SE) code, which is based on hybrid meshes consisting of triangular and quadrilateral elements. The dissociating and ionisation chemical reactions as well as the vibrational energy relaxation are taken into account. The stiff source terms are solved by an implicit trapezoidal method of integration. Comparison with laboratory and flight tests are provided to demonstrate the accuracy and reliability of the present CE/SE code in simulating hypersonic non-equilibrium flows.

Acknowledgement

There is a Chinese idiom that goes: "一日为师，终身为父"*(yi ri wei shi, zhong shen wei fu)* and I think it applies greatly to my relationship with Professor Wen Chih-Yung. Almost six years ago when I met him I was a kid extremely passionate about aerospace engineering, but without real experience or knowledge of it. He took my passion and thanks to his advise, teachings and patience he moulded me into a “Rocket Scientist”. Thanks to him I have not only learned how to be a better engineer, but through example I have learnt to be a better person. Thank you Professor.

I also would like to thank Dr. Shen Hua who masterfully helped me to understand the CE/SE method. I feel proud to be your first student.

The friendship and encouragement from my fellow graduate students and friends at the High-speed Thermo-fluid and MAV/UAV Laboratory (HTML) is also deeply appreciated as well as the support from the staff in the Department of Mechanical Engineering, in particular Lily Tam.

Finally, I would like to thank my amazing Patita for her support during this long journey that included sleepless nights, conferences that took us around the world, battles against mould, beach escapades, endless moments of joy and great discussions about our studies, life, physics and philosophy. I also would like to thank my parents Heriberto and Odette, you are the pillars that cement my life, and my sister Ody, who is an example of strength and integrity, for their unconditional support and love.

To conclude I would like to thank the financial support given by the Research Grants Council (RGC) of Hong Kong, by awarding me the Hong Kong PhD Fellowship Scheme (HKPFS).

Contents

List of Figures

List of Tables

Listings

Nomenclature

$\kappa_{Tr,V}$	Mixture thermal conductivity for each energy mode
μ	Viscosity
Ψ_r	Switch function for chemical reactions
Ψ_s	Switch function for simulation dimension
Ψ_v	Switch function for viscosity terms
ρ_b	Density on the body
ρ_e	Equilibrium density
ρ	Density
$\rho_i u_i^d$	i-species diffusion flux in the x direction
$\rho_i v_i^d$	i-species diffusion flux in the y direction
$\tau_{\theta\theta}$	Viscous stress component in the circumferential direction θ
τ_{ij}	Viscous stress components
$AIAA$	The American Institute of Aeronautics and Astronautics

CE/SE	Conservation Element / Solution Element Method
CST	Crew Space Transportation
D	Sphere Diameter
D_s	Mass diffusion coefficient for species s
E	Total energy of mixture
$E_{v_{m_i}}$	Vibrational energy of i-th molecule
h_s	Enthalpy of species s
Kn	Knudsen Number
m_i	i-th molecule
p	Pressure
q_i	Translational-rotational heat flux
q_i^v	Vibrational heat flux
R_u	Universal gas constant
$RAM - C$	Radio Attenuation Measurement Capsule
T	Translational Temperature
T_V	Vibrational Temperature
T_{wall}	Wall temperature
u	x-component of velocity

U_∞	Freestream condition
v	y-component of velocity
Y_n	n-th species mass fraction
CFL	Courant–Friedrichs–Lewy
CVCV	Coupled Vibration - Chemistry Vibration
FORTRAN	Formula Translation
OpenMP	Open Multi-Processing
STL	Standard Template Library
ZEHST	Zero Emission Hyper Sonic Transport

Introduction

1

> *“Following the light of the sun, we left the Old World.”*
>
> — **Cristoforo Colombo**
> Italian explorer, navigator and coloniser

1.1 Motivation

Humans have been driven to explore since the dawn of time. It is coded in our genes, we don’t like the unknown and by shining light into it, we had grown and pushed the boundaries of our social, scientific and technical limits, and then pushed even further. Starting from the 15th century we entered an age of discovery and constant expansion that reached its peak on July 16th, 1969. Then, we played safe and haven’t reached any further beyond earth’s atmosphere. Happily, over the last years, a renewed interest in manned missions to Mars has brought back our dreams of exploration leading to a renewed attention to the field of hypersonic aero-thermodynamics. Several space agencies, as well as private companies are currently designing hypersonic vehicles (CST-100 Starliner by Boeing, Orion by Lockheed Martin, ZHEST by Airbus Aerospace and, Dragon by Space Exploration Technologies Corporation) that, hopefully, will become the next generation of space vehicles.
The atmosphere surrounding Earth protects and supports life on the planet, but it also makes space flight more difficult. It is said, only half-jokingly, that getting to orbit is halfway to anywhere because of the considerable amount of energy necessary to go beyond the gravity well of this planet. Generally overlooked, however, is just how difficult it is to return from orbit[1]. All of the energy expended to get to orbit dissipates on the way back to Earth, usually in the form of extreme heating. When the space vehicle enters the atmosphere at an orbital speed, a detached bow shock forms in front of its blunt nose and the temperature behind the shock, especially in the stagnation region, can reach high levels, due to the conversion of kinetic flow energy into thermal energy by strong shock compression. At hypersonic speeds, the massive amount of kinetic energy leads gas molecule dissociation and other

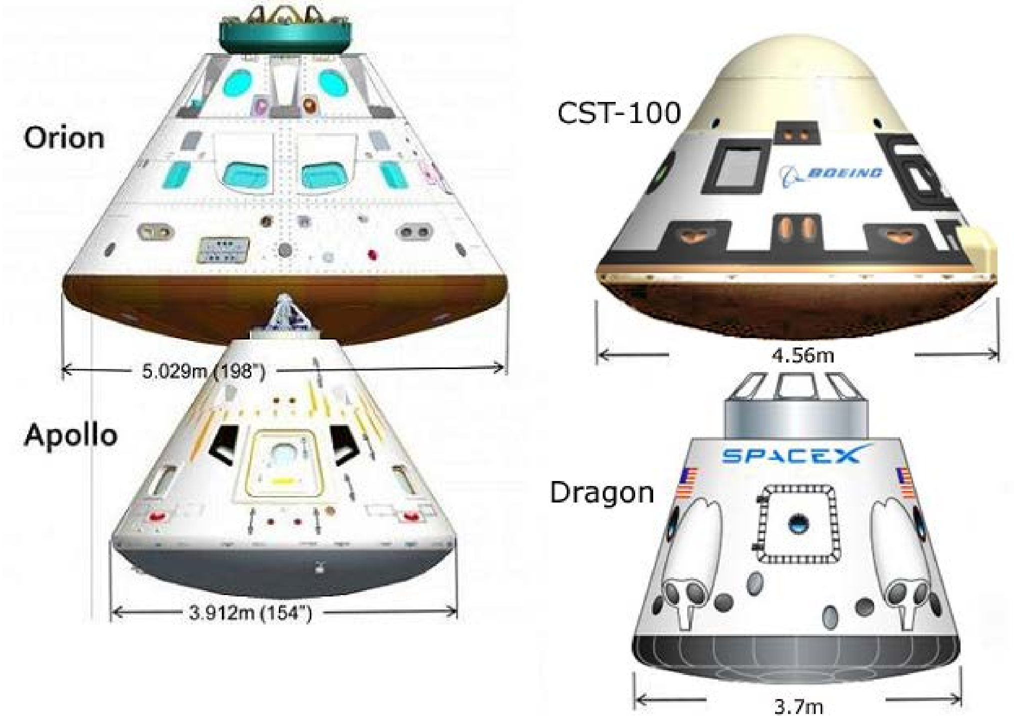

Fig. 1.1.: Apollo capsule next to some designs of the next generation of space capsules.

real gas effects of hypersonic flows. Consequently, the air can no longer be treated as a perfect gas and the dissociative non-equilibrium phenomenon complicates the flow physics. If the speed is high enough, the presence of ionisation in the shock layer, providing a large number of free electrons, also occurs. [2] These free electrons absorb radio-frequency radiation and cause radio blackout (For the Apollo 13 mission, communication blackout lasted around six minutes). Thanks to satellites orbiting the earth, communications blackout is not the problem it used to be, nevertheless, is still a very real problem encountered in atmospheric reentry, mainly because it's not confined to earth's atmosphere. Past missions to mars have shown us that this problem also occurs in CO_2 environments, therefore it's of high importance to accurately predict the electron number density in the plasma sheath around any capsule.[3]

1.2 Reentry Flow Regime

Space vehicles reentering the Earth's atmosphere have typical values for the entry velocity between 7,000 and 12,000 km/s and the associated Mach numbers range between 10 and 50. As the spacecraft crosses the atmo-

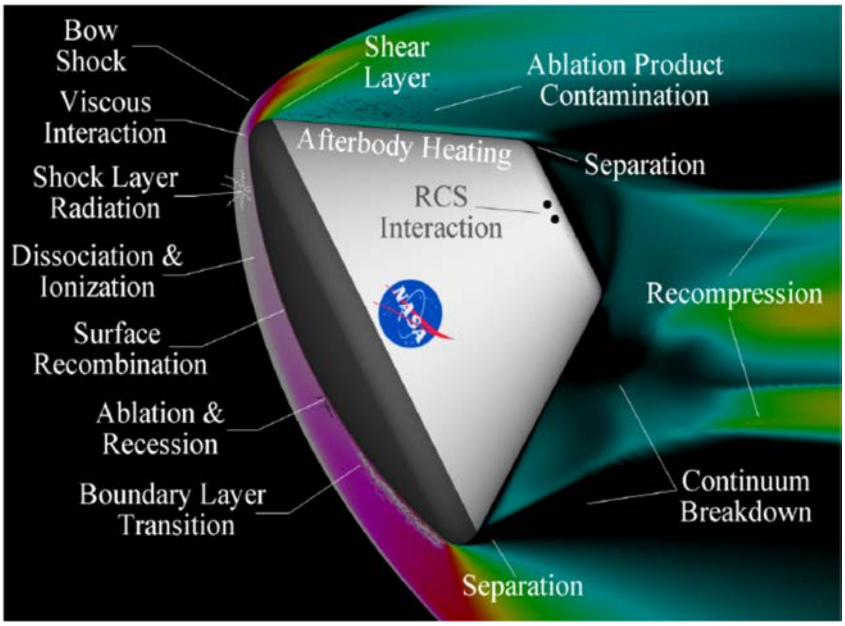

Fig. 1.2.: Schematic of the flow field surrounding a space capsule during reentry.

sphere, it undergoes different flow regimes. The Knudsen number gives a basic criterion that determines the flow regime(collision-less, transitional or continuum) as follows:

$$Kn = \frac{\lambda}{l}$$

where λ is the mean free path traveled by molecules between collisions and l is a characteristic length of the body. A flow is defined in the continuum regime when the Knudsen number tends to zero. On the other hand, a flow is defined in the free molecular flow as the Knudsen number tends to infinity. At highest altitudes, the interaction of the vehicle with the atmospheric air is characterized by the free molecular flow. In this regime, the molecules of the environment collide with the vehicle surface, interact with the surface and are reflected from the surface. Moreover, collisions of reflected molecules with incoming molecules from the free-stream are not frequently in this flow regime.

As the vehicle enters deeper into the Earth's atmosphere, the mean free path between incoming free-stream molecules decreases and collisions between molecules reflected from the vehicle surface and the molecules incoming from the free-stream can no longer be ignored. As a result, the flow in this condition defines the transition flow regime. In the transition flow regime, the contribution of aerodynamic forces and heat flux to the vehicle surface start to increase rapidly with decreasing altitude, causing large changes in the aerodynamic characteristics of the vehicle when compared with those

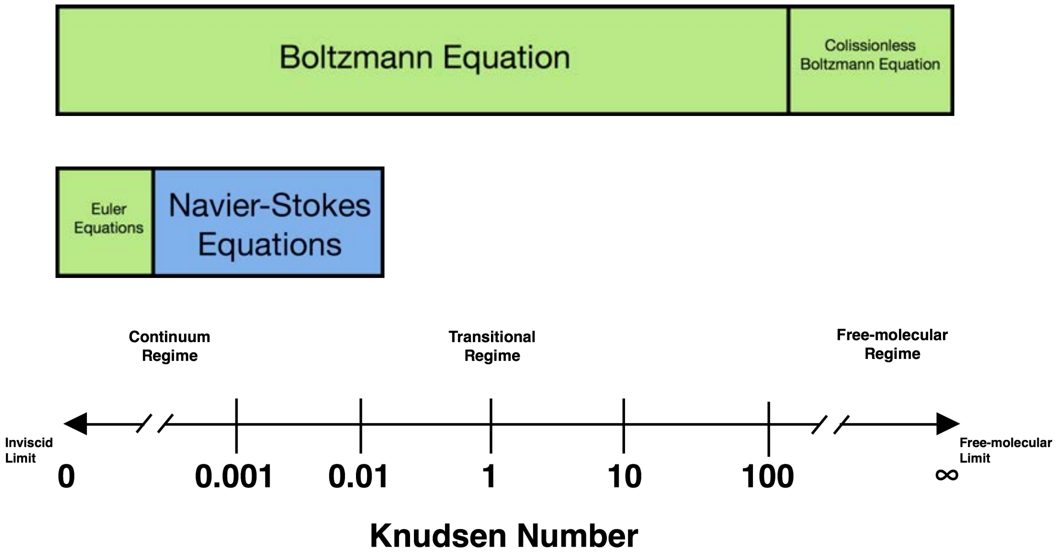

Fig. 1.3.: The Knudsen number limits on the mathematical models.

observed in the free molecular flow. As the vehicle continues to deepen into the atmosphere, it finally reaches the continuum flow regime. Here, the flow around the vehicle is treated by a macroscopic model that considers the air as a continuum state, and the description of the flow is made in terms of spatial and temporal variations of the primary properties, such as velocity, pressure, density, and temperature.

The development of promising future generation space vehicles requires a complete and detailed knowledge of their aero-thermodynamics along the complete descent trajectory and due to the extreme flow conditions, experimental approaches to study such hypersonic flows are difficult in general, not to mention expensive. Therefore, is essential to develop a reliable, efficient and accurate numerical method.

1.3 Review of Related Works

Variable numerical methods have been applied to simulating the hypersonic non-equilibrium flows. However, the conservation element and solution element (CE/SE) method is implemented to investigate such problems for the first time, to the best of the current author's knowledge. The CE/SE method is a novel numerical framework, which is proposed by Chang and coworkers[4, 5, 6, 7] to solve hyperbolic conservation equations. Since its inception in 1991, it has been used to obtain highly accurate numerical solutions for 1D, 2D, and 3D flow problems involving shocks, contact discontinuities, vortices, MHD, etc. [8, 4, 5, 6] The original CE/SE schemes were constructed on triangular elements in two dimensions (2D) and tetrahedrons in three dimensions (3D), and extended to quadrilateral elements in 2D and hexahedral elements in 3D later. Nevertheless, the CE/SE scheme used in present study is that implemented on a hybrid mesh consisting of triangular elements and quadrilateral elements[9]. The author has presented some numerical results about hypersonic non-equilibrium flows in the 19th & 20th AIAA International Space Planes and Hypersonic Systems[10, 11] and Technologies Conference and the 30th International Symposium on Shock Waves[12]

1.4 Scope of Thesis

In the present work, the inviscid CE/SE code based on hybrid meshes consists of triangular and quadrilateral elements[9] is used and extended to solve hypersonic chemical reacting non-equilibrium flows.

Both chemical dissociation and vibrational energy relaxation are taken into account. The code is capable of using a CVCV[13] model developed by Knab and a two temperature chemical kinetic model developed by Park[14]. For Nitrogen flows, only two species (N_2 and N) and two chemical reactions are used, for CO_2 and airflows, five species ((CO_2, O_2, CO, C, and O) and (N_2, O_2, NO, N, and O) respectively) and seventeen reactions are considered. Several cases of nitrogen, air, carbon dioxide, ionised, non-ionised, viscous and inviscid flows, are provided to demonstrate the accuracy and reliability of the method regarding non-equilibrium flows. Furthermore, the flow features of hypersonic flows are analysed in detail through the extensive numerical results.

The two main tasks of this work are:

(1) development and validation of software tools for numerical investigations of chemically reacting hypersonic flows using CE/SE methods;

(2) study of aero-thermodynamics of promising space vehicles, including those with leading edges of small-radius bluntness, with allowance for non-equilibrium physical and chemical processes and analysis of their influence

on distributed (pressure and heat flux) and integral (drag force, lift force, heat transfer, pitching moment, etc.) aero-thermodynamic characteristics.

This thesis is divided into six chapters including this introduction, an outline of it is as follows:

Chapter 2 - Physical Model and Governing Equations

This chapter will start with a general description of hypersonic and high-temperature gas dynamics, then it will present the conservation equations used, the viscous terms implemented and the thermodynamic properties. The chapter will conclude with a detailed explanation and comparison of the chemical models used, CVCV and the Two-Temperature model.

Chapter 3 - The space-time CE/SE Scheme

This chapter details the numerical method used. First an introduction regarding the CE/SE method, the motivations, and its advantages. Secondly, an explanation of the CE/SE scheme based on hybrid meshes. Thirdly a detailed account of the implementation of boundary conditions, including both inviscid and viscous wall boundary conditions. Finally, the semi-implicit algorithm used to solve the stiff source term is presented.

Chapter 4 - Implementation

This chapter gives a general overview of the code, explains the CFL conditions, the parallelisation strategies and the equipment used to run the code.

Chapter 5 - Results

This chapter presents code validation efforts using available experimental, numerical and flight data for space capsules. The fist part will deal with inviscid flows, including Nitrogen, Air and CO_2, around spheres. The second part will present results for viscous flows around spheres and space capsules.

Chapter 6 - Conclusion

Conclusions and suggestions for further research are summarised in this chapter.

2

Physical Model and Governing Equations

> *Underpinning everything... are the laws of physics.*
>
> — **Paul Davies**
> (Theoretical physicist, cosmologist and astro-biologist)

2.1 Introduction

Usually, shock wave propagation problems are described by classic Navier-Stokes equations or inviscid Euler equations and the collision between the gas molecules is neglected so that the gas can be treated as a perfect gas. However, because the collision frequency between the particles is very high in hypersonic flows as a consequence of the high gas density and temperature between the shock and body, dissociation, recombination, ionisation and other real gas effects occur. In addition, the vibrational energy plays an important role and should be considered. Therefore, more terms have to be included into the classic Navier-Stokes equations to accurately describe these phenomena. With this in mind, the chemical reactions and the vibrational energy relaxation models are taken into consideration in the present study.

2.2 Conservation Equations

The general form of the equations governing 2D reactive non-equilibrium flows with n_s species can be written as:

$$\frac{\partial U}{\partial t}+\frac{\partial F(U)}{\partial x}+\frac{\partial G(U)}{\partial y}-\Psi_v\left(\frac{\partial F_v(U)}{\partial x}+\frac{\partial G_v(U)}{\partial y}\right)=\Psi_s S(U)+\Psi_r R(U) \quad (2.1)$$

where $U = \left[\rho_1, \ldots, \rho_{n_s}, \rho u, \rho v, E, E_{v_{m_1}}, \ldots, E_{v_{m_s}}\right]^T$ is the conservative quantity vector. F and G are the convection fluxes which are given by:

$$F = \left[\rho_1 u, \ldots, \rho_{n_s} u, \rho u^2 + p, \rho u v, (E+p)u, E_{v_{m_1}} u, \ldots, E_{v_{m_s}} u\right]^T \tag{2.2}$$

and

$$G = \left[\rho_1 v, \ldots, \rho_{n_s} v, \rho u v, \rho v^2 + p, (E+p)v, E_{v_{m_1}} v, \ldots, E_{v_{m_s}} v\right]^T \tag{2.3}$$

The viscid fluxes F_v and G_v can be expressed in the following form:

$$F_v = \begin{bmatrix} -\rho_1 u_1^d \\ \vdots \\ -\rho_{n_s} u_{ns}^d \\ \tau_{xx} \\ \tau_{xy} \\ \tau_{xx} u + \tau_{xy} v - q_x - q_x^v - \sum_{s=1}^{n_s} \rho_s u_s^d h_s \\ -q_x^v - \rho_{m_1} u_{m_1}^d e_{m_1}^v \\ \vdots \\ -q_x^v - \rho_{m_s} u_{m_s}^d e_{m_s}^v \end{bmatrix} \tag{2.4}$$

and

$$G_v = \begin{bmatrix} -\rho_1 v_1^d \\ \vdots \\ -\rho_{n_s} v_{ns}^d \\ \tau_{xy} \\ \tau_{yy} \\ \tau_{xy} u + \tau_{yy} v - q_y - q_y^v - \sum_{s=1}^{n_s} \rho_s v_s^d h_s \\ -q_y^v - \rho_{m_1} v_{m_1}^d e_{m_1}^v \\ \vdots \\ -q_y^v - \rho_{m_s} v_{m_s}^d e_{m_s}^v \end{bmatrix} \tag{2.5}$$

S is the source term caused by symmetry (y being the axis of symmetry) and R is that caused by chemical reactions and energy relaxation. They can be expressed in the following form

$$S = -\frac{1}{y}\begin{bmatrix} \rho_1 v \\ \vdots \\ \rho_{n_s} v \\ \rho u v \\ \rho v^2 \\ (E+p)v \\ E_{v_{m_1}} v \\ \vdots \\ E_{v_{m_s}} v \end{bmatrix} + \frac{\Psi_v}{y}\begin{bmatrix} -\rho_1 v_1^d \\ \vdots \\ -\rho_{n_s} v_{n_s}^d \\ \tau_{xy} \\ \tau_{yy} - \tau_{\theta\theta} \\ \tau_{xy} u + \tau_{yy} v - q_y - q_y^v - \sum_{s=1}^{n_s} \rho_s v_s^d h_s \\ -q_y^v - \rho_{m_1} v_{m_1}^d e_{m_1}^v \\ \vdots \\ -q_y^v - \rho_{m_s} v_{m_s}^d e_{m_s}^v \end{bmatrix} \tag{2.6}$$

$$R = \begin{bmatrix} \dot{\omega}_1 \\ \vdots \\ \dot{\omega}_{n_s} \\ 0 \\ 0 \\ 0 \\ \dot{\omega}_{v_{m_1}} \\ \vdots \\ \dot{\omega}_{v_{m_s}} \end{bmatrix} \tag{2.7}$$

In these expressions,$\rho_1 \ldots \rho_{n_s}$ are the species densities, u and v are the bulk velocity components, E and $E_{v_{m_i}}$ are the total and the i-th molecule vibrational energy per unit volume of mixture, p is the pressure, τ_{ij} are the viscous stress components, q_i and q_i^v, are the translational-rotational and vibrational heat fluxes in the i-th direction. Moreover, h_s is the species enthalpy and $-\rho_i u_i^d$ and $-\rho_i v_i^d$ are the i-species diffusion flux in the x and y direction respectively, $\dot{\omega}_s$ is the mass production/destruction term for chemical species s and $\dot{\omega}_{v_{m_i}}$ is the i-th molecule vibrational energy source term. Finally, Ψ_v is a switch function with values of 0 and 1 for inviscid and viscid problems, respectively; Ψ_s is a switch function and has values of 0 and 1 for two-dimensional and axisymmetric problems, respectively; while Ψ_r is also a switch function and has values of 0 and 1 for chemical reacting and frozen gas cases, respectively.

2.3 Viscous Terms

Under stokes' hypothesis of negligible bulk viscosity effects, the viscous stresses can be expressed as follows:

$$\tau_{xx} = 2\mu\frac{\partial u}{\partial x} - \frac{2}{3}\mu\left(\frac{\partial u}{\partial x} + \frac{\partial v}{\partial y} + \Psi_s\frac{v}{y}\right) \tag{2.8}$$

$$\tau_{yy} = 2\mu\frac{\partial v}{\partial y} - \frac{2}{3}\mu\left(\frac{\partial u}{\partial x} + \frac{\partial v}{\partial y} + \Psi_s\frac{v}{y}\right) \tag{2.9}$$

$$\tau_{xy} = \tau_{yx} = \mu\left(\frac{\partial u}{\partial x} + \frac{\partial v}{\partial y}\right) \tag{2.10}$$

$$\tau_{\theta\theta} = -\frac{2}{3}\mu\left(\frac{\partial u}{\partial x} + \frac{\partial v}{\partial y} - 2\frac{v}{y}\right) \tag{2.11}$$

Here, $\tau_{\theta\theta}$ is the viscous stress component in the circumferential direction θ. The i-species diffusion flux are assumed to be proportional to the gradients of the mass fractions

$$\frac{\partial c_s}{\partial x} \tag{2.12}$$

and

$$\rho_i v_i^d = -\rho D_s\frac{\partial c_s}{\partial y} \tag{2.13}$$

The heat fluxes appeared in the viscid fluxes are modeled according to Fourier's law as

$$q_{Tr,V} = -\kappa_{Tr,V}\nabla T_{Tr,V} \tag{2.14}$$

where $-\kappa_{Tr,V}$ are the mixture thermal conductivity for each energy mode.

2.4 Thermodynamics Properties

The mixture pressure p is obtained using Dalton's law of partial pressures and the perfect gas law for each species. Thus,

$$p = \sum_{s=1}^{n_s} \rho_s \frac{R_u}{M_s} T \tag{2.15}$$

where R_u is the universal gas constant.

The combined energy in the translational and rotational modes is obtained by subtracting the vibrational, kinetic, and chemical energies from the total energy. Assuming that the rotational energy modes are in equilibrium with the translational modes, the caloric equation of state for mass-averaged gas is derived as

$$\sum_{s=1}^{n_s} \rho_s c_s^v T = E - \sum_{s=1}^{m_s} E_{v_{m_s}} - \frac{1}{2}\rho(u^2 + v^2) - \sum_{s=1}^{n_s} \rho_s h_s \tag{2.16}$$

where, c_s^v and h_s are the translational-rotational specific heat at constant volume and species enthalpy, respectively. The translational-rotational temperature, T, can be determined using Eq. 2.16 accordingly.

The translational-rotational specific heat at constant volume, c_s^v, is given by

$$c_s^v = c_s^t + c_s^r \tag{2.17}$$

We asume that the translational and rotational specific heat at constant volume are constant and given by:

$$c_s^t = \frac{3}{2}\frac{R_u}{M_s} \tag{2.18}$$

and

$$c_s^r = \begin{cases} \frac{R_u}{M_s} & \text{for molecules,} \\ 0 & \text{for atoms and electrons.} \end{cases} \tag{2.19}$$

The species vibrational energy per unit mass is modeled using a harmonic oscillator as:

$$e_{v,s} = \begin{cases} \frac{R_u}{M_s} \frac{\theta_{v_s}}{exp(\theta_{v_s}/T_v)-1} & \text{for molecules,} \\ 0 & \text{for atoms and electrons.} \end{cases} \tag{2.20}$$

where θ_{v_s} is the species characteristic vibrational temperature.

The vibrational specific heat at constant volume can be calculated as

$$Cv_{v,s} = \begin{cases} \frac{R_u}{M_s} \frac{(\theta_{v_s}/T_v)^2 exp(\theta_{v_s}/T_v)}{[exp(\theta_{v_s}/T_v)-1]^2} & \text{for molecules,} \\ 0 & \text{for atoms and electrons.} \end{cases} \tag{2.21}$$

The vibrational-electron-electronic energy per unit mass of the species is given by

$$e_{v_e,s} = \begin{cases} e_{v,s} & \text{for molecules and atoms} \\ c_e^t T_v & \text{for electrons.} \end{cases} \tag{2.22}$$

The i-t molecule vibrational energy is given by

$$E_{v_{m_i}} = \rho_i e_{v_e,i} \tag{2.23}$$

and the species enthalpies, h_s are given by

$$h_s = \begin{cases} R_s T & \text{for molecules and atoms} \\ R_e T_v & \text{for electrons.} \end{cases} \tag{2.24}$$

2.5 Transport Properties

At low temperatures the viscosity can be estimated from the well know Sutherland's law, however, at high temperatures the transport properties of gasses significantly differ and to accurately obtain them, we use Wilke's mixing rule [15]

$$\mu = \sum_s \frac{X_s \mu_s}{\phi_s} \tag{2.25}$$

$$\kappa = \sum_s \frac{X_s \kappa_s}{\phi_s} \tag{2.26}$$

where X_s is the species molar fraction, μ_s is the species coefficient of viscosity and κ_s is the species thermal conductivity. The term ϕ_s is given by

$$\phi_s = \sum_r X_r \left[1 + \sqrt{\frac{\mu_s}{\mu_r}} \left(\frac{M_r}{M_s}\right)^{1/4}\right]^2 \left[\sqrt{8\left(1 + \frac{M_s}{M_r}\right)}\right]^{-1} \tag{2.27}$$

The species viscosities are calculated using Blottner's curve fits[16]

$$\mu_s = 0.1exp[(A_s lnT + B_s)lnT + C_s] \tag{2.28}$$

where A_s, B_s and C_s are constants determined for each species[17]. The species thermal conductivities are determined using Eucken's relation[18] as

$$\kappa_{tr,s} = \frac{5}{2}\mu_s c_s^t + \mu_s c_s^r \tag{2.29}$$

2.6 Chemical Model

Chemical model plays an important role in the accurate description of composition of the high-temperature gas. Several investigators have discussed the problems of chemical non-equilibrium in the shock layers over vehicles flying at high speeds and high altitudes in Earth's atmosphere.[19] For Nitrogen flows, because the ionisation is neglected, only two species are used (N_2 and N), the considered chemical reactions are

$$N_2 + M \leftrightharpoons N + N + M$$

where, M is the collision partner and can represent either molecular or atomic nitrogen. For air flows, five chemical species are used (N_2, O_2, NO, N and O). The chemical reactions included in the current work are listed as follows:

$$\begin{gathered} N_2 + M \leftrightharpoons N + N + M \\ O_2 + M \leftrightharpoons O + O + M \\ NO + M \leftrightharpoons N + O + M \\ N_2 + O \leftrightharpoons NO + N \\ NO + O \leftrightharpoons O_2 + N \end{gathered}$$

For carbon dioxide flows, the five primary chemical species CO_2, O_2, CO, C and O are considered. The used chemical reactions are listed as follows:

$$\begin{gathered}
CO_2 + M \leftrightharpoons CO + O + M \\
CO + M \leftrightharpoons C + O + M \\
O_2 + M \leftrightharpoons O + O + M \\
CO_2 + O \leftrightharpoons O_2 + CO \\
CO + O \leftrightharpoons O_2 + C
\end{gathered}$$

For ionized airflows, eleven chemical species are used (N_2, O_2, NO, N, O, N_2^+, O_2^+, NO^+, N^+, O^+ and e^-). The chemical reactions included in the current work are listed as follows:

$$\begin{gathered}
\text{Dissociation reactions} \\
N_2 + M \leftrightharpoons N + N + M \\
O_2 + M \leftrightharpoons O + O + M \\
NO + M \leftrightharpoons N + O + M \\
NO \text{ exchange reactions} \\
N_2 + O \leftrightharpoons NO + N \\
NO + O \leftrightharpoons O_2 + N \\
\text{Associative ionisation reactions} \\
N + O \leftrightharpoons NO^+ + e^- \\
O + O \leftrightharpoons O_2^+ + e^- \\
N + N \leftrightharpoons N_2^+ + e^-
\end{gathered}$$

$$\begin{gathered}
\text{Electron-impact ionisation reactions} \\
O + e^- \leftrightharpoons O^+ + 2e^- \\
N + e^- \leftrightharpoons N^+ + 2e^- \\
\text{Charge exchange reactions} \\
NO^+ + O \leftrightharpoons N^+ + O_2 \\
O_2^+ + N \leftrightharpoons N^+ + O_2 \\
O^+ + NO \leftrightharpoons N^+ + O_2 \\
O_2^+ + N_2 \leftrightharpoons N_2^+ + O_2 \\
O_2^+ + O \leftrightharpoons O^+ + O_2 \\
NO^+ + O_2 \leftrightharpoons O_2^+ + NO \\
NO^+ + O \leftrightharpoons O_2^+ + N \\
O^+ + N_2 \leftrightharpoons N_2^+ + O \\
NO^+ + N \leftrightharpoons N_2^+ + O
\end{gathered}$$

The mass production/destruction term for chemical species $\dot{\omega}_s$ in Eq.(2.7) is formulated as

$$\dot{\omega}_s = M_s \sum_{r=1}^{n_r} (\beta_{sr} - \alpha_{sr}) \left[k_{fr} \prod_{j=1}^{n_s} \left(\frac{\rho_j}{M_j} \right)^{\alpha_{jr}} - k_{br} \prod_{j=1}^{n_s} \left(\frac{\rho_j}{M_j} \right)^{\beta_{jr}} \right] \tag{2.30}$$

where α and β are the stoichiometric coefficients of species s in reaction r. The forward and backward reaction rates are affected by the level of non-equilibrium in the flow.
To account for that effect, Park's two-temperature model[14] and CVCV[13] model can be used.

2.6.1 Two Temperature Model

For fast results, certain computer codes for calculating the non-equilibrium reacting flow use the one-temperature model, which assumes that all of the internal energy modes of the gaseous species are in equilibrium with the translational mode.[20, 21] It has been pointed[22] out that such a one-temperature description of the flow leads to a substantial overestimation of the rate of equilibration when compared with the existing experimental data. A three-temperature chemical- kinetic model has been proposed by Lee[23] to describe the relaxation phenomena correctly in such a flight regime. However, the model is complex and requires many chemical rate parameters that are yet unknown. As a compromise between the three-temperature chemical-kinetic and the conventional one-temperature model, a two-temperature chemical-kinetic model has been developed by Park[14]. The model uses one temperature, T, to characterise the translational energy of the atoms and molecules and the rotational energy of the molecules, and another temperature, T_v , to characterise the vibrational energy of the molecules, translational energy of the electrons, and electronic excitation energy of atoms and molecules. The forward reaction rates coefficients k_{fr} can be calculated by the Arrhenius' law as

$$k_{fr}(T) = A_{fr} T_c^{\eta_r} exp(-\theta_r / T_c) \tag{2.31}$$

where the control temperature, T_c, can be the translational temperature (T), the vibrational temperature (T_v) or an geometrical mean temperature, $\bar{T} = T^s T_v^{s-1}$, where s is between 0.5-0.7, no clear advantage of 0.7 over the

0.5 has yet been demonstrated[24]. The backward reaction rates depend only on the translational temperature as

$$k_{br}(T) = \frac{k_{fr}(T)}{K_{eq}(T)} \tag{2.32}$$

For air and nitrogen flows, the equilibrium constants can be obtained from

$$K_{eq}(T) = exp\left[A_1\left(\frac{T}{10,000}\right) + A_2 + A_3 ln\left(\frac{10,000}{T}\right) + A_4\left(\frac{10,000}{T}\right) + A_5\left(\frac{10,000}{T}\right)^2\right] \tag{2.33}$$

where the coefficients A_i are a function of the local number density. For carbon dioxide flows, due to a lack of information regarding the coefficients A_i, the equilibrium constants are obtained from

$$K_{eq}(T) = \left(\frac{p_o}{RT_{tr}}\right)^{v_r} exp\left(-\sum_s(\beta_{s,r} - \alpha_{s,r})\left[\frac{\hat{h}_s}{RT_{tr}} - \frac{\hat{s}_s}{R}\right]\right) \tag{2.34}$$

where p_o is a reference pressure set to 1 bar and $v_r = \sum_s(\beta_{s,r} - \alpha_{s,r})$. The normalized enthalpy and entropy are obtained from curve fits of the form

$$\frac{\hat{h}_s}{RT_{tr}} = -\frac{B_1}{T^2} + B_2\frac{lnT}{T} + B_3 + B_4\frac{T}{2} + B_5\frac{T^2}{3} + B_6\frac{T^3}{4} + B_7\frac{T^4}{5} + \frac{B_8}{T} \tag{2.35}$$

$$\frac{\hat{s}_s}{R} = -\frac{B_1}{2T^2} + B_2\frac{1}{T} + B_3 lnT + B_4 T + B_5\frac{T^2}{2} + B_6\frac{T^3}{3} + B_7\frac{T^4}{4} + B_9 \tag{2.36}$$

where the coefficients B_i are a function of temperature. The constants in Eqs. 2.33-2.36 can be found from different sources[25, 26, 27].

2.6.2 CVCV

The first quantitative multi-temperature approach based on state selective rates together with the Boltzmann distribution for internal energy was proposed by Hammerling[28] in 1959, Treanor and Marrone[29] extended this model, including the reverse effect that dissociation exerts on the vibrational relaxation rate. To describe the influence of vibration on exchange reactions and associative ionisation reactions as well as the coupling of the reactions on vibrational energy, the CVCV model was proposed by Knab.[13] In Knab's model, the thermal equilibrium reaction rates are modified using an efficiency function $\varphi(T, T_v)$ as follows[30]

$$k(T, T_v) = \varphi(T, T_v) k_{eq}(T) \tag{2.37}$$

The efficiency function is calculated disregarding anharmonicity effects, using the trunked harmonic oscillator model,

$$Q(T, E) = \frac{1 - e^{-E/RT}}{1 - e^{-\theta_v/T}} \tag{2.38}$$

where θ_v and E are the characteristic vibrational temperature and the truncated maximum energy respectively. The efficiency function is computed as

$$\varphi(T, T_v) = X_1 \frac{X_2}{X_3} \tag{2.39}$$

where

$$\begin{aligned} X_1 &= \tfrac{Q(T,E_d)}{Q(Tv,E_d)}; \\ X_2 &= e^{-\alpha E_a/RT} Q(\Gamma, \alpha E_a) + Q(T^0, E_d) - Q(T^0, \alpha E_a) \\ X_3 &= e^{-\alpha E_a/RT} Q(-U, \alpha E_a) + Q(T^*, E_d) - Q(T^*, \alpha E_a) \end{aligned}$$

E_d is the dissociation energy of the molecule, E_a is the activation Energy for the reaction, α is a coefficient that determines the fraction of energy required for each reaction and is set to 0.7-0.8.
T^0, T^*, Γ and U are temperatures defined as,

$$\begin{aligned} \tfrac{1}{\Gamma} &= \tfrac{1}{T_v} - \tfrac{1}{T} - \tfrac{1}{U} \\ U &= \tfrac{E_d}{5R} \\ \tfrac{1}{T^0} &= \tfrac{1}{T_v} - \tfrac{1}{U} \\ \tfrac{1}{T^*} &= \tfrac{1}{T} - \tfrac{1}{U} \end{aligned}$$

2.7 Relaxation Model

The vibrational energy source term $\dot{\omega}_v$ in Eq.2.7 is given by

$$\dot{\omega}_v = S_{c-v} + S_{t-v} + S_{h-e} + S_{e-i} + S_{v-v} \tag{2.40}$$

where S_{c-v} is the vibrational-electron-electronic energy added or removed by chemical reactions modelled using a non-preferential model where it is assumed that molecules are created or destroyed at the average vibrational energy, hence

$$S_{c-v} = \sum_s \dot{\omega}_s (e_{v,s} + e_{el,s}) \tag{2.41}$$

S_{h-e} is the energy transfer between heavy particles and electrons,

$$S_{h-e} = 3R_u \rho_e (T - T_v) \sqrt{\frac{8R_u T_v}{\pi M_e}} \sum_{s \neq e} \frac{\rho_s N_a}{M_s^2} \sigma_s \tag{2.42}$$

S_{e-i} is the energy removed from free electrons during impact ionisation reactions,

$$S_{e-i} = \hat{I}_N M_{N^+} \dot{\omega}_{N^+,iir} + \hat{I}_O M_{O^+} \dot{\omega}_{O^+,iir} \tag{2.43}$$

for Air flows. S_{v-v} is to account for vibration-vibration energy exchange[13] given by

$$S_{v-v} = N_a \sqrt{\frac{8R_u T}{\pi M_u}} \sum_{s \neq i}^{m_s} 0.01 \sigma_s \frac{c_i c_s}{\sqrt{\mu_{is}}} \left(\frac{e^*_{v,i}(T)}{e^*_{v,r}(T)} e_{v,r}(T_v) - e_{v,i}(T_v) \right) \tag{2.44}$$

where, σ_s is the limiting cross section, $c_{i,s}$ are the i-th and s-th species mass fractions and μ_{is} is given by $\mu_{is} = (M_i M_s)/(M_i + M_s)$.

S_{t-v} is the energy exchange rate between the vibrational and translational modes modelled by the Landau-Teller model[18] as

$$S_{t-v} = \sum_{s=1}^{n_s} \rho_s \frac{e^*_{v,s}(T) - e_{v,s}(T_v)}{\tau_s} \tag{2.45}$$

where

$$\tau_s = \langle \tau_s \rangle + \tau_{ps} \tag{2.46}$$

The molar averaged Landau-Teller relaxation time, $\langle \tau_s \rangle$ [23] is written as

$$\langle \tau_s \rangle = \frac{\sum_{r=1}^{n_s} X_r}{\sum_{r=1}^{n_s} X_r / \tau_{sr}} \tag{2.47}$$

where, X_r is the molar fraction of species r. The Landau-Teller relaxation time between species s and r, τ_{sr}, can be modelled using curve fits given by Millikan and White[31] for vibrational relaxation as

$$\tau_{sr} = \frac{101,325}{p} exp[A_{sr}(T^{1/3} - B_{sr}) - 18.42] \tag{2.48}$$

The values for A_{sr} and B_{sr} are derived by using tabulated data from Hash et al [32]. It is known that Millikan and White curve underestimate the relaxation time at high temperatures. Park[27] corrected this problem by limiting the collision cross section and adding the corresponding limiting relaxation time

$$\tau_{ps} = \frac{1}{\sigma_s a_s N} \tag{2.49}$$

to fix this problem, where N is the number density of the mixture, as is the average molecular speed of the species which is given by

$$a_s = \sqrt{\frac{8R_u T}{\pi M_s}} \tag{2.50}$$

and σ_s is the limiting cross section defined as

$$\sigma_s = 10^{-20}\left(\frac{50,000}{T}\right)^2 m^2 \tag{2.51}$$

The above energy relaxation model is only applicable for nitrogen and air flows. For CO_2 flows, results of Camac[33] indicate that due to strong resonance coupling between the different vibrational modes of CO_2 the three vibrational modes of CO_2 relax at the same rate, and the vibrational relaxation time of CO_2 can be modelled by

$$\tau_{CO_2} = \frac{1}{p_{atm}} exp(36.5T^{-1/3} - 17.71) \tag{2.52}$$

where p_{atm} is pressure in atmospheres.

3

The space-time CE/SE Scheme

> ”…wibbily wobbly timey wimey…stuff*
>
> — **The** 10^{th} **Doctor (Dr.Who)**
> about space and time

3.1 Introduction

Because in the field of computational fluid dynamics (CFD) a conflict between stability and numerical accuracy is one that affects most of the established methods, Chang and To[4] developed the space-time conservation element and solution element (CE/SE), using the unique approach of enforcing flux conservation in both space and time with extensive physics considerations. A list of key features and advantages of the CE/SE method follows:

- It places extensive consideration on the physical world.
- The method is generic to all conservation laws ($i.e.$, changing solely the Jacobian matrices changes the equations to be solved)
- It adopts a unified treatment of space and time using:
    - The conservation element (CE)
    - The solution element (SE)
- Temporal coordinate is treated in the same way as spatial coordinates for calculating space-time fluxes
- Shock capturing strategy without using a Riemann solver via a staggered mesh that allows for evaluation of fluxes at the cell interfaces

- A complex geometry can be easily fit by using unstructured meshes with mixed shapes

- It is a truly multidimensional scheme where no directional splitting ($i.e.$ Alternating Direction Implicit (ADI) method) is employed

- It is highly computationally efficient and due to its nature, is ideal for parallel computing.

3.2 CE/SE scheme based on hybrid meshes

In the present work, a robust CE/SE scheme based on hybrid meshes[9] is used to solve the governing equations, to simplify the mathematical expression, we define

$$u \equiv U, f \equiv F - \psi_v F_v, g \equiv G - \psi_v G_v \text{ and } s \equiv \psi_s S \tag{3.1}$$

Equation 2.1 is then simplified as

$$\frac{\partial u}{\partial t} + \frac{\partial f}{\partial x} + \frac{\partial g}{\partial y} = s \tag{3.2}$$

The source term caused by chemical reactions and energy relaxation R will be treated separately later. The algorithm[9] will be summarised in the simplest case here to clarify the context of this work.

Considering the spatial coordinates x and y together with t be the new coordinates of a Euclidean space E_3, and then Eq. 3.2 can be expressed as $\nabla \cdot h_m = s_m (m = 1 \text{ to } n_s + 4)$, where $h_m = (f_m, g_m, u_m)$. According to Gauss' divergence theorem, Eq. 3.2 is the differential form of the integral conservation law

$$\oiint_{S(V)} h_k \cdot ds = \iiint_V s_k dV \tag{3.3}$$

where $S(V)$ is the boundary of an arbitrary closed space-time region V in E_3, and $ds = d\sigma n$, in which $d\sigma$ and n are the area and unit outward normal vector of a micro surface element on $S(V)$, respectively.

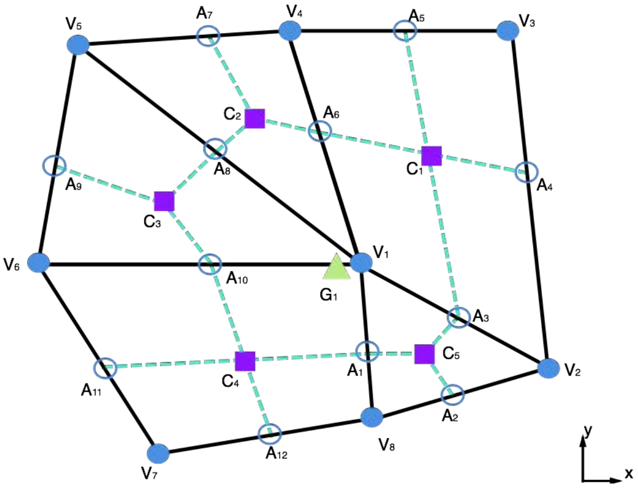

Fig. 3.1.: Arbitrary hybrid mesh

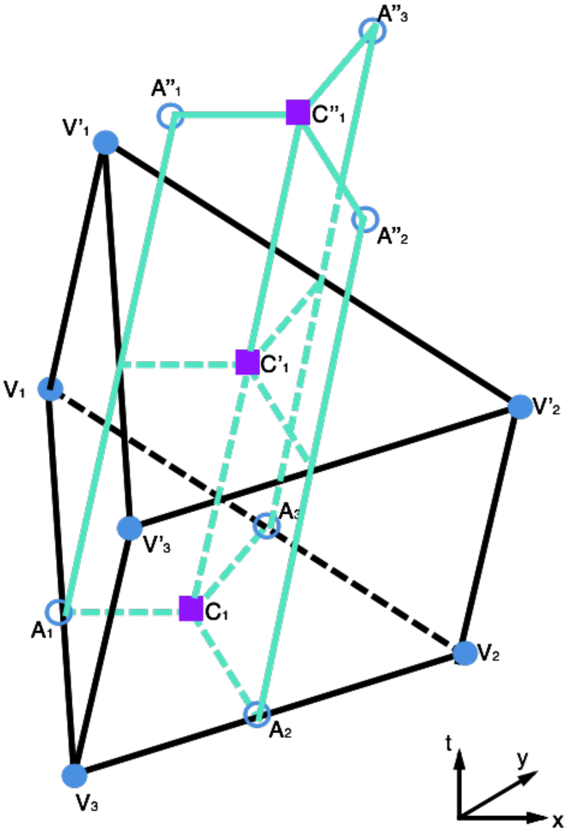

Fig. 3.2.: CE and SE for triangular element

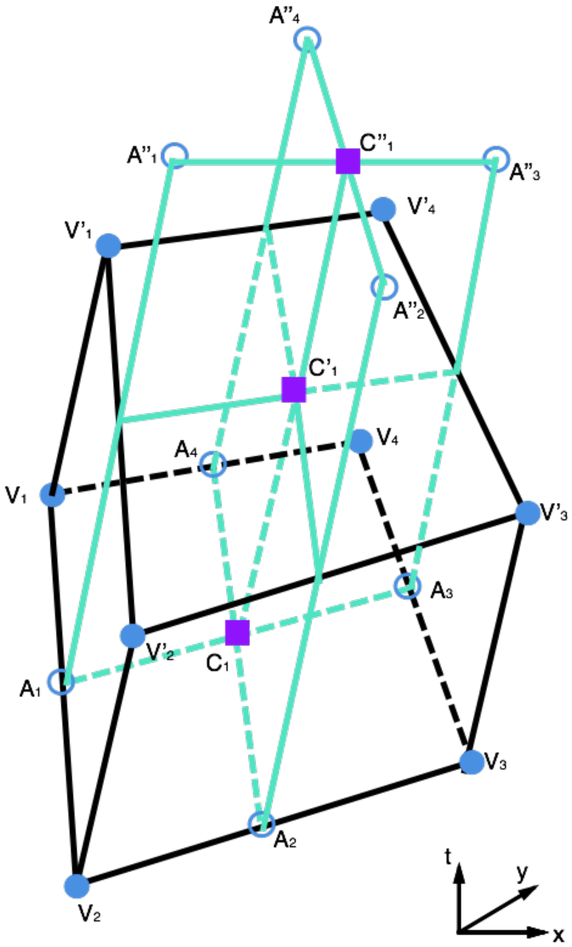

Fig. 3.3.: CE and SE for quadrilateral element

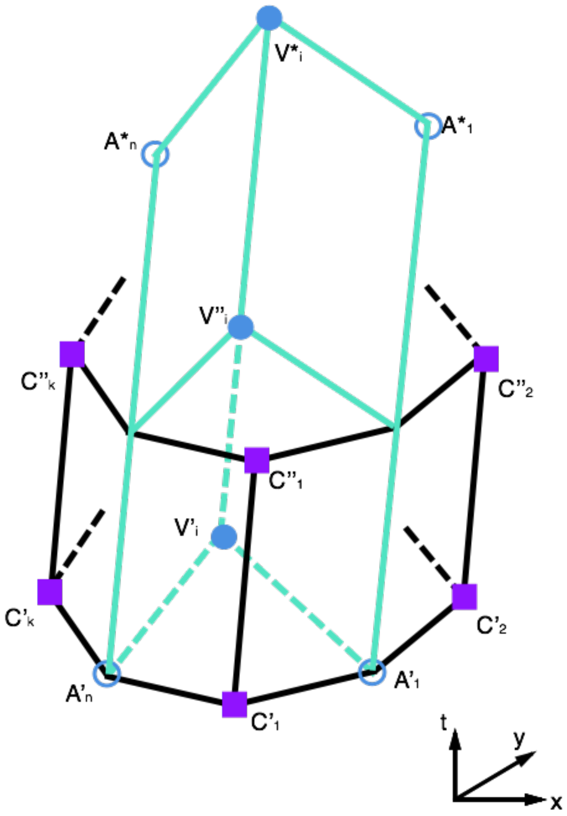

Fig. 3.4.: CE and SE for arbitrary polygonal element

To proceed, the spatial domain is divided into hybrid meshes which including triangular elements and quadrilateral elements, as shown by Fig.3.1. The solid lines represent the original mesh lines. For the convenience of expression, the following notations are adopted:

- V_i the ith vertex (marked by solid circles)
- A_i the ith mid-point of the element edges (marked by hollow circles)
- C_i the ith centroid of the original elements (marked by solid squares)
- G_i the ith centroid of staggered elements (marked by solid triangles). For example, G_1 is the centroid of the staggered element $A_1C_5A_3C_1A_6C_2A_8C_3A_{10}C_4$

For the staggered time marching strategy, the following notations are adopted:

- P the point at time level $t = t_n$ corresponding to the point P
- P' the point at time level $t = t_n + 1/2$ corresponding to the point P
- P'' the point at time level $t = t_n + 1$ corresponding to the point P
- $P*$ the point at time level $t = t_n + 3/2$ corresponding to the point P

With the current strategy, the solution is updated alternatively between element centre (marked by solid squares) and element vertexes (marked by solid circles). In the construction process of a CE/SE scheme, defining conservation element (CE) and solution element (SE) for each solution point is very important. In a hybrid mesh, the corresponding spatial elements for solution points C_i are triangles or quadrangles, while for solution points V_i (or G_i), the corresponding spatial elements could be arbitrary shape of polygons. The configurations of the CE and SE for different shapes of elements are slightly different but essentially identical, which are demonstrated respectively as follows:

1. As shown in Fig.3.2, CE(C_1') for the triangular element $V_1V_2V_3$ is defined by the triangular prism $V_1V_2V_3V_1'V_2'V_3'$, while SE(C_1') is defined by four planes, *i.e.*, $V_1'V_2'V_3'$, $A_1C_1C_1''A_1''$, $A_2C_1C_1''A_2''$ and $A_3C_1C_1''A_3''$, intersecting at C_1' and the triangular prism $V_1'V_2'V_3'V_1''V_2''V_3''$.

2. CE(C'_1) for a quadrilateral element $V_1V_2V_3V_4$ as shown in Fig.3.3 is defined by the hexahedron $V_1V_2V_3V_4V'_1V'_2V'_3V'_4$, while SE($C'_1$) is constituted by five planes, namely $V'_1V'_2V'_3V'_4$, $A_1C_1C''_1A''_1$, $A_2C_1C''_1A''_2$, $A_3C_1C''_1A''_3$ and $A_4C_1C''_1A''_4$, intersecting at C'_1 and the hexahedron $V'_1V'_2V'_3V'_4V''_1V''_2V''_3V''_4$.

The definitions of CE and SE retain the following features:

1. All of the CE's cover the whole space-time domain and do not intersect with each other

2. All of the SE's cover all the CE's and their boundaries and, do not overlap with each other

The definition of CE and SE can be easily extended to cater for any arbitrary shape of polygonal element. Notably, compared with the definition of SE in Ref. [9], we add an additional volume for solving the source term.
Imposing the conservation law of Eq. 3.3 on CE(V''_i) yields,

$$\begin{aligned}\iint_{C''_1A''_1\ldots C''_kA''_k} u_m d\sigma = \sum_{k=1}^{K}\iint_{C'_kA'_kV'_iA'_{k-1}} u_m d\sigma - \\ \sum_{k=1}^{K}\iint_{C'_kA'_kC''_kA''_k+C'_kA'_{k-1}C''_kA''_{k-1}} (f_m n_x + g_m n_y) d\sigma + \\ \iiint_{CE(V''_i)} s_m dV\end{aligned} \tag{3.4}$$

where n_x and n_y are the components of the normal vector of the corresponding surface. To solve the integral terms in Eq.3.4, it is assumed that u_m, f_m, g_m and s_m in each SE are approximated by first order Taylor expansion. That is to say, the distributions of u_m, f_m, g_m and s_m are all linear in CE(V''_i) and its boundary surfaces affiliated to SE(C'_1), ..., SE(C'_K) and SE(V''_i), respectively. Thus, the integrations of (u_m, f_m, g_m)/s_m on any particular surface are simply equivalent to the corresponding area multiplied by the values of (u_m, f_m, g_m)/s_m at the centroid, i.e.,

$$\iint_{C''_1A''_1\ldots C''_kA''_k} u_m d\sigma = u_m(G''_i)\text{Area}(C''_1A''_1\ldots C''_1A''_1) \tag{3.5}$$

$$\sum_{k=1}^{K}\iint_{C'_kA'_kV'_iA'_{k-1}} u_m d\sigma = \sum_{k=1}^{K} u_m(\bar{G}'_k)\text{Area}(C'_kA'_kV'_iA'_{k-1}) \tag{3.6}$$

$$\sum_{k=1}^{K} \iint_{C'_k A'_k C''_k A''_k + C'_k A'_{k-1} C''_k A''_{k-1}} (f_m n_x + g_m n_y) d\sigma = \sum_{k=1}^{K} \left[\text{FLUX}^k_{m_1} + \text{FLUX}^k_{m_2} \right] \tag{3.7}$$

$$\iiint_{CE(V''_i)} s_m dV = \Delta t_{n+1/2} \sum_{k=1}^{K} s_m(G_i *) \text{Area}(C'_k A'_k V'_i A'_{k-1}) \tag{3.8}$$

where $\bar{G}'_k$ and G^*_k are the centroid of quadrangle $C'_k A'_k V'_i A'_{k-1}$ and hexahedron $C'_k A'_k V'_i A'_{k-1} C''_k A''_k V''_i A''_{k-1}$ which belong to SE(C'_k). Therefore, $u(\bar{G}'_k)$ and $u(G^*_k)$ can be calculated via the Taylor expansion in SE(C'_k). In addition, $\text{FLUX}^k_{m_1}$ and $\text{FLUX}^k_{m_2}$ represent the fluxes leaving surfaces $C'_k A'_k A''_k C''_k$ and $C'_k A'_{k-1} A''_{k-1} C''_k$, respectively, and are computed as

$$\begin{aligned} \text{FLUX}^k_{m_1} &= \Delta t_{n+1/2} \Delta y^k_1 \left[f_m(C'_k) + f_{mx}(C'_k) \frac{\Delta x^k_1}{2} + f_{my}(C'_k) \frac{\Delta y^k_1}{2} + f_{mt}(C'_k) \frac{\Delta t^k_{n+1/2}}{2} \right] \\ &\quad - \Delta t_{n+1/2} \Delta x^k_1 \left[g_m(C'_k) + g_{mx}(C'_k) \frac{\Delta x^k_1}{2} + g_{my}(C'_k) \frac{\Delta y^k_1}{2} + g_{mt}(C'_k) \frac{\Delta t^k_{n+1/2}}{2} \right] \end{aligned} \tag{3.9}$$

$$\begin{aligned} \text{FLUX}^k_{m_2} &= \Delta t_{n+1/2} \Delta y^k_2 \left[f_m(C'_k) + f_{mx}(C'_k) \frac{\Delta x^k_2}{2} + f_{my}(C'_k) \frac{\Delta y^k_2}{2} + f_{mt}(C'_k) \frac{\Delta t^k_{n+1/2}}{2} \right] \\ &\quad - \Delta t_{n+1/2} \Delta x^k_2 \left[g_m(C'_k) + g_{mx}(C'_k) \frac{\Delta x^k_2}{2} + g_{my}(C'_k) \frac{\Delta y^k_2}{2} + g_{mt}(C'_k) \frac{\Delta t^k_{n+1/2}}{2} \right] \end{aligned} \tag{3.10}$$

where,

$$\Delta x^k_1 = x_{A_k} x_{C_k}, \; \Delta y^k_1 = y_{A_k} y_{C_k}$$
$$\Delta x^k_2 = x_{C_k} x_{A_{k-1}}, \; \Delta y^k_2 = y_{C_k} y_{A_{k-1}}$$

and

$$\Delta t_{n+1/2} = t_{n+1} - t_{n+1/2}$$

Finally, substituting Eqs.3.5 $\sim$ 3.8 into Eq. 3.4, along with Eqs. 3.9 and 3.10, an explicit time marching scheme for $u_m(G''_i)$ is obtained as

$$u_m(G''_i) = \frac{\sum_{k=1}^{K} u_m(\bar{G}'_k) \text{Area}(C'_k A'_k V'_i A'_{k-1}) - \sum_{k=1}^{K} \left[\text{FLUX}^k_{m_1} + \text{FLUX}^k_{m_2} \right]}{\text{Area}(C''_1 A''_1 \ldots C''_1 A''_1)} + \frac{\Delta t_{n+1/2} \sum_{k=1}^{K} s_m(G_i *) \text{Area}(C'_k A'_k V'_i A'_{k-1})}{\text{Area}(C''_1 A''_1 \ldots C''_1 A''_1)} \tag{3.11}$$

In the first-order Taylor expansion, besides u_m itself, its first-order derivatives are also unknown. Substituting the first-order Taylor expansion into Eq.3.2, one can obtain

$$\frac{\partial u_m}{\partial t} = -\frac{\partial f_m}{\partial x} - \frac{\partial g_m}{\partial y} + s_m \tag{3.12}$$

Therefore, we have to update u_m, u_{mx} and u_{my} at each solution point. As shown by Fig. 3.4, C''_k $(k = 1 - K)$ belongs to both SE(G''_i) and SE(C'_k). Therefore, $u_m(C''_k)$ can be calculated through Taylor expansion in SE(G''_i) and SE(C'_k), *i.e.*,

$$u_m(C'_k) + u_{mt}(C'_k)\Delta t_{n+1/2} = u_m(C''_k) = u_m(G''_i) + u_{mx}(G''_i)\delta x_k + u_{my}(G''_i)\delta y_k \tag{3.13}$$

where

$$\delta x_k = x_{C_k} - x_{G_i} \text{ and } \delta y_k = y_{C_k} - y_{G_i}$$

The same relation can be derived for $k+1$ as

$$u_m(C'_{k+1}) + u_{mt}(C'_{k+1})\Delta t_{n+1/2} = u_m(C''_{k+1}) = u_m(G''_i) + u_{mx}(G''_i)\delta x_{k+1} + u_{my}(G''_i)\delta y_{k+1} \tag{3.14}$$

Note that, $u_m(G''_i)$ has already been calculated by Eq. 3.11, so Eqs.3.13 and 3.14 are linear equations with two unknowns $u_{mx}(G''_i)$ and $u_{my}(G''_i)$. Define

$$\delta u_m^k \equiv u_m(C'_k) + u_{mt}(C'_k)\Delta t_{n+1/2} - u_m(G''_i)$$

Then, one pair of derivatives (defined as $u_{mx}(G''_i)$ and $u_{my}(G''_i)$, respectively) can be calculated using Cramer's rule as

$$u_{mx}(G''_i) = \frac{\Delta^k_{mx}}{\Delta^k_m},\ u_{my}(G''_i) = \frac{\Delta^k_{my}}{\Delta^k_m} \tag{3.15}$$

where

$$\Delta^k_m = \begin{vmatrix} \delta x_k & \delta y_k \\ \delta x_{k+1} & \delta y_{k+1} \end{vmatrix},\ \Delta^k_{mx} = \begin{vmatrix} \delta u^k_m & \delta y_k \\ \delta u^{k+1}_m & \delta y_{k+1} \end{vmatrix},\ \Delta^k_{my} = \begin{vmatrix} \delta x_k & \delta u^k_m \\ \delta x_{k+1} & \delta u^{k+1}_m \end{vmatrix}$$

K pairs of derivatives can be obtained in this way. Thereafter, $u_{mx}(G''_i)$ and $u_{my}(G''_i)$ can be evaluated by the average of the K pairs of derivatives as

$$u_{mx}(G''_i) = \frac{1}{K}\sum_{k=1}^{K} u_{mx}(G''_i),\ u_{my}(G''_i) = \frac{1}{K}\sum_{k=1}^{K} u_{my}(G''_i) \tag{3.16}$$

Alternatively, for a problem with discontinuities, a simple weighted average function [34] can be used as a limiter, $i.e.$,

$$u_{mx}(G_i'') = \frac{\sum_{k=1}^{K} W_m^k u_{mx}(G_i'')}{\sum_{k=1}^{K} W_m^k + \zeta} \tag{3.17}$$

$$u_{my}(G_i'') = \frac{\sum_{k=1}^{K} W_m^k u_{my}(G_i'')}{\sum_{k=1}^{K} W_m^k + \zeta} \tag{3.18}$$

where,

$$W_m^k = \left(\prod_{j=1, j\neq k}^{K} \theta_m^k \right)^{\chi}, \ k = 1 \text{ to K} \tag{3.19}$$

with

$$\theta_m^j = \sqrt{\left(u_{mx}(G_i'')\right)^2 + \left(u_{my}(G_i'')\right)^2}, \ j = 1 \text{ to K} \tag{3.20}$$

Here, $\chi \geq 0$ is an adjustable parameter used to control the dissipations near discontinuities in the computational domain. For the second-order CE/SE scheme, χ is usually assigned a value in the range of 0-2. It is important to underline that when χ increases, the dissipations also increase; when $\chi = 0$ the dissipations are the lowest and Eqs.3.17 and 3.18 are equivalent to the simple average function expressed by Eq.3.16. Furthermore, to avoid dividing by zero, a small positive number (e.g., $\zeta = 10^{-60}$) is added to the denominators. For strong shockwaves ($i.e.$ Mach ≥ 10) MINMOD function can also be used to control the dissipations near discontinuities.

At last, we have to notice that the solution points C_i' at $t_{n+1/2}$ are exactly located at the centres of original elements where the solutions can be directly updated by Eqs.3.11, 3.17 and 3.18 ($K = 3$ and 4 for triangular and quadrilateral elements, respectively). However, the solution points V_i'' at t_{n+1} may not coincide with the centres of the staggered elements G_i''. Consequently, once $u_m(G_i'')$ and its spatial derivatives have been computed through Eqs. 3.11, 3.17 and 3.18, $u_m(V_i'')$ must be updated via the Taylor expansion and its spatial derivatives are equal to $u_{mx}(G_i'')$ and $u_{my}(G_i'')$.

3.3 Stiff Source Term

In the last section, we mentioned that the CE/SE is only used to solve the flow dynamics and the source term caused by chemical reactions and energy relaxation R is treated separately. The rationale behind them is that the CE/SE scheme is an explicit scheme and its time step is limited by the

CFL condition of the CE/SE scheme (CFL$\leq$1). The source terms involving chemical reactions or energy exchange rates may cause the stiffness problem, $i.e.$, the rates may be orders of magnitude higher than the flow velocity. Therefore, if we solve the stiff source terms together with the flow using the explicit CE/SE scheme, the time step may be limited to a very small range due to the limitation of the CFL condition. To overcome this problem, the reacting and energy exchange source term is solved by an implicit trapezoidal method of integration, which is expressed in as

$$\left(I - \Delta t \left[\frac{\partial R}{\partial U}\right]^{n}\right)\left(U^{n+1} - U^{n}\right) = \Delta t R^{n} \tag{3.21}$$

where $\frac{\partial R}{\partial U}$ is the Jacobi matrix of the stiff reacting source term R. I and U are unit matrix and conservative quantity vector, respectively.

3.4 Boundary Conditions

The implementation of boundary conditions in this work is performed by enforcing the conservation laws. The values of its properties are set so that the flux calculation on the boundary face yields the correct flux. For instance, for a wall boundary face, the correct inviscid flux calculations should yield zero mass and energy fluxes. The viscous flux for the wall boundary face should yield viscous forces and heat fluxes.

3.4.1 Inviscid Boundary Condition

The inviscid boundary conditions are defined as follows.

Inlet

The free stream boundaries are given by

$$U_{inlet} = U_{\infty}$$

where U_{∞} are known constants.

Outlet

The outlet boundaries are calculated using a Taylor expansion

$$U_{outlet} = U_c + \frac{\partial U_c}{\partial x}\Delta x + \frac{\partial U_c}{\partial y}\Delta y$$

where U_c is the value of U at the centre of the neighbouring cell.

Wall and Symmetry

The inviscid flux for symmetry and an adiabatic wall are the same. No mass and energy fluxes are accounted for, and momentum flux is given by the pressure only. That is accomplished by,

$$\frac{\partial T}{\partial n} = 0 \text{ and } u_n = 0$$

3.4.2 Viscous Boundary Condition

The viscous boundary conditions are defined as follows.

Inlet

The free stream boundaries are given by

$$U_{inlet} = U_{\infty}$$

where U_{∞} are known constants.

Outlet

The outlet boundaries are calculated using a Taylor expansion

$$U_{outlet} = U_c + \frac{\partial U_c}{\partial x}\Delta x + \frac{\partial U_c}{\partial y}\Delta y$$

where U_c is the value of U at the centre of the neighbouring cell.

Wall

The values at the wall for an isothermal non-catalytic wall are

$$\begin{aligned} u_{wall} &= 0 \\ v_{wall} &= 0 \\ T_{wall} &= const. \\ Y_{n,wall} &= Y_c \\ p_{wall} &= p_c \end{aligned}$$

where T_{wall} is a known wall temperature, Y_c and p_c are the n-th species mass fraction and pressure at the centre of the neighbouring cell respectively. The density at the wall is calculate using the perfect gas law as

$$\rho_{wall} = \frac{\rho_c T_c}{T_w}$$

and the species density as

$$\rho_{n,wall} = \rho_{wall} Y_{n,wall};$$

Implementation

4

> *Ideas are easy. Implementation is hard.*
>
> — **Guy Kawasaki**
> Silicon Valley venture capitalist

4.1 Introduction

This chapter addresses some aspects of the implementation of the in-house CE/SE code. While it is not viable to detail all the aspects of the code, it is important to detail the general structure of the code and some of the operations that are performed during its execution. Furthermore, the boundary conditions implementation, the Courant insensitive scheme, and the parallelisation strategy are described in the chapter.

4.2 Code Overview

The in-house code has been written using the C^{++} language, this language was selected because of the following advantages:

- A native support for object oriented programming
- Efficient memory management
- The usage of STL libraries
- User-defined operators and function overloading are supported
- Backward compatibility with C
- Great readability, reusability and portability

The code starts by allocating the number of processors that are to be used. Next, the code reads the mesh files, in this step the memory allocation and the mesh processing occur. During the processing, the dimensions of the element are assigned and the staggered elements are constructed.

The CE/SE solver begin and the initial conditions are read from the input and assigned to each element of the domain. A loop then is started, it will continue as long as it hasn't reached the assigned final time.

Due to the nature of the CE/SE method, each time step is divided by half, during the first half, the local CFL is assigned, the fluxes and derivatives are computed, the chemistry source term is calculated, the value of U is updated and then the values of $\frac{\partial u}{\partial x}$ and $\frac{\partial u}{\partial y}$ are calculated with the weight average function shown in Eqs. 3.16-3.20.

During the second half time step, the process is similar to the first half, but due to the staggered nature of the method, the boundary conditions are only calculated at each full time step, ($i.e.\ t = n+1$). The simulation is completed, the results are written in two output files, one assigned for the wall surface and one for the whole domain. Finally, the code flushes the memory of the computer.

An overview of the execution of the code is shown in listing 4.1.

Listing 4.1: Code overview

```
Set number of processors to be used.
Read mesh
    Allocate memory
    Process mesh
        Calculate dimensions of element
        Define the centre of element
        Construct staggered elements
Start CE/SE solver
Read initial conditions
Assign initial condition to each element
Start loop while t < assigned time
    Calculate for t=n+1/2
        Calculate local CFL number
        Compute fluxes F and G, and derivatives
        Compute U
        Calculate the chemistry source term
        Update the value of U
        Compute x and y derivatives
```

```
    Calculate for t=n+1
        Calculate local CFL number
        Compute fluxes F and G, and derivatives
        Compute U
        Calculate the chemistry source term
        Update the value of U
        Compute x and y derivatives
        Calculate the boundary conditions
End simulation
Output results
    Create wall output file
    Create full domain output file
Free memory
```

For reference, a 2D structured CE/SE code is included in Appendix C.

4.3 Boundary Conditions

The treatment of the boundary conditions is based on the same principle of fluxes conservation treatment we give to the whole domain, the difference lays on the structure of the boundary edge, Fig. 4.1 shows the boundary node structure and table 4.2 shows an example of a typical "meshfile.bnd" file used to assign the boundary conditions, where column "a" is an assigned boundary edge number, columns "b"and "c" are the elements on the left and right of the boundary edge (See Fig. 4.1), columns "d" to "g" are ignored and column "h" assigns the boundary type according to Table 4.1.

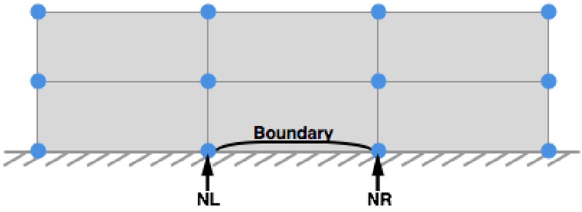

Fig. 4.1.: Structure used to determine the boundary edge

After the code has already processed the boundary file information, each node has two boundary edges assigned, the right side one sharing the same ID and the one on the left assigned as BL (See Fig.4.2). Each node needs to

Tab. 4.1.: Definition of Boundary conditions.

outl	Outlet Boundary Condition
inle	Inlet Boundary Condition
wall	Adiabatic Boundary Condition
isot	Isothermal Boundary Condition
sym	Symmetry Boundary Condition

Tab. 4.2.: File meshfile.bnd structure.

a	b	c	d	e	f	g	h
1	1	2	0	0	1	0	inle
2	3	8	0	0	1	0	outl
3	4	6	0	0	1	0	wall
4	5	5	0	0	1	0	sym
⋮	⋮	⋮	⋮	⋮	⋮	⋮	⋮

check how many related elements are surrounding it. In the case of a normal element we have 2 related elements (Fig.4.3), but for a corner element we only have one (Fig.4.4)

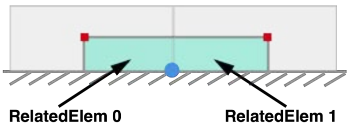

Fig. 4.3.: Normal element with two related elements

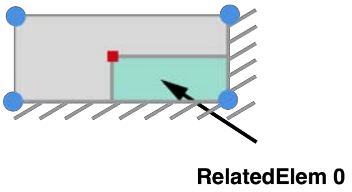

Fig. 4.4.: Corner element with one related elements

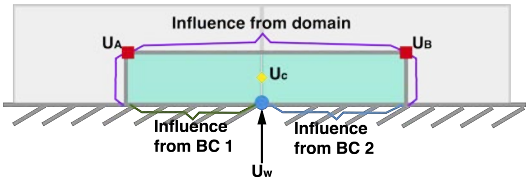

Fig. 4.5.: Boundary condition treatment

To calculate the value (U_w) at the boundary, we need to consider the influence

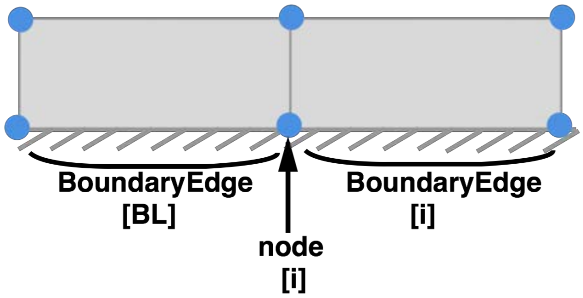

Fig. 4.2.: The stencil of the boundary conditions

of the inner domain and the wall. Therefore, we first calculate the value of U at the centre (U_c) and from it, we do a Taylor expansion to get the value at the wall. This is accomplished with the following steps,

1. Get the fluxes through inner domain
2. Get the values through left boundary
3. Get the values through right boundary
4. Calculate the values at the centre (U_c)
5. Calculate the values of $\frac{\partial U_c}{\partial x}$ and $\frac{\partial U_c}{\partial y}$
6. Perform a Taylor expansion using U_c, $\frac{\partial U_c}{\partial x}$ and $\frac{\partial U_c}{\partial y}$ in the form $U_w = U_c + \frac{\partial U_c}{\partial x}(x_{U_w} - x_{U_c}) + \frac{\partial U_c}{\partial y}(y_{U_w} - y_{U_c})$

It is important to note that sometimes the node will be located in a corner, the influence of the wall boundary conditions has a great effect on the result, therefore, the values have to be calculated using the influence from the left and right side boundary edges.

4.4 Courant Number Insensitive (CNI) scheme

For highly non-uniform meshes, the accuracy of the CE/SE method is significantly impacted by large numerical dissipation. To overcome this, Chang [35] introduced the Courant number insensitive CE/SE scheme to deal with small CFL numbers. The presented CNI scheme is based on the works done by Chang[36] to extend the CNI scheme to 3D calculations. Because of they hybrid mesh nature of the current code, certain modifications had to be made.

Figures 4.6 and 4.7 show the definition of the points M_i, G_i and P_i at $t = n/2$ and $t = n$ respectively. When $t = n/2$, the Values of G_i represents the original mesh axis and G^* is the centroid of the element. When $t = n$, the values of G_i represents the centroid of the element and G^* is the original mesh axis The value of M_i is the centroid of the small element in $t = n/2$ and $t = n$ To

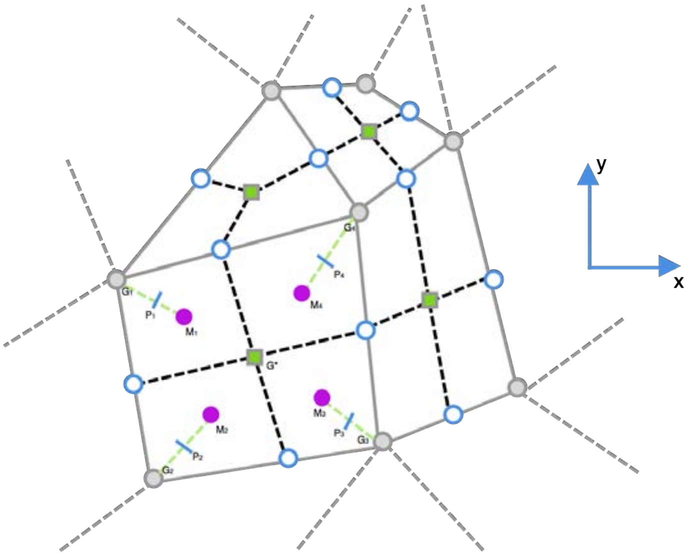

Fig. 4.6.: Definition of points for $t = n/2$

calculate the location of P_i, along the line segments M_iG_i we use the local CFL number of G^* such that

$$\frac{x_{P_i} - x_{M_i}}{x_{G_i} - x_{M_i}} = CFL_{local}(G^*)$$

Therefore, when the local CFL number goes down to zero, the value of P_i is the same as of M_i. Also, when the local CFL number equals one, the location of P_i is the same as G_i Then we get the values of U^n at P_i

$$U^n_{P_i} = U^{n-0.5}_{G_i} + \frac{\Delta t}{2}\left(\frac{\delta u}{\delta t}\right)^{n-0.5}_{G_i} + (x_{P_i} - x_{G_i})\left(\frac{\delta u}{\delta x}\right)^{n-0.5}_{G_i} + (y_{P_i} - y_{G_i})\left(\frac{\delta u}{\delta y}\right)^{n-0.5}_{G_i}$$

To calculate of $\left(\frac{\delta u}{\delta x}\right)_{G_i}$ and $\left(\frac{\delta u}{\delta x}\right)_{G_i}$ at time n first using the values of P_i, we design 3 or 4 areas (depending of the geometry of the mesh) as shown in Figure4.8 and we apply,

$$\left(\frac{\delta u}{\delta x}\right)^{K_1}_{G^*} = \frac{1}{2 * A_{[P_1P_2G^*]}}\left[(y_{P_1} - y_{P_2}) * (u^n_{G^*}) + (y_{G^*} - y_{P_1}) * (u^n_{P_2}) + (y_{P_2} - y_{G^*}) * (u^n_{P_1})\right]$$

and,

$$\left(\frac{\delta u}{\delta y}\right)^{K_1}_{G^*} = \frac{1}{2 * A_{[P_1P_2G^*]}}\left[(x_{P_1} - x_{P_2}) * (u^n_{G^*}) + (x_{G^*} - x_{P_1}) * (x^n_{P_2}) + (x_{P_2} - x_{G^*}) * (u^n_{P_1})\right]$$

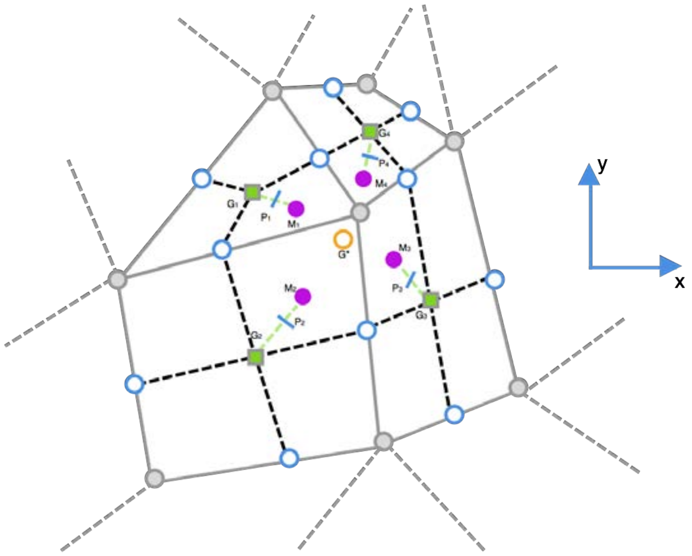

Fig. 4.7.: Definition of points for $t = n$

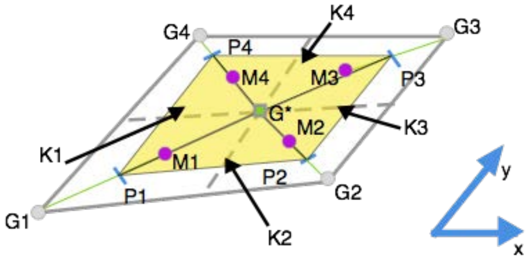

Fig. 4.8.: CNI scheme implementation

Where $A_{[P_1 P_2 G^*]}$ is the area of the triangle formed with the axis of P_1, P_2, G^*. Then we can do the same for the triangles K_2, K_3 and K_4. Finally, to get the values of $\left(\frac{\delta u}{\delta x}\right)^n_{G^*}$ and $\left(\frac{\delta u}{\delta y}\right)^n_{G^*}$ we use a weighted average function like the one used in Eqs. 3.16-3.20.
For strong shockwaves ($i.e.$ Mach $\geq$ 10) MINMOD function can also be used to control the dissipations near discontinuities.

4.5 Parallelisation

To increase the computational efficiency and reduce the workload, the code is parallelised using OpenMP.
OpenMP is a programming run-time library used for writing parallel programs on shared memory multiprocessor systems. It is a multi-platform library that can be used with C, C^{++}, and FORTRAN. It's implemented during compilation and it uses the fork-join model of parallel execution[37] .

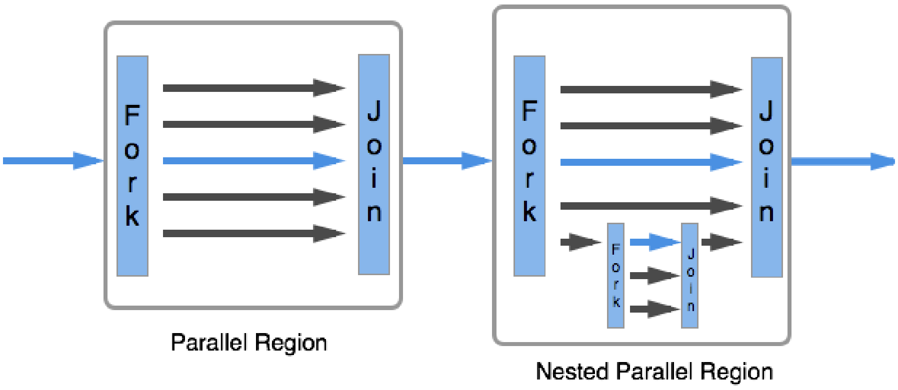

Fig. 4.9.: OpenMP Fork-Join Execution Model

An OpenMP program starts with a "master" thread, it executes sequentially until a parallel region is encountered. Then, a set of parallel threads is created. The instruction in the code that are assigned to the parallel region are executed at the same time. After the instructions are completed, they all synchronise with the master thread and the parallel region is terminated, leaving the "master" alone. OpenMP supports nested parallelism. This is accomplished by placing a parallel set of instructions inside another one. (See Fig. 4.9)
Listing 4.2 shows a simple example of an openMP implementation.

Listing 4.2: Simple openMP example

```
#include <omp.h>
int main()
{
omp_set_num_threads(4); //Set number of parallel threads
#pragma omp parallel for // A parallel loop is initialised
for(int i=0;i<ArrayDimen;i++)
        {
        functionA();
        #pragma omp for  // A nested parallel loop is initialised
        for (int i=0; i<n; i++)
                {
                functionB();
                }
        }
return 0;
}
```

4.6 Equipment

The majority of the simulations were performed using a custom-built workstation, the technical specs are shown in table 4.3
The workstation is supported by the High-speed Thermo-fluid and MAV/UAV Laboratory (HTML) at the Hong Kong Polytechnic University in Hung Hom, Kowloon, Hong Kong, S.A.R.

Tab. 4.3.: Workstation Tech Specs.

Operating System	Windows 7
System Type	64 bit
Memory	64.0 GB
Processor	Intel(R) Xeon(R) CPU E5-2630 v2 @2.6GHz (x2 processors)
Cores	6 (x2) (x2 processors)

Results

5

> *Scientific Progress goes "boink"!*
>
> — **Hobbes**
> (Bill Waterson's character)

5.1 Introduction

This chapter presents code validation efforts using available experimental, numerical and flight data for space capsules. The fist part will deal with inviscid flows, including Nitrogen, Air and CO_2, around spheres and the RAM-C capsule. The second part will present certain validation cases and results for viscous flows around spheres.

5.2 Inviscid Flows

When the hypersonic flow encounters a sphere, a bow shock will detach from the surface of the sphere. The shape of the bow shock and the distance between the shock and body on the stagnation line, namely the shock stand-off distance, Δ, are two important flow characteristics. The present work will focus on the study of these two flow features. The flow is assumed to be inviscid and axisymmetric, such that the computational domain is reduced to only one-half of the complete flow field (Figure. 5.1). Grid-independence tests were carefully performed for all test cases. This was achieved by running a series of simulations increasing the mesh size by a factor of 1.5 until the difference in the stagnation streamline properties between mesh models was smaller than 2%.

Figure 5.2 shows the density distribution along the stagnation streamline for case 9 using different mesh sizes. Pressure and speed distributions for all the cases of this study also show similar convergence with their respective mesh size.

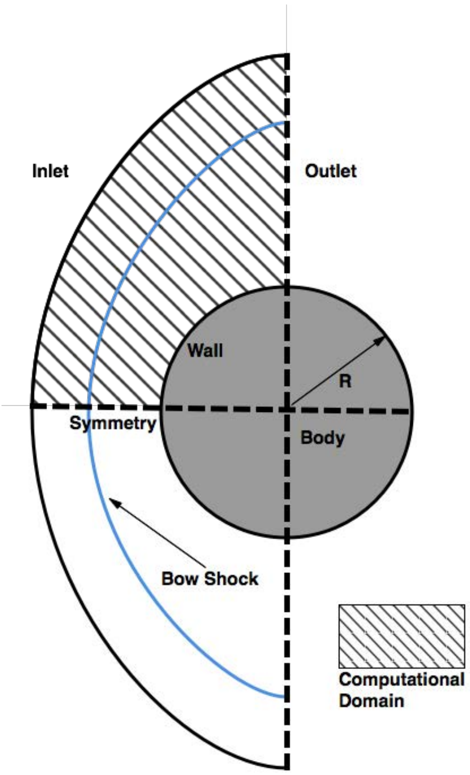

Fig. 5.1.: Schematic of computational model for sphere cases

5.2.1 Nitrogen Flows

Nitrogen flow is one of the simplest hypersonic dissociating flows. If there is no ionisation, only two species exist in the flow. Therefore, nitrogen flow has been widely investigated by previous researchers. In the present study, we first apply the CE/SE code to simulate the experimental nitrogen flow cases selected from Wen [38], where the hypervelocity flows over spheres of various radii and free-stream conditions were studied. The sphere radii and free-stream conditions of selected cases are listed in table 5.1 and the comparison of experimental, theoretical and numerical dimensionless shock-off distances are listed in table 5.2. Here, the theoretical results are calculated by Wen &

Tab. 5.1.: Free-stream conditions of nitrogen flow cases selected from Wen[38].

Case No.	R(m)	ρ_∞ (kg/m^3)	u_∞ (m/s)	T_∞ (K)	α_∞
1	0.013	0.0374	5150	2340	0.036
2	0.025	0.0198	4860	1950	0.041
3	0.038	0.0195	5140	2200	0.064
4	0.051	0.0181	5350	2350	0.090

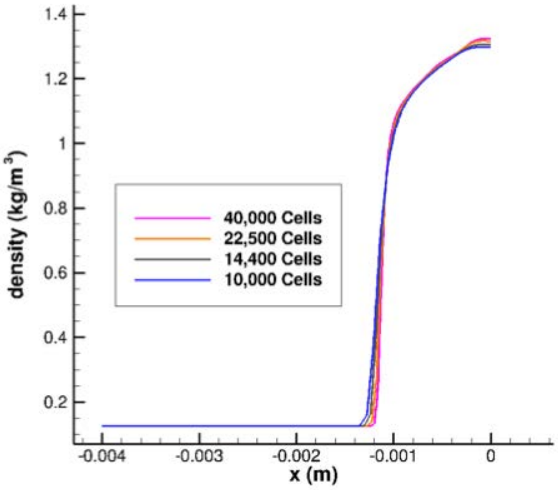

Fig. 5.2.: Density distribution along the stagnation streamline for case 9 using different mesh sizes

Hornung's theory[39], which is based on the fact that the oncoming mass flow entering the shock has to leave the flow field between shock and body. This theory[39] gives an analytic solution for the whole non-equilibrium flow regime without use any specific gas model and is presented by a piecewise function as

$$\begin{cases} \tilde{\Delta} = \frac{1}{\tilde{\Omega}}\left[-1+\sqrt{1+2L\tilde{\Omega}}\right], & when \quad \rho_b < \rho_e \\ \tilde{\Delta} = \frac{\rho_{sh}}{\rho_e}\left[L+\frac{1}{2\tilde{\Omega}}\left(\frac{\rho_e}{\rho_{sh}}-1\right)^2\right], & else \end{cases} \tag{5.1}$$

Here, the constant L equals to 0.41 for spheres that is given by the well-known Lobb's [40] correlation for supersonic frozen flows. $\tilde{\Delta}$ is another dimensionless shock-off distance which is defined as

$$\tilde{\Delta} \equiv \frac{1}{2}\frac{\Delta}{R}\frac{\rho_{sh}}{\rho_\infty} \tag{5.2}$$

The generalized dimensionless reaction rate parameter $\tilde{\Omega}$ is defined by

$$\tilde{\Omega} \equiv \left(\frac{\partial \rho}{\partial t}\right)_{sh} \frac{D}{\rho_{sh} u_\infty} \tag{5.3}$$

At the first glance, $\tilde{\Omega}$ represents the density variation right after the shock on the stagnation streamline when the flow passes the sphere. However, Wen & Hornung[39] deepened physical significance of $\tilde{\Omega}$ as

$$\tilde{\Omega} = \frac{\text{Energy absorption rate by chemistry}}{\text{Input rate of free stream kinetic energy}}$$

From table 5.2 , we can see that the present numerical results agree very well with Wen & Hornung's experimental and theoretical results. The largest error between the results of simulation and experiments is about 5%. To further compare the numerical results with Wen & Hornung's experimental results, we compare the bow shock shapes by overlapping the numerical density contours in the experimental finite fringe differential interferograms in Fig. 5.3. It is shown that the shapes of the numerical bow shocks fit the experimental results very well. It demonstrated that the present code is reliable for simulating hypersonic dissociating flows. To thoroughly study the influence of the parameter $\tilde{\Omega}$ on the flow features of hypersonic dissociating flows, we choose one typical set of free-stream condition as $\rho_\infty = 0.0443 kg/m^3$, $u_\infty =, 200 m/s$, $T_\infty = 2300K$ and $\alpha_\infty = 0.0156$. The radii of spheres are varied to obtain different between 0.2 and 111. The comparison of dimensionless shock-off distance $\tilde{\Delta}$ between present numerical results and Wen & Hornung's theory is shown in Fig. 5.4. It is clearly demonstrated that the present code is accurate throughout the whole non-equilibrium flow regime. The largest difference between numerical method and the theory is about 6.7%, which occurs at medium $\tilde{\Omega}$ value. Notably, the numerical shock standoff distance

Tab. 5.2.: Experimental, theoretical and numerical dimensionless shock stand-off distance, $\tilde{\Delta}$, for nitrogen flows.

Case No.	Experiment (Wen & Hornung) [39]	Theory (Wen & Hornung) [39]	Simulation	Error
1	0.096	0.095	0.101	5.2%
2	0.114	0.099	0.109	4.3%
3	0.100	0.095	0.100	0.0%
4	0.099	0.094	0.099	0.0%

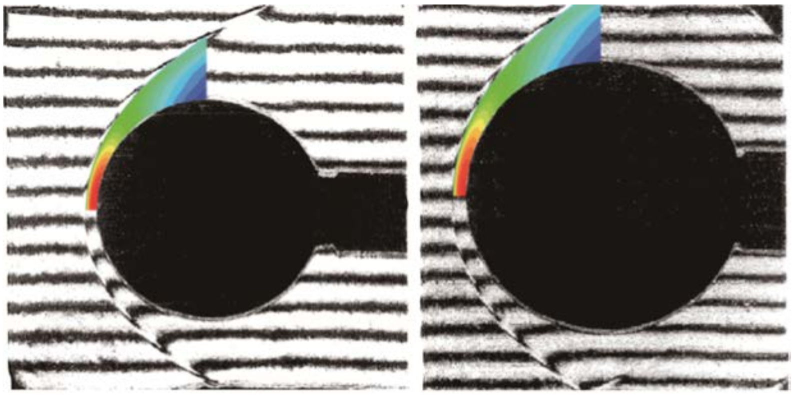

Fig. 5.3.: Comparison of the numerical and experimental shapes of the bow shock for Nitrogen flows for case 3 (left) and case 4 (right)

is a little larger than that of Wen & Hornung's theory. It is because Wen & Hornung used a piecewise linear function to describe the density distribution on the stagnation line and the average density was slightly overestimated. Consequently, the shock standoff distance is underestimated [39].

Figure 5.5 shows the density profiles and N atomic distributions of different sphere radii. When the free-stream condition is fixed, the value of chemical reaction parameter $\tilde{\Omega}$ will increase with sphere radii according to the definition of $\tilde{\Omega}$. It indicates that when the gas flows over a sphere, the gas has more time for dissociating and energy relaxation in the larger sphere cases and the dissociating level, $i.e.$ the mass fraction of N atoms, is, therefore, higher. Meanwhile, the density behind the shock also reaches a higher level and the distribution of vibrational temperature is closer to that of translational temperature (See Fig. 5.6). For the case of R=0.063 mm, the highest mass fraction of N only reaches to about 0.036, and the highest dimensionless density is just over 6 which is the density ratio of frozen flows. For the case of R=1.02 meters, the highest mass fraction of N is higher than 0.2, and the highest dimensionless density approaches 9.8 which is the density ratio of fully equilibrium flows.

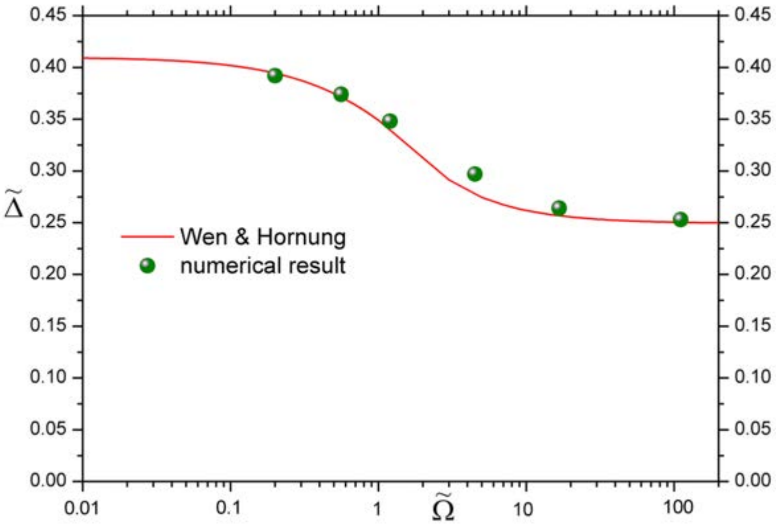

Fig. 5.4.: Comparison of dimensionless shock standoff distance for nitrogen flows

5.2.2 Air Flows

Air flow is much more complicated than nitrogen flow but is very important in practice. First, we also pick four air flow cases from Wen & Hornung's experiments. The free-stream conditions, free-stream mass fractions and the

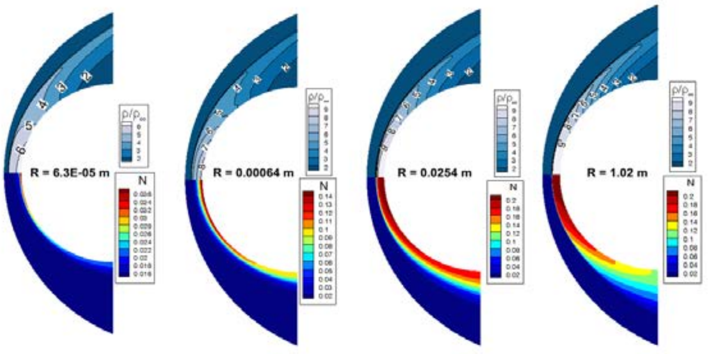

(a) $\tilde{\Omega} = 1.2$ (b) $\tilde{\Omega} = 4.5$ (c) $\tilde{\Omega} = 16.7$ (d) $\tilde{\Omega} = 111$

Fig. 5.5.: Distributions of dimensionless density (ρ/ρ_∞, upper) and mass fraction of atomic nitrogen (lower) for nitrogen flows

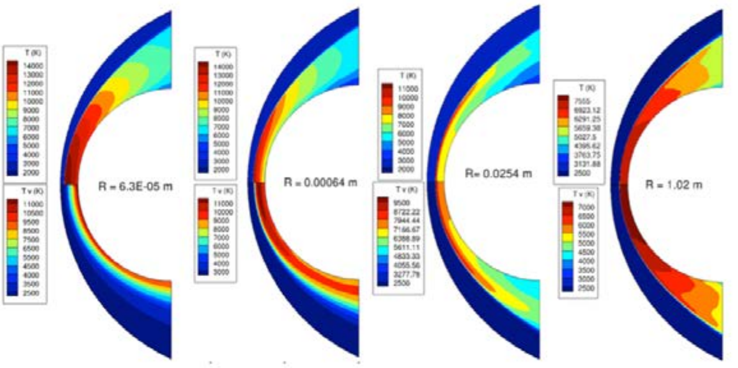

(a) $\tilde{\Omega} = 1.2$ (b) $\tilde{\Omega} = 4.5$ (c) $\tilde{\Omega} = 16.7$ (d) $\tilde{\Omega} = 111$

Fig. 5.6.: Translational temperature (T, upper) and vibrational temperature (Tv, lower) for nitrogen flows.

dimensionless shock stand-off distance comparison are listed in table 5.3, 5.4 and 5.5. Good agreement between experimental, theoretical and numerical results is observed. The numerical shapes of the entire bow shocks are also very close to the experimental results, as shown in Fig. 5.7.

The free-stream conditions of case 6 are adopted and the radii of spheres are varied to obtain different $\tilde{\Omega}$ between 0.595 and 62.4. Fig.5.8 shows the comparison of numerical and theoretical dimensionless shock standoff distances. The largest error is only about 6%. Figure 5.9 shows the distributions of species. It is found that the mass fraction of O atoms is much higher than that of N atoms. It is because that the characteristic dissociating temperature of O_2 (59,500K) is much lower than that of N_2 (113,200K). Under the same temperature, the dissociating level of O_2 is much higher than that of N_2. Even for the case of R=1.02 meters ($\tilde{\Omega}$=62.4), the mass fraction of N is only about 0.6%, but the mass fraction of O reaches to 20%. On the upper side of

Tab. 5.3.: Free-stream conditions of Air flow cases selected from Wen[38].

Case No.	R(m)	ρ_∞ (kg/m^3)	u_∞ (m/s)	T_∞ (K)
5	0.013	0.0584	4110	1590
6	0.025	0.0278	3930	1370
7	0.038	0.03	3960	1410
8	0.051	0.0158	5560	2620

Tab. 5.4.: Free-stream mass fraction of Air flow cases selected from Wen[38].

Case No.	N_2	O_2	NO	N	O
5	0.724	0.180	0.064	2.39E-8	0.0171
6	0.724	0.171	0.065	5.91E-9	0.0262
7	0.724	0.171	0.0648	8.33E-9	0.0259
8	0.743	0.0341	0.0252	3.97e-5	0.184

the sphere, there is almost no N due to the flow expansion. The consequent significant temperature decrease during the flow expansion yields the full recombination of the atomic nitrogen. On the other hand, the mass fraction of O is still more than 10%. The distribution of translational temperature and vibrational temperature is similar to that of nitrogen flows (see Fig. 5.6).

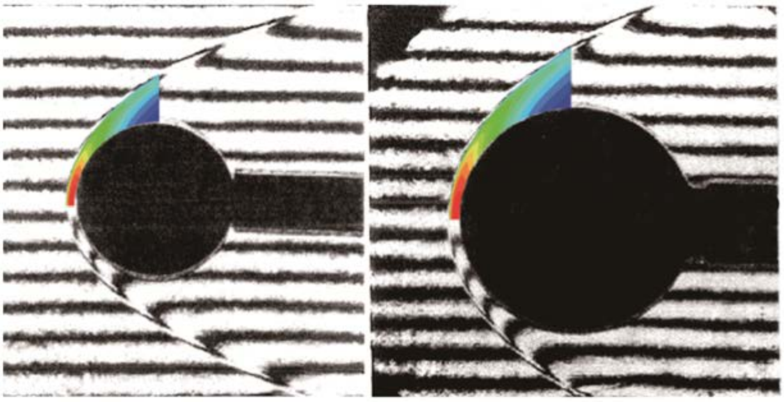

Fig. 5.7.: Comparison of the numerical and experimental shapes of the bow shock for air flows for case 6 (left) and case 7 (right)

5.2.3 CO_2 Flows

To perform accurate modeling for reentry of space vehicles in the Martian atmosphere is of primordial importance to study reacting carbon dioxide flows, the primary element in the Martian atmosphere. We selected three CO_2 flow cases from Wen & Hornung's[39] experiments. The free-stream

Tab. 5.5.: Experimental, theoretical and numerical dimensionless shock stand-off distance, $\tilde{\Delta}$, for Air flows.

Case No.	Experiment (Wen & Hornung) [39]	Theory (Wen & Hornung) [39]	Simulation
5	0.101	0.092	0.092
6	0.105	0.093	0.095
7	0.103	0.094	0.093
8	0.090	0.084	0.087

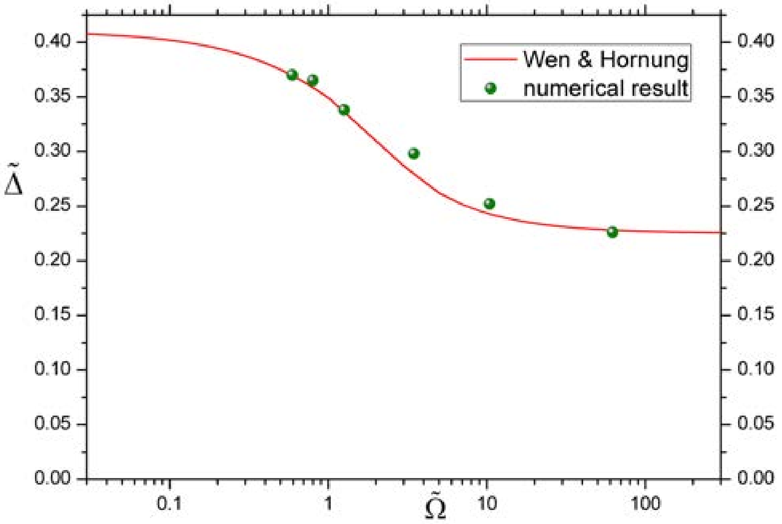

Fig. 5.8.: Comparison of dimensionless shock standoff distance for air flows

conditions, free-stream mass fractions, and the dimensionless shock stand-off distance comparison are listed in table 5.6, 5.7 and 5.8. Fig.5.10 shows the comparison of the bow shock shapes between the numerical analysis and the experimental results. A good agreement is observed.

The free-stream conditions of case 10 were adopted and the radii of spheres

Tab. 5.6.: Free-stream conditions of CO_2 flow cases selected from Wen[38].

Case No.	R(m)	ρ_∞ (kg/m^3)	u_∞ (m/s)	T_∞ (K)
9	0.025	0.0937	3100	1900
10	0.038	0.150	2560	1240
11	0.051	0.0326	3490	2010

are varied to obtain different $\tilde{\Omega}$ between 1.539 and 50.5824. The comparison of numerical and theoretical dimensionless shock stand-off distances is shown on Fig.5.11. The largest error is about 5.05%. Figure 5.12 shows the distributions of CO_2 and O atoms. It can be seen that for the first two cases the dissociation of CO_2 is relatively small, this due to the fast speed

Tab. 5.7.: Free-stream mass fraction of CO_2 flow cases selected from Wen[38].

Case No.	CO_2	O_2	CO	O	C
9	0.739	0.0941	0.166	0.0008	0.0001
10	0.922	0.028	0.049	0.0005	0.0005
11	0.459	0.185	0.344	0.0115	0.0005

Tab. 5.8.: Experimental, theoretical and numerical dimensionless shock stand-off distance, $\tilde{\Delta}$, for CO_2 flows.

Case No.	Experiment (Wen & Hornung) [39]	Theory (Wen & Hornung) [39]	Simulation
9	0.0898	0.0872	0.0876
10	0.090	0.0888	0.0898
11	0.088	0.0864	0.087

of the flow and small radius of the spheres. When the radius of the sphere increases a more noticeable dissociation occurs and it can be appreciated that it happens mostly in the stagnation region, on the upper side of the sphere, there is almost no atomic oxygen due to the flow expansion.

5.2.4 Weakly Ionised Hypersonic Flows

When the space vehicle enters the atmosphere at an orbital speed, a detached bow shock forms in front of its blunt nose and the temperature behind the shock, especially in the stagnation region, can reach high levels, due to the conversion of kinetic flow energy into thermal energy by strong shock compression. At hypersonic speeds, the massive amount of kinetic energy leads to the presence of ionisation in the shock layer, providing a large number of free electrons. These free electrons absorb radio-frequency radiation and cause radio blackout (For the Apollo 13 mission, communication blackout lasted around six minutes). Thanks to satellites orbiting the earth, communications blackout is not the problem it used to be, nevertheless, is still a very real problem encountered in atmospheric reentry, mainly because it's not confined to earth's atmosphere. Past missions to mars have shown us that this problem also occurs in CO_2 environments, therefore it is of high importance to accurately predict the electron number density in the plasma sheath around any capsule. To validate the code capabilities regarding hypervelocity flows, shock standoff on spheres in air is simulated based on

Tab. 5.9.: Free-stream conditions of Air flow cases selected from Zander et al. [41].

Case No.	R(m)	ρ_∞ (kg/m^3)	u_∞ (m/s)	T_∞ (K)	Mach
12	0.04	1.38E-3	8.73±0.14	2,013.4	10.3
13	0.06	1.38E-3	8.73±0.14	2,013.4	10.3
14	0.08	1.38E-3	8.73±0.14	2,013.4	10.3

Tab. 5.10.: Free-stream mass fraction of Air flow cases selected from Zander et al. [41]

Case No.	N_2	O_2	NO	N	O
12	0.7866	0.2051	0.0063	0.0	0.002
13	0.7866	0.2051	0.0063	0.0	0.002
14	0.7866	0.2051	0.0063	0.0	0.002

experiments performed by Zander et al. [41]. The free-stream conditions and the initial mass fraction of main species of the selected cases are listed in table 5.9 and 5.10. Figure 5.13 shows the comparison of the experimental data by Zander et al.[41] and the CE/SE simulations of shock standoff (Δ/D) distance vs. flow velocity. A good agreement between experimental and numerical results is observed.

5.2.5 RAM-C Model

The Radio Attenuation Measurement (RAM) experiment was a series of hypersonic flights performed in the 1960's to study communications blackout, this experiment was frequently used to evaluate the modeling of weakly ionised gases[27]. The RAM-C geometry is composed by a spherically blunted cone with a nose radius of 0.1524 m, a total length of 1.3 m and a 9^o half angle. In this work, the flow condition corresponding to the 71km altitude trajectory point, with a free-stream speed, density, and temperature of 7650 m/s, 2.7E-4 kg/m^3 and 254K respectively is simulated. The airflow initial mass fractions is that of 0.79 N_2 and 0.21 O_2. For the simulations, the flow is assumed to be axisymmetric, therefore a symmetric boundary condition is applied to the lower boundary. Figure 5.15 shows the translational temperature along the stagnation streamline for the RAMC-II capsule, it is seen that it reaches a peak of about 25,500 K which is similar to the results presented by Candler & MacCormack[42] for the same case, the behaviour of the temperature at the wall is due to the adiabatic wall conditions assumed in the simulation. Maximum electron number densities along the direction normal to the vehicle surface are compared to flight data and numerical simulations done by Candler & MacCormack 10 in Fig5.14. The electron number densities are in good agreement with the RAM-C II flight experiment. It can be observed that a rapid decrease in the electron number density occurs as the flow moves downstream, this is due to the expansion along the spherical nose yielding temperature reduction. Figure 5.16 shows a comparison of the mass distribution of O_2 , N_2 and NO^+ around RAMC-II capsule. It can be observed that high amounts of dissociation and reaction are found in the front face of the experimental capsule. This is due to the abrupt increase of temperature behind the shock wave. The most pronounced dissociation happens with respect to the oxygen molecules due to their corresponding low dissociation energy. On the other hand, the nitrogen molecules dissociate less significantly because of their high dissociation energy. Ionisation effects of NO^+ are notable in front of the capsule nose. This is caused by the associative-recombination reaction $N + O \leftrightharpoons NO^+ + e^-$ forming NO^+ and free electrons, which, in terms of the overall composition of the gas, are small, but of particular significance when dealing with radio communication.

5.3 Viscous Flows

5.3.1 Validation Cases

When we deal with high speed vehicles, the matter of aerodynamic heating and shear stress is of extreme importance, hence, a strong emphasis is placed on accurately predicting any viscous flow, a series of benchmark cases have been performed to prove the capabilities of the CE/SE solver for subsonic, supersonic and real gas cases.

Driven cavity

A driven cavity was simulated as a benchmark to demonstrate the capability of the CE/SE solver for viscous flows. The results were compared with the works done by Ghia et al.[43]. Fig.5.17a shows the comparison of the u-velocity profile along vertical centerline for Re = 400. The Reynolds number is based on the height of the cavity and the moving speed of the top wall

(Mach 0.15). It can be seen from Fig.5.17b that the method has captured the primary vortex and the two secondary vortices.

Shock/Boundary Layer Interactions

A shock wave boundary layer interaction problem is used as a validation case. The results were compared with the works done by Zhang et al.[44]. Fig.5.18 a shows the pressure contours of the shock boundary layer interaction problem. Pressure Distribution at the wall and the skin friction distribution along wall are shown in figures 5.19 and 5.20 respectively. It can be observed that once the shock capture parameter α has been tuned, the results are in good agreement with both the simulations done by Zhang et al.[44] and the experiments done by Hakkinen et al.[45].

Shock tube reflection

To validate the code capabilities regarding high speed viscous and compressive flows, the reflection of a normal shock wave from the end wall of a shock tube has been simulated. In this test case, the shock bifurcation is simulated based on experiments performed by Matsuo et al.[46]. To save computational resources, only the last 0.15m of the channel adjacent to the end wall and half a domain of 0.02m with an incident Mach number of 2.6 were simulated. The results provided by the CE/SE code were then compared against the experimental results of Matsuo et al. and the numerical results of Weber et al. [47]. Figure 5.21 shows the triple point trajectories from the CE/SE simulations (Adiabatic wall), the reference calculations from Weber et al. (Adiabatic and isothermal wall) and the experimental values obtained from Matsuo et al. It can be seen that the CE/SE results follow a trend that predicts the triple-point trajectory similarly to the results of the reference calculations and the experimental results. However, the calculations predict an equilibrium height 20% higher that the experimental one, being similar to the isothermal simulations of Weber et al. who suggested that these discrepancies can have several implications. The first one being a growth of the interacted zone caused by the lower density found in an adiabatic wall boundary layer. The second reason is the lack of a turbulence model in the simulation, therefore, the viscous layer contains less energy and this creates a larger displacement.

Surface heat transfer

To validate the code regarding surface heat transfer, a Mach 17 flow over a 2D cylindrical surface was simulated. The simulations were compared against the LAURA benchmark[48] and the numerical CE/SE results of Chau-Lyan Chang [36]. To accurately predict surface heat transfer, a highly refined mesh near the body surface must be used. Figure 5.22 shows a comparison of cylinder surface heating between the present results, Lee's theory and simulations from the LAURA code and Chau-Lyan Chang. A good agreement with Lee's theory can be seen, the results lay between those of Chang and the LAURA Benchmark.

5.3.2 Air Flows

A case from Knab et al.[49] CV-CV simulations was selected to test the code capabilities regarding real gas effects using the CV-CV model. Air flow around a sphere with 0.1 m in diameter has been simulated, the free-stream conditions are specified by a Mach number of 12.7, a free-stream density of $1.6X10^-3kg/m^3$, and a temperature of 196 K. The initial mass fractions are as follow, $N_2 = 0.7718$, $O_2 = 0.183343$, $O = 0.039827$, and $NO = 0.00503$. Atomic nitrogen is negligible. The CVCV-model parameters have been set to be $U = \frac{E_d}{5R}$ and $\alpha = 0.8$, $\alpha = 0.7$.

With those conditions, the flow is characterised by a strong thermal non-equilibrium, where just behind the shock, vibrational energy modes become excited. In figure 5.23, it can be observed that steep temperature gradients occurring near the wall and shock are captured by the CE/SE simulations accurately. After the shock, the vibrational energy modes become excited by dominant translational-vibrational energy exchange. O_2 dissociation begins and the vibrational energy removal keeps the vibrational temperature of oxygen from overshooting the translational temperature. We can observe that the vibrational temperature of NO is very high and over predicted near the wall, this is an effect of the non-equilibrium modelling of the exchange reactions, nitric oxide is formed in the reverse direction of the exchange reaction $NO + O \leftrightharpoons O_2 + N$, but also destroyed in the reverse direction in

$N_2 + O \leftrightharpoons NO + N$ [49], the CV-CV model predicts the average vibrational energy gain in an endothermic exchange reaction to be greater than the average vibrational energy loss in an exothermic exchange reaction [49], therefore one gets a positive coupling term for $\dot{w}_{v_{NO}}$, leading to an increase in the vibrational temperature of nitric oxide.

An Air flow case from Wen[39] experiments was selected to test the code capabilities regarding real gas effects. The two-temperature model of Park and CV-CV model has been used for this case. The free-stream conditions, free-stream mass fractions and comparison of the heat flux at the stagnation point are listed in table 5.11, 5.12 and 5.13. Good agreement between experimental, theoretical and numerical results is observed.

The temperature profile along the stagnation streamline for the two-temperature model case can be seen in Fig. 5.24. The transfer of energy from initial kinetic energy into various degrees of freedom determines this.Translational and rotational equilibration occur very rapidly, giving a high translational temperature immediately across the shock as all the directed energy of motion is transformed into random translational and rotational energy. Transfer into vibrational excitation takes longer and leads to a lower temperature as the energy is distributed among more degrees of freedom. Dissociation and electronic excitation take longer still, giving yet a further reduction in kinetic temperature, yielding the final equilibrium temperature.
Fig. 5.25 shows a comparison of surface heating between the present results, against Lee's theory, Wen's simulations and experiments[39]. It can be seen that the heat transfer at stagnation point is accurately predicted, corresponding to its maximum value.

Tab. 5.11.: Free-stream conditions of Air flow cases selected from Wen[38].

Case No.	R(m)	ρ_∞ (kg/m^3)	u_∞ (m/s)	T_∞ (K)	T_w (K)
15	0.038	0.0172	5250	2320	500

Tab. 5.12.: Free-stream mass fraction of Air flow cases selected from Wen[38].

Case No.	N_2	O_2	NO	N	O
15	0.739	0.0615	0.0355	1.04E-5	0.151

Tab. 5.13.: Experimental, theoretical and numerical heat transfer at stagnation point, for Air flows.

Case No.	Experiment (Wen & Hornung) [39]	Theory (Wen & Hornung) [39]	2T-CE/SE	CVCV-CE/SE
15	15.3 MW/m^2	15.7 MW/m^2	15.57 MW/m^2	14.17 MW/m^2

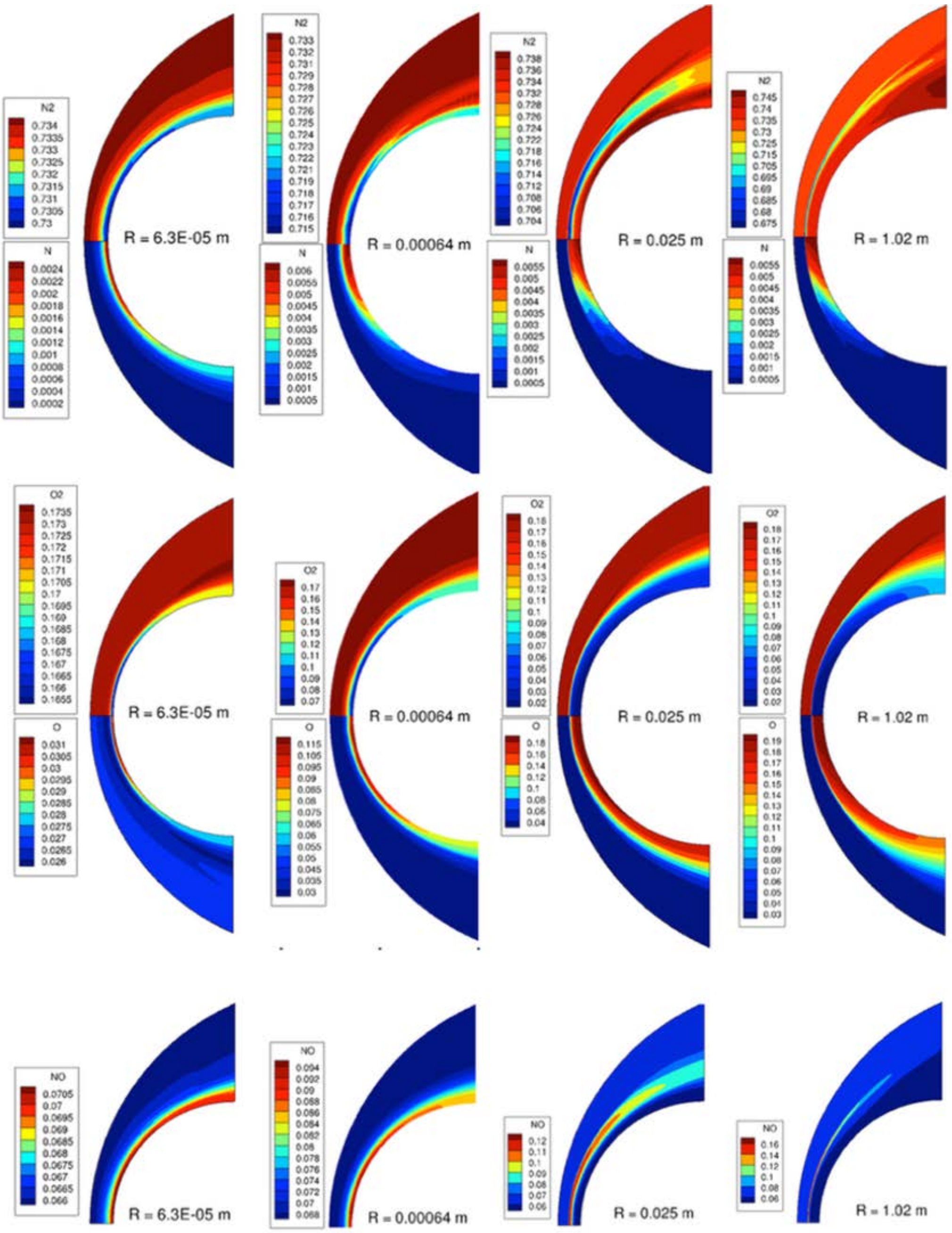

(a) $\widetilde{\Omega} = 1.26$ (b) $\widetilde{\Omega} = 3.48$ (c) $\widetilde{\Omega} = 10.4$ (d) $\widetilde{\Omega} = 62.4$

Fig. 5.9.: Mass fraction of N_2, N, O_2, O and NO molecules for airflows.

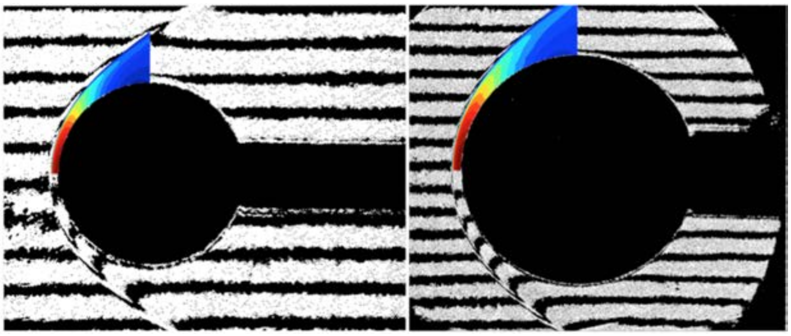

Fig. 5.10.: Comparison of the numerical and experimental shapes of the bow shock for CO_2 flows for case 9 (left) and case 11 (right)

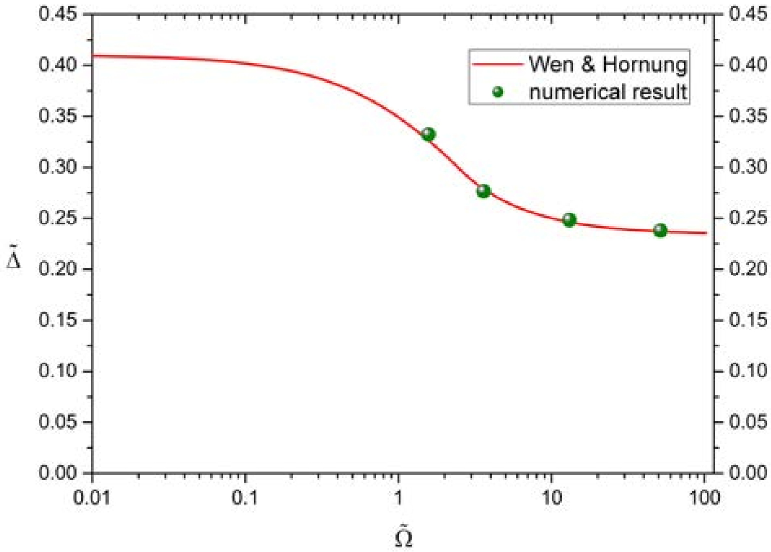

Fig. 5.11.: Comparison of dimensionless shock standoff distance for CO_2 flows

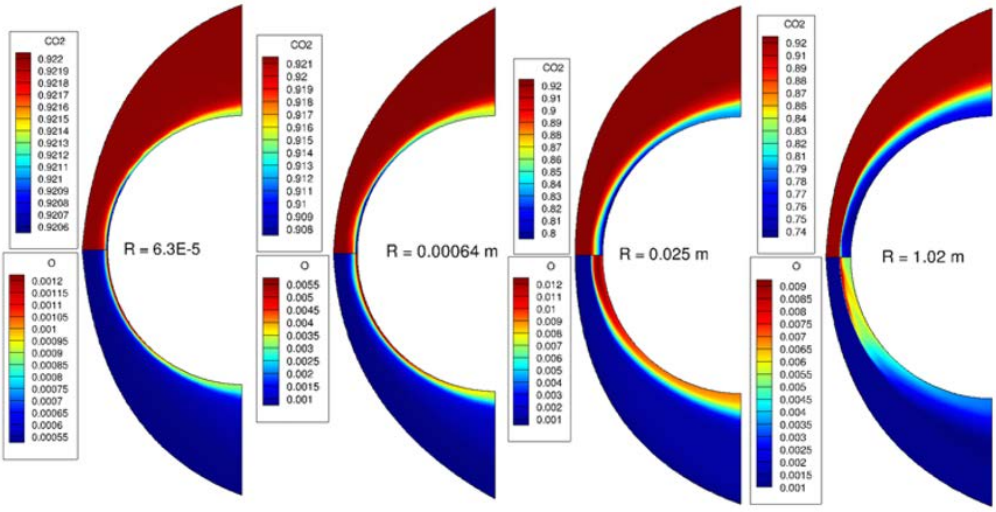

(a) $\widetilde{\Omega} = 1.54$ **(b)** $\widetilde{\Omega} = 3.52$ **(c)** $\widetilde{\Omega} = 12.87$ **(d)** $\widetilde{\Omega} = 50.58$

Fig. 5.12.: Mass fraction of CO_2 molecules (upper) and O atoms (lower) for CO_2 flows.

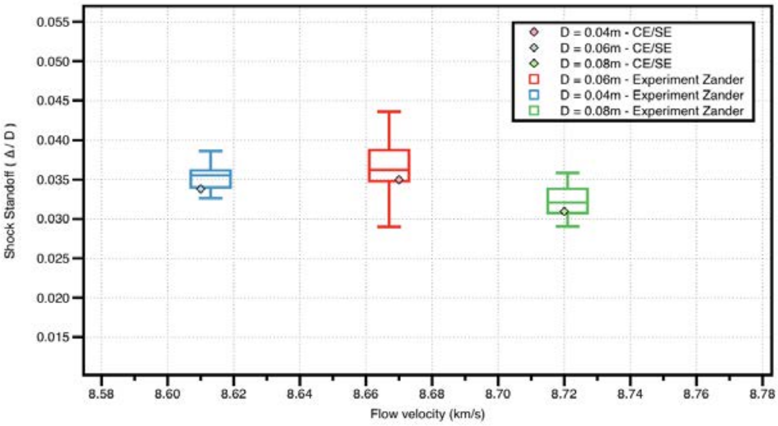

Fig. 5.13.: Comparison of the experimental data by Zander et al.[41] and the CE/SE simulations of shock standoff (Δ/D) distance vs. flow velocity.

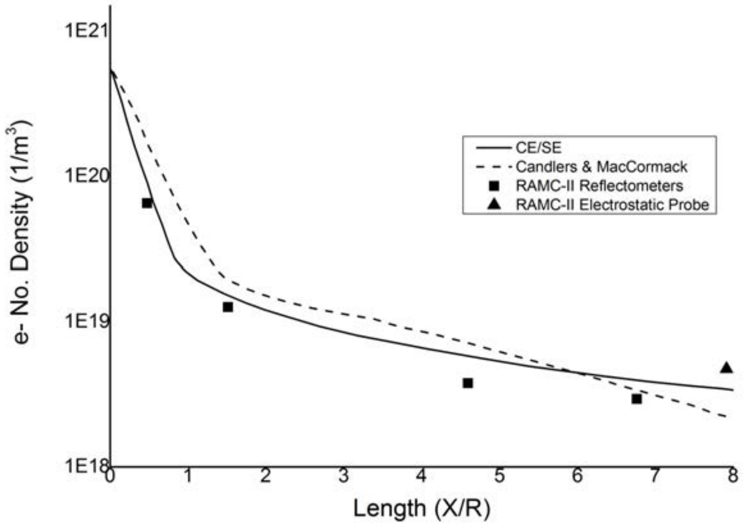

Fig. 5.14.: Electron number density comparisons along the body for RAM-C II flight test at 71 km altitude.

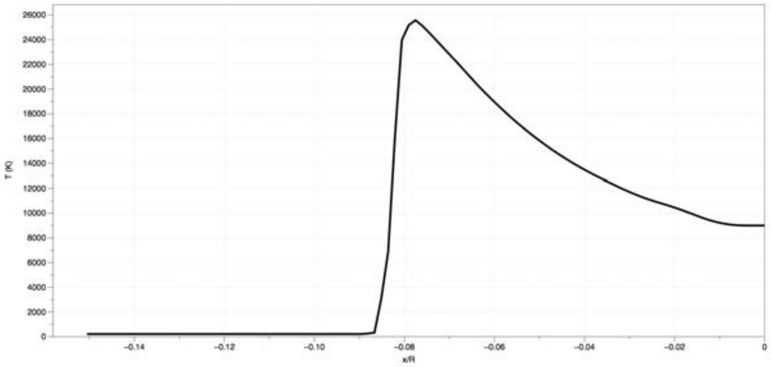

Fig. 5.15.: Translational temperature along the stagnation streamline.

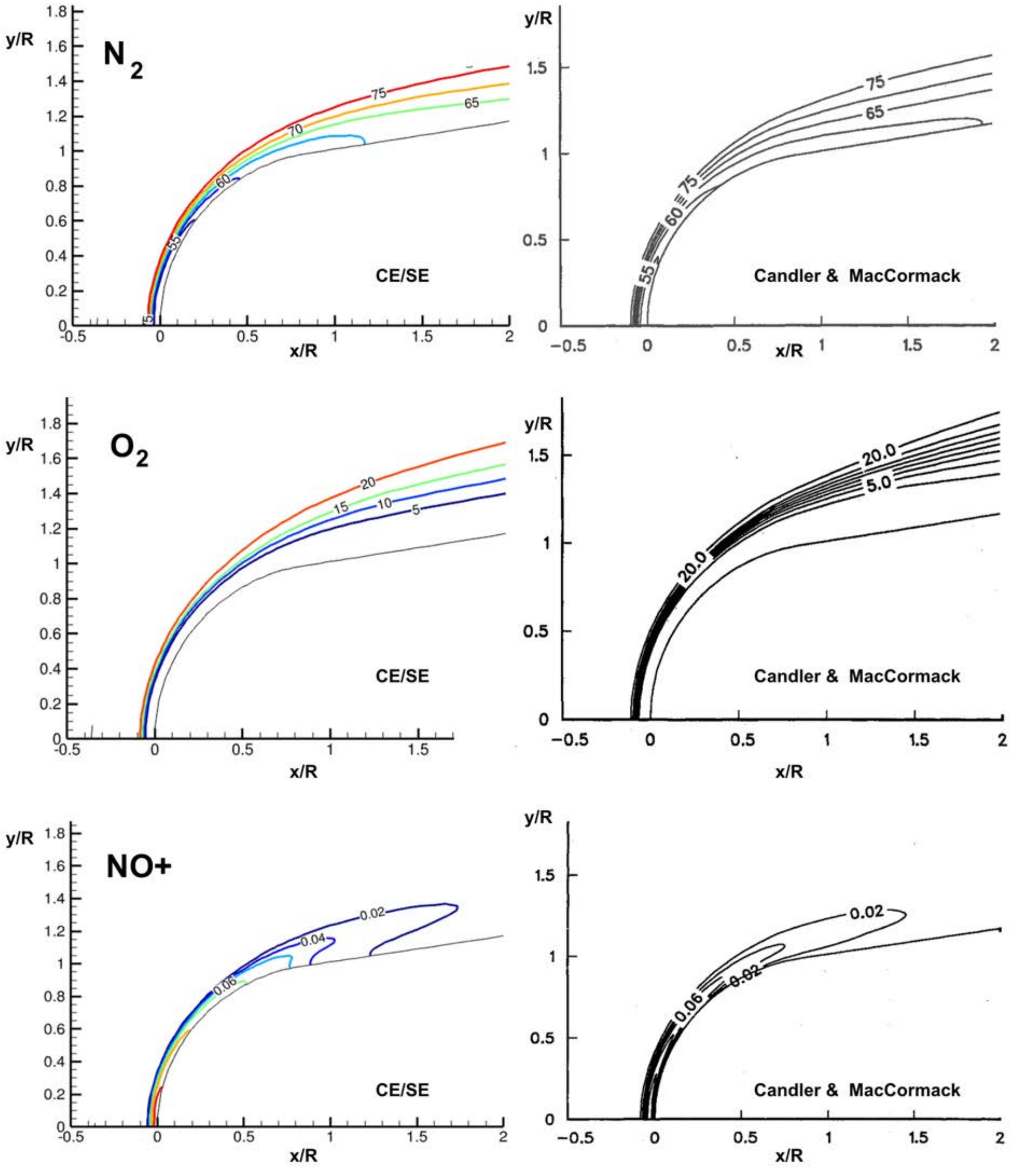

Fig. 5.16.: Mass fraction (%) distributions of O_2, N_2 and NO^+ around the RAM-C capsule at an altitude of 71 km.

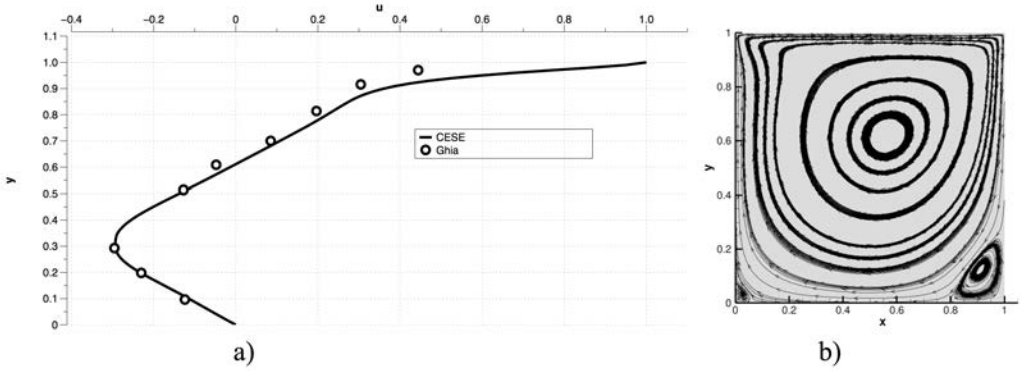

Fig. 5.17.: Comparison of the u-velocity profile along vertical centreline(left) and Streamline contour for a Driven cavity benchmark(right).

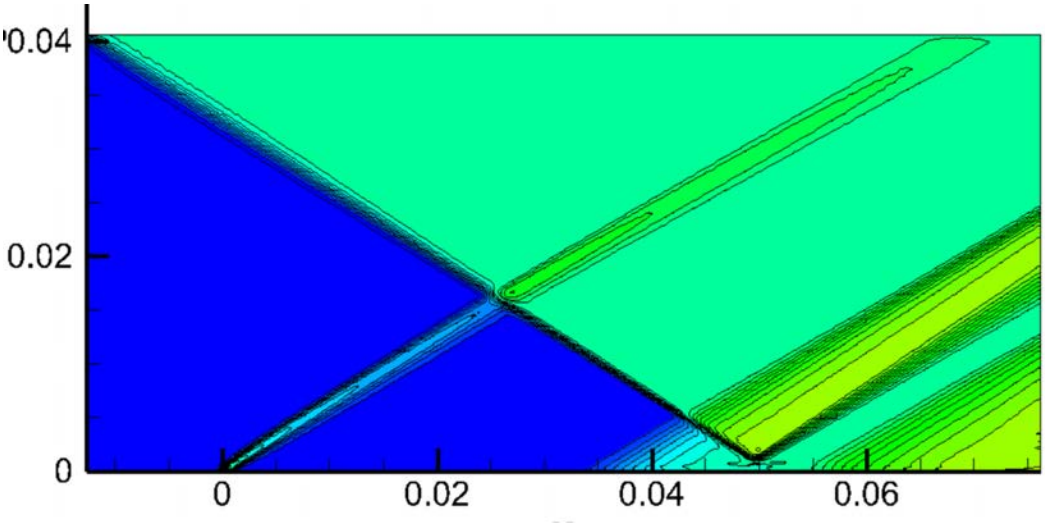

Fig. 5.18.: Pressure contours of the shock boundary layer interaction problem.

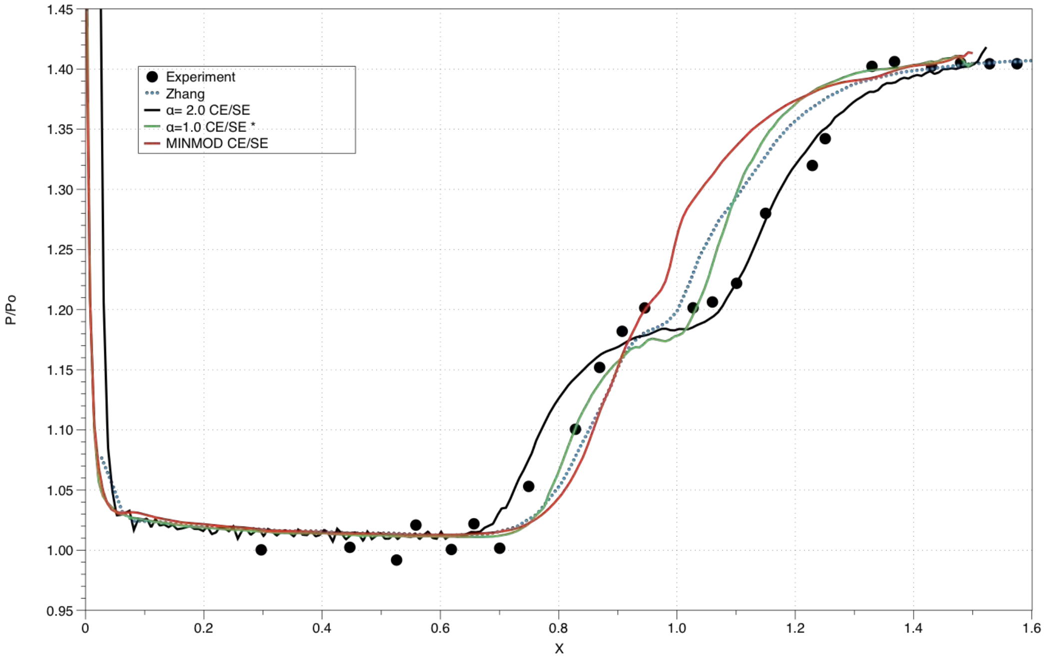

Fig. 5.19.: Pressure distribution along the wall for the Shock/Boundary Layer Interactions validation case.

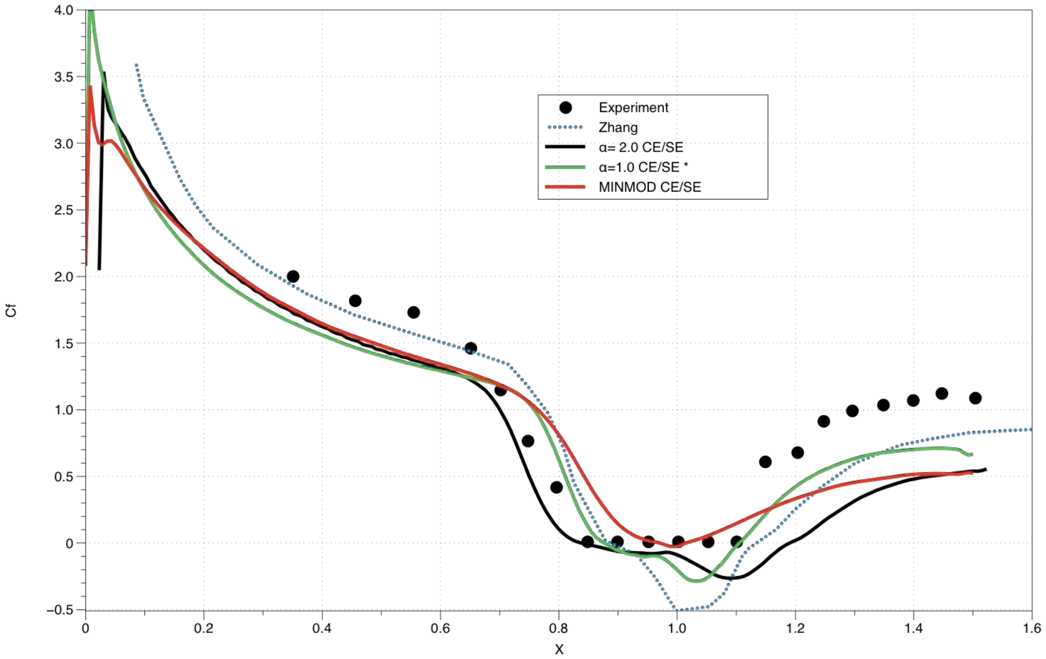

Fig. 5.20.: Skin friction distribution along the wall for the Shock/Boundary Layer Interactions validation case.

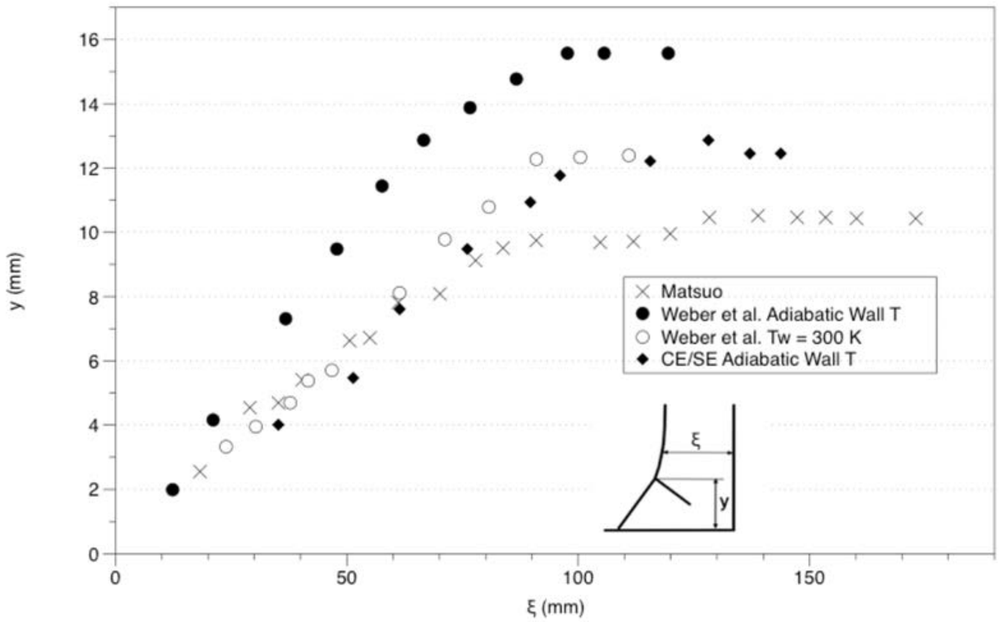

Fig. 5.21.: Comparison of the Variation of the height of the bifurcated foot with distance from the end wall.

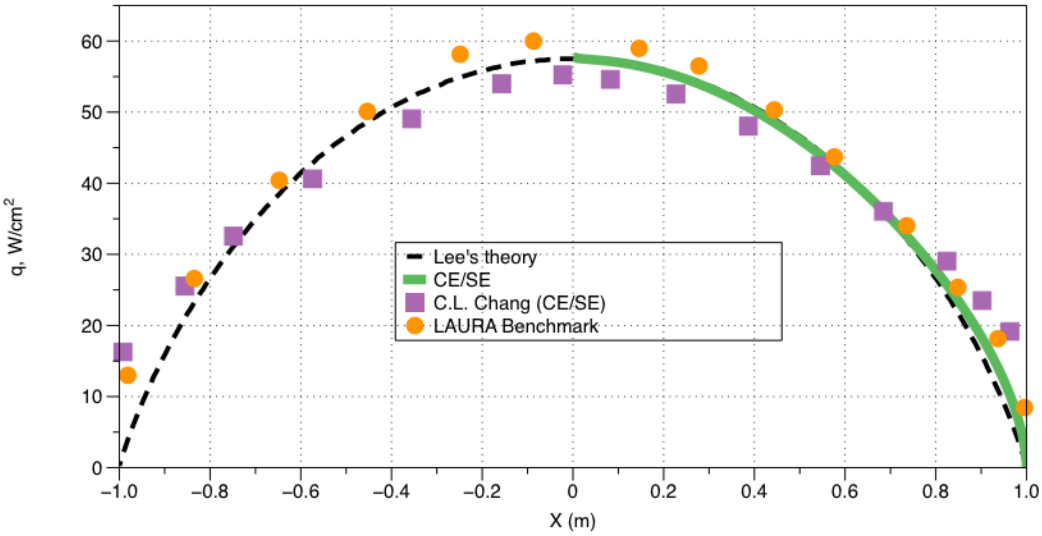

Fig. 5.22.: Comparison of surface heating against the LAURA benchmark[48] and the numerical CE/SE results of Chau-Lyan Chang.

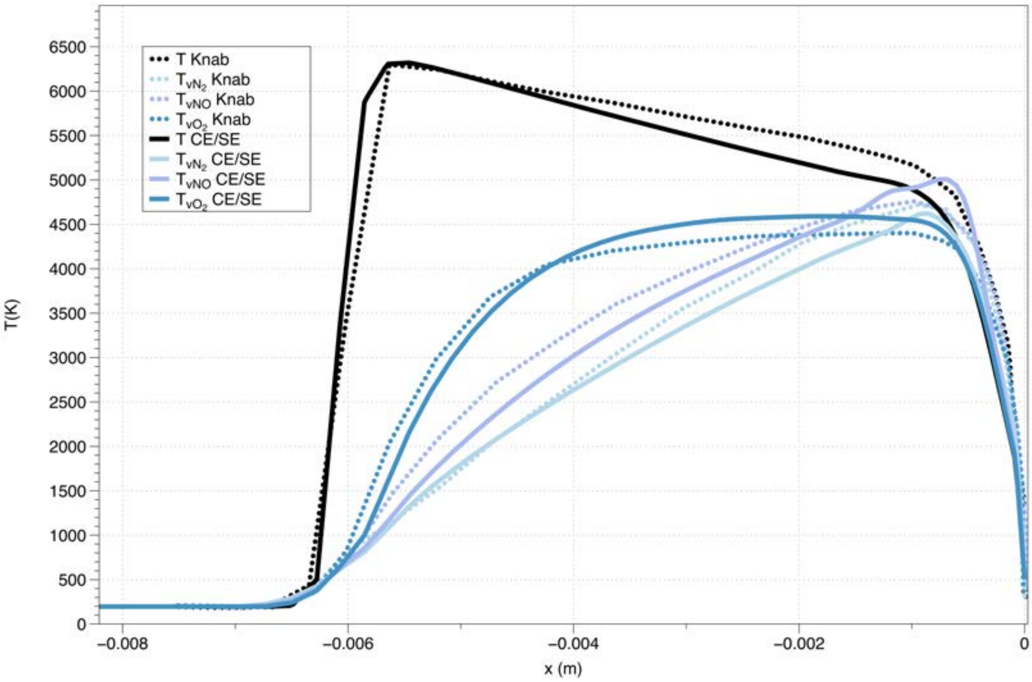

Fig. 5.23.: Comparison of translational and vibrational temperatures along the stagnation streamline of the 0.1m sphere against Knab's simulations.[49] $U_i = \frac{D_i}{5R}$ and $\alpha = 0.8$

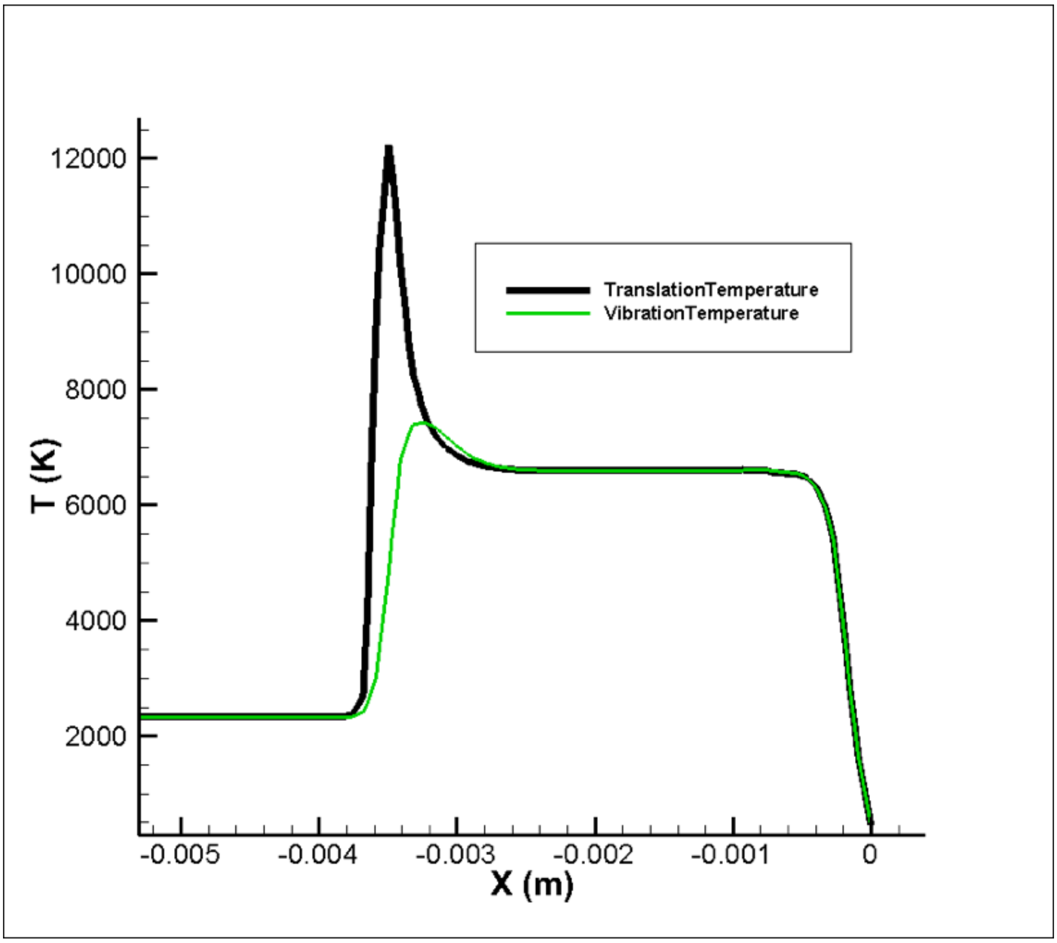

Fig. 5.24.: Temperatures profile along the stagnation streamline.

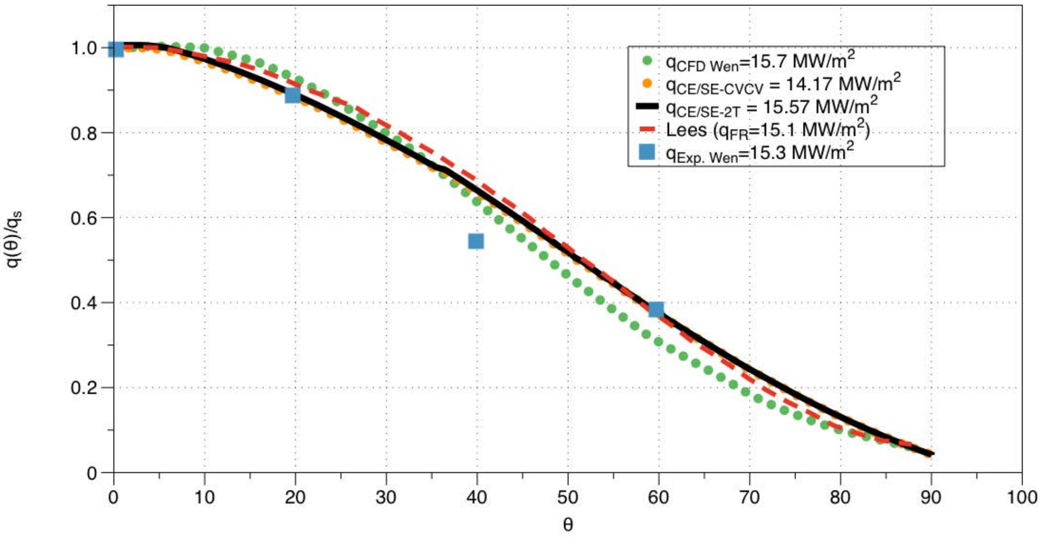

Fig. 5.25.: Comparison of surface heating against Lee's theory, Wen's simulations and experiments.[39]

Conclusion

6

6.1 Conclusions

This work aims to study inviscid and viscous hypersonic dissociating flows over blunt bodies. The work was mostly divided into two parts. The first part focused on inviscid flows. These simulation cases were run for nitrogen, CO_2 and air flows around spheres of different radii, implementing the CE/SE hybrid meshes solver, an in-house code developed by the High-speed Thermo-fluid and MAV/UAV Laboratory team. The main results obtained from this set of simulations are summarised below:

- The code is proved capable of simulating hypersonic flows accurately by comparing the numerical shock standoff distances and bow shock shapes with Wen & Hornung's experimental results and theoretical model.

- The code is proved capable of simulating hypervelocity flows accurately by comparing the numerical shock standoff distances with experimental results by Zander et al.

- Moreover, the code shows good accuracy in simulating chemically reacting ionised flows around the RAM-C II capsule.

The second part of the thesis focused on viscid flows. The simulations were performed in order to calculate the heat transfer and compare the different gas models implemented, two temperature model and CV-CV. The main results obtained are summarised below:

- The code shows good accuracy in predicting viscous flows as shown by comparing the results of a driven cavity with the works done by Ghia et al.

- The code is proved capable of simulating shock patterns and shock bifurcation compared against the experimental results of Matsuo et al. and the numerical results of Weber et al.

- The code is proved capable of capturing the numerical shock standoff distances and bow shock shapes with Wen & Hornung's experimental results and Knab et al. numerical model.

- Moreover, the code shows good accuracy in simulating heat flux in air flows around spheres.

6.2 Future Work

To provide evidence of the code capabilities regarding heat transfer, ionisation, viscous flows and turbulence, further work should focus on the inclusion of a turbulent model and validation of the code regarding air, carbon dioxide and nitrogen viscous and turbulent flows over blunt bodies using real flight data and experimental data provided by the Apollo capsule, FIRE-II and mars reentry capsules. To be able to prove accurate results for asymmetrical complex shapes, an extension to a 3D code is also recommended.

Appendix - Chemistry

A

A.1 Reactions rates data

Tables A.1, A.2 and A.3 present the reaction data used for Nitrogen and air, ionised air and CO_2 models, respectively.

Tab. A.1.: Reaction data used in Nitrogen and Air flows.

Reaction	M	C_f	n	θ_v
$N_2 + M \rightleftharpoons 2N + M$	N_2	3.7E18	-1.6	113200
$N_2 + M \rightleftharpoons 2N + M$	N	1.1E19	-1.6	113200
$N_2 + M \rightleftharpoons 2N + M$	O_2	3.7E18	-1.6	113200
$N_2 + M \rightleftharpoons 2N + M$	O	1.1E19	-1.6	113200
$N_2 + M \rightleftharpoons 2N + M$	NO	3.7E18	-1.6	113200
$O_2 + M \rightleftharpoons 2O + M$	N_2	2.75E16	-1.0	59500
$O_2 + M \rightleftharpoons 2O + M$	N	8.25E16	-1.0	59500
$O_2 + M \rightleftharpoons 2O + M$	O_2	2.75E16	-1.0	59500
$O_2 + M \rightleftharpoons 2O + M$	O	8.25E16	-1.0	59500
$O_2 + M \rightleftharpoons 2O + M$	NO	2.75E16	-1.0	59500
$NO + M \rightleftharpoons N + O + M$	N_2	2.3E14	-0.5	75500
$NO + M \rightleftharpoons N + O + M$	N	4.6E14	-0.5	75500
$NO + M \rightleftharpoons N + O + M$	O_2	2.3E14	-0.5	75500
$NO + M \rightleftharpoons N + O + M$	O	4.6E14	-0.5	75500
$NO + M \rightleftharpoons N + O + M$	NO	2.3E14	-0.5	75500
$NO + O \rightleftharpoons O2 + N$	-	2.16E5	1.29	19220
$N2 + O \rightleftharpoons NO + O$	-	3.18E10	0.1	37700

Tab. A.2.: Reaction data used in Ionised Air flows.

Reaction	M	C_f	n	θ_v
$N_2 + M \rightleftharpoons 2N + M$	N_2	3.7E18	-1.6	113200
$N_2 + M \rightleftharpoons 2N + M$	N	1.1E19	-1.6	113200
$N_2 + M \rightleftharpoons 2N + M$	O_2	3.7E18	-1.6	113200
$N_2 + M \rightleftharpoons 2N + M$	O	1.1E19	-1.6	113200
$N_2 + M \rightleftharpoons 2N + M$	NO	3.7E18	-1.6	113200
$O_2 + M \rightleftharpoons 2O + M$	N_2	2.75E16	-1.0	59500
$O_2 + M \rightleftharpoons 2O + M$	N	8.25E16	-1.0	59500
$O_2 + M \rightleftharpoons 2O + M$	O_2	2.75E16	-1.0	59500
$O_2 + M \rightleftharpoons 2O + M$	O	8.25E16	-1.0	59500
$O_2 + M \rightleftharpoons 2O + M$	NO	2.75E16	-1.0	59500
$NO + M \rightleftharpoons N + O + M$	N_2	2.3E14	-0.5	75500
$NO + M \rightleftharpoons N + O + M$	N	4.6E14	-0.5	75500
$NO + M \rightleftharpoons N + O + M$	O_2	2.3E14	-0.5	75500
$NO + M \rightleftharpoons N + O + M$	O	4.6E14	-0.5	75500
$NO + M \rightleftharpoons N + O + M$	NO	2.3E14	-0.5	75500
$NO + O \rightleftharpoons O2 + N$	-	2.16E5	1.29	19220
$N2 + O \rightleftharpoons NO + O$	-	3.18E10	0.1	37700
$N + O \leftrightharpoons NO^+ + e^-$	-	8.8E8	1.0	31900
$O + O \leftrightharpoons O_2^+ + e^-$	-	7.1E2	2.7	80600
$N + N \leftrightharpoons N_2^+ + e^-$	-	4.4E7	1.5	67500
$O + e^- \leftrightharpoons O^+ + 2e^-$	-	3.9E33	-3.78	158500
$N + e^- \leftrightharpoons N^+ + 2e^-$	-	2.5E34	-3.82	168600
$NO^+ + O \leftrightharpoons N^+ + O_2$	-	1.0E12	0.5	77200
$O_2^+ + N \leftrightharpoons N^+ + O_2$	-	8.7E13	0.14	28600
$O^+ + NO \leftrightharpoons N^+ + O_2$	-	1.4E5	1.9	26600
$O_2^+ + N_2 \leftrightharpoons N_2^+ + O_2$	-	9.9E12	0.0	40700
$O_2^+ + O \leftrightharpoons O^+ + O_2$	-	4.0E12	-0.09	18000
$NO^+ + O_2 \leftrightharpoons O_2^+ + NO$	-	2.4E13	0.41	32600
$NO^+ + O \leftrightharpoons O_2^+ + N$	-	7.2E12	0.29	48600
$O^+ + N_2 \leftrightharpoons N_2^+ + O$	-	9.1E11	0.36	22800
$NO^+ + N \leftrightharpoons N_2^+ + O$	-	7.2E13	0.0	35500

Tab. A.3.: Reaction data used in CO_2 flows.

Reaction	M	C_f	n	θ_v
$CO_2 + M \leftrightharpoons CO + O + M$	CO_2	6.9E21	-1.5	63275
$CO_2 + M \leftrightharpoons CO + O + M$	O	1.4E22	-1.5	63275
$CO_2 + M \leftrightharpoons CO + O + M$	O_2	6.9E21	-1.5	63275
$CO_2 + M \leftrightharpoons CO + O + M$	CO	6.9E21	-1.5	63275
$CO_2 + M \leftrightharpoons CO + O + M$	C	1.4E22	-1.5	63275
$CO + M \leftrightharpoons C + O + M$	CO_2	2.3E20	-1.0	129000
$CO + M \leftrightharpoons C + O + M$	O	3.4E20	-1.0	129000
$CO + M \leftrightharpoons C + O + M$	O_2	2.3E20	-1.0	129000
$CO + M \leftrightharpoons C + O + M$	CO	2.3E20	-1.0	129000
$CO + M \leftrightharpoons C + O + M$	C	3.4E20	-1.0	129000
$O_2 + M \leftrightharpoons O + O + M$	CO_2	2.0E21	-1.50	59750
$O_2 + M \leftrightharpoons O + O + M$	O	1.0E22	-1.50	59750
$O_2 + M \leftrightharpoons O + O + M$	O_2	2.0E21	-1.50	59750
$O_2 + M \leftrightharpoons O + O + M$	CO	2.0E21	-1.50	59750
$O_2 + M \leftrightharpoons O + O + M$	C	1.0E22	-1.50	59750
$CO_2 + O \leftrightharpoons O_2 + CO$	-	2.1E13	0.0	27800
$CO + O \leftrightharpoons O_2 + C$	-	3.9E13	-0.18	69200

B

Appendix-Equilibrium constant data

B.1 Equilibrium constant data

Listing B.1 and B.2 present the equilibrium constant curve fit coefficients for the reactions considered in the air and CO_2 model, respectively.

Listing B.1: Equilibrium Constants Curve Fits for Air flows

```
N2                  Ref–Elm. Gurvich,1978 pt1 p280 pt2 p207.
3 tpis78 N    2.00     0.00     0.00     0.00     0.00 0     28.01340            0.000
200.000   1000.000 7 –2.0 –1.0   0.0   1.0   2.0   3.0   4.0   0.0          8670.104
2.210371497E+04–3.818461820E+02 6.082738360E+00–8.530914410E–03 1.384646189E–05
–9.625793620E–09 2.519705809E–12 0.000000000E+00 7.108460860E+02–1.076003744E+01
1000.000   6000.000 7 –2.0 –1.0   0.0   1.0   2.0   3.0   4.0   0.0          8670.104
5.877124060E+05–2.239249073E+03 6.066949220E+00–6.139685500E–04 1.491806679E–07
–1.923105485E–11 1.061954386E–15 0.000000000E+00 1.283210415E+04–1.586640027E+01
6000.000  20000.000 7 –2.0 –1.0   0.0   1.0   2.0   3.0   4.0   0.0          8670.104
8.310139160E+08–6.420733540E+05 2.020264635E+02–3.065092046E–02 2.486903333E–06
–9.705954110E–11 1.437538881E–15 0.000000000E+00 4.938707040E+06–1.672099740E+03
#
N                   Hf:Cox,1989. Moore,1975. Gordon,1999.
3 g 5/97 N    1.00     0.00     0.00     0.00     0.00 0     14.00670       472680.000
200.000   1000.000 7 –2.0 –1.0   0.0   1.0   2.0   3.0   4.0   0.0          6197.428
0.000000000E+00 0.000000000E+00 2.500000000E+00 0.000000000E+00 0.000000000E+00
0.000000000E+00 0.000000000E+00 0.000000000E+00 5.610463780E+04 4.193905036E+00
1000.000   6000.000 7 –2.0 –1.0   0.0   1.0   2.0   3.0   4.0   0.0          6197.428
8.876501380E+04–1.071231500E+02 2.362188287E+00 2.916720081E–04–1.729515100E–07
4.012657880E–11–2.677227571E–15 0.000000000E+00 5.697351330E+04 4.865231506E+00
6000.000  20000.000 7 –2.0 –1.0   0.0   1.0   2.0   3.0   4.0   0.0          6197.428
5.475181050E+08–3.107574980E+05 6.916782740E+01–6.847988130E–03 3.827572400E–07
–1.098367709E–11 1.277986024E–16 0.000000000E+00 2.550585618E+06–5.848769753E+02
#
O2                  Ref–Elm. Gurvich,1989 pt1 p94 pt2 p9.
3 tpis89 O    2.00     0.00     0.00     0.00     0.00 0     31.99880            0.000
200.000   1000.000 7 –2.0 –1.0   0.0   1.0   2.0   3.0   4.0   0.0          8680.104
–3.425563420E+04 4.847000970E+02 1.119010961E+00 4.293889240E–03–6.836300520E–07
–2.023372700E–09 1.039040018E–12 0.000000000E+00–3.391454870E+03 1.849699470E+01
1000.000   6000.000 7 –2.0 –1.0   0.0   1.0   2.0   3.0   4.0   0.0          8680.104
–1.037939022E+06 2.344830282E+03 1.819732036E+00 1.267847582E–03–2.188067988E–07
2.053719572E–11–8.193467050E–16 0.000000000E+00–1.689010929E+04 1.738716506E+01
6000.000  20000.000 7 –2.0 –1.0   0.0   1.0   2.0   3.0   4.0   0.0          8680.104
4.975294300E+08–2.866106874E+05 6.690352250E+01–6.169959020E–03 3.016396027E–07
–7.421416600E–12 7.278175770E–17 0.000000000E+00 2.293554027E+06–5.530621610E+02
#
O                   D0(O2):Brix,1954. Moore,1976. Gordon,1999.
3 g 5/97 O    1.00     0.00     0.00     0.00     0.00 0     15.99940       249175.003
200.000   1000.000 7 –2.0 –1.0   0.0   1.0   2.0   3.0   4.0   0.0          6725.403
–7.953611300E+03 1.607177787E+02 1.966226438E+00 1.013670310E–03–1.110415423E–06
6.517507500E–10–1.584779251E–13 0.000000000E+00 2.840362437E+04 8.404241820E+00
1000.000   6000.000 7 –2.0 –1.0   0.0   1.0   2.0   3.0   4.0   0.0          6725.403
2.619020262E+05–7.298722030E+02 3.317177270E+00–4.281334360E–04 1.036104594E–07
–9.438304330E–12 2.725038297E–16 0.000000000E+00 3.392428060E+04–6.679585350E–01
6000.000  20000.000 7 –2.0 –1.0   0.0   1.0   2.0   3.0   4.0   0.0          6725.403
1.779004264E+08–1.082328257E+05 2.810778365E+01–2.975232262E–03 1.854997534E–07
–5.796231540E–12 7.191720164E–17 0.000000000E+00 8.890942630E+05–2.181728151E+02
#
NO                  Gurvich,1978,1989 pt1 p326 pt2 p203.
3 tpis89 N    1.00O    1.00     0.00     0.00     0.00 0     30.00610        91271.310
200.000   1000.000 7 –2.0 –1.0   0.0   1.0   2.0   3.0   4.0   0.0          9179.110
–1.143916503E+04 1.536467592E+02 3.431468730E+00–2.668592368E–03 8.481399120E–06
–7.685111050E–09 2.386797655E–12 0.000000000E+00 9.098214410E+03 6.728725490E+00
1000.000   6000.000 7 –2.0 –1.0   0.0   1.0   2.0   3.0   4.0   0.0          9179.110
```

```
2.239018716E+05-1.289651623E+03 5.433936030E+00-3.656034900E-04 9.880966450E-08
-1.416076856E-11 9.380184620E-16 0.000000000E+00 1.750317656E+04-8.501669090E+00
6000.000 20000.000 7 -2.0 -1.0  0.0  1.0  2.0  3.0  4.0  0.0          9179.110
-9.575303540E+08 5.912434480E+05-1.384566826E+02 1.694339403E-02-1.007351096E-06
2.912584076E-11-3.295109350E-16 0.000000000E+00-4.677501240E+06 1.242081216E+03
#
NO+               Cp,S,IP(NO): Gurvich,1989 pt1 p330 pt2 p205.
3 g 5/99 N  1.00O  1.00E  -1.00   0.00   0.00 0     30.00555     990809.704
298.150  1000.000 7 -2.0 -1.0  0.0  1.0  2.0  3.0  4.0  0.0          8670.104
1.398106635E+03-1.590446941E+02 5.122895400E+00-6.394388620E-03 1.123918342E-05
-7.988581260E-09 2.107383677E-12 0.000000000E+00 1.187495132E+05-4.398433810E+00
1000.000  6000.000 7 -2.0 -1.0  0.0  1.0  2.0  3.0  4.0  0.0          8670.104
6.069876900E+05-2.278395427E+03 6.080324670E+00-6.066847580E-04 1.432002611E-07
-1.747990522E-11 8.935014060E-16 0.000000000E+00 1.322709615E+05-1.519880037E+01
6000.000 20000.000 7 -2.0 -1.0  0.0  1.0  2.0  3.0  4.0  0.0          8670.104
2.676400347E+09-1.832948690E+06 5.099249390E+02-7.113819280E-02 5.317659880E-06
-1.963208212E-10 2.805268230E-15 0.000000000E+00 1.443308939E+07-4.324044462E+03
#
e-                Ref-Species. Chase,1998 3/82.
3 g12/98 E  1.00   0.00   0.00   0.00   0.00 0      0.00055         0.000
298.150  1000.000 7 -2.0 -1.0  0.0  1.0  2.0  3.0  4.0  0.0          6197.428
0.000000000E+00 0.000000000E+00 2.500000000E+00 0.000000000E+00 0.000000000E+00
0.000000000E+00 0.000000000E+00 0.000000000E+00-7.453750000E+02-1.172081224E+01
1000.000  6000.000 7 -2.0 -1.0  0.0  1.0  2.0  3.0  4.0  0.0          6197.428
0.000000000E+00 0.000000000E+00 2.500000000E+00 0.000000000E+00 0.000000000E+00
0.000000000E+00 0.000000000E+00 0.000000000E+00-7.453750000E+02-1.172081224E+01
6000.000 20000.000 7 -2.0 -1.0  0.0  1.0  2.0  3.0  4.0  0.0          6197.428
0.000000000E+00 0.000000000E+00 2.500000000E+00 0.000000000E+00 0.000000000E+00
        0.000000000E+00 0.000000000E+00 0.000000000E+00-7.453750000E+02-1.172081224E+01
```

Listing B.2: Equilibrium Constants Curve Fits for CO_2 flows

```
CO2               Gurvich,1991 pt1 p27 pt2 p24.
 3 g 9/99 C  1.00O  2.00   0.00   0.00   0.00 0     44.00950    -393510.000
   200.000  1000.000 7 -2.0 -1.0  0.0  1.0  2.0  3.0  4.0  0.0          9365.469
 4.943650540E+04-6.264116010E+02 5.301725240E+00 2.503813816E-03-2.127308728E-07
-7.689988780E-10 2.849677801E-13 0.000000000E+00-4.528198460E+04-7.048279440E+00
  1000.000  6000.000 7 -2.0 -1.0  0.0  1.0  2.0  3.0  4.0  0.0          9365.469
 1.176962419E+05-1.788791477E+03 8.291523190E+00-9.223156780E-05 4.863676880E-09
-1.891053312E-12 6.330036590E-16 0.000000000E+00-3.908350590E+04-2.652669281E+01
  6000.000 20000.000 7 -2.0 -1.0  0.0  1.0  2.0  3.0  4.0  0.0          9365.469
-1.544423287E+09 1.016847056E+06-2.561405230E+02 3.369401080E-02-2.181184337E-06
 6.991420840E-11-8.842351500E-16 0.000000000E+00-8.043214510E+06 2.254177493E+03
#
O2                Ref-Elm. Gurvich,1989 pt1 p94 pt2 p9.
 3 tpis89 O  2.00   0.00   0.00   0.00   0.00 0     31.99880          0.000
   200.000  1000.000 7 -2.0 -1.0  0.0  1.0  2.0  3.0  4.0  0.0          8680.104
-3.425563420E+04 4.847000970E+02 1.119010961E+00 4.293889240E-03-6.836300520E-07
-2.023372700E-09 1.039040018E-12 0.000000000E+00-3.391454870E+03 1.849699470E+01
  1000.000  6000.000 7 -2.0 -1.0  0.0  1.0  2.0  3.0  4.0  0.0          8680.104
-1.037939022E+06 2.344830282E+03 1.819732036E+00 1.267847582E-03-2.188067988E-07
 2.053719572E-11-8.193467050E-16 0.000000000E+00-1.689010929E+04 1.738716506E+01
  6000.000 20000.000 7 -2.0 -1.0  0.0  1.0  2.0  3.0  4.0  0.0          8680.104
 4.975294300E+08-2.866106874E+05 6.690352250E+01-6.169959020E-03 3.016396027E-07
-7.421416600E-12 7.278175770E-17 0.000000000E+00 2.293554027E+06-5.530621610E+02
#
CO                Gurvich,1979 pt1 p25 pt2 p29.
 3 tpis79 C  1.00O  1.00   0.00   0.00   0.00 0     28.01010    -110535.196
   200.000  1000.000 7 -2.0 -1.0  0.0  1.0  2.0  3.0  4.0  0.0          8671.104
 1.489045326E+04-2.922285939E+02 5.724527170E+00-8.176235030E-03 1.456903469E-05
-1.087746302E-08 3.027941827E-12 0.000000000E+00-1.303131878E+04-7.859241350E+00
  1000.000  6000.000 7 -2.0 -1.0  0.0  1.0  2.0  3.0  4.0  0.0          8671.104
 4.619197250E+05-1.944704863E+03 5.916714180E+00-5.664282830E-04 1.398814540E-07
-1.787680361E-11 9.620935570E-16 0.000000000E+00-2.466261084E+03-1.387413108E+01
  6000.000 20000.000 7 -2.0 -1.0  0.0  1.0  2.0  3.0  4.0  0.0          8671.104
 8.868662960E+08-7.500377840E+05 2.495474979E+02-3.956351100E-02 3.297772080E-06
-1.318409933E-10 1.998937948E-15 0.000000000E+00 5.701421130E+06-2.060704786E+03
#
O                 D0(O2):Brix,1954. Moore,1976. Gordon,1999.
 3 g 5/97 O  1.00   0.00   0.00   0.00   0.00 0     15.99940     249175.003
   200.000  1000.000 7 -2.0 -1.0  0.0  1.0  2.0  3.0  4.0  0.0          6725.403
-7.953611300E+03 1.607177787E+02 1.966226438E+00 1.013670310E-03-1.110415423E-06
 6.517507500E-10-1.584779251E-13 0.000000000E+00 2.840362437E+04 8.404241820E+00
  1000.000  6000.000 7 -2.0 -1.0  0.0  1.0  2.0  3.0  4.0  0.0          6725.403
 2.619020262E+05-7.298722030E+02 3.317177270E+00-4.281334360E-04 1.036104594E-07
-9.438304330E-12 2.725038297E-16 0.000000000E+00 3.392428060E+04-6.679585350E-01
  6000.000 20000.000 7 -2.0 -1.0  0.0  1.0  2.0  3.0  4.0  0.0          6725.403
 1.779004264E+08-1.082328257E+05 2.810778365E+01-2.975232262E-03 1.854997534E-07
-5.796231540E-12 7.191720164E-17 0.000000000E+00 8.890942630E+05-2.181728151E+02
```

```
#
C                         Hf:Douglas,1955. Moore,1970b. Gordon,1999.
 3 g 7/97 C   1.00    0.00    0.00    0.00    0.00 0   12.0107000     716680.000
    200.000   1000.000 7 −2.0 −1.0  0.0  1.0  2.0  3.0  4.0  0.0            6535.895
 6.495031470E+02−9.649010860E−01 2.504675479E+00−1.281448025E−05 1.980133654E−08
−1.606144025E−11 5.314483411E−15 0.000000000E+00 8.545763110E+04 4.747924288E+00
   1000.000   6000.000 7 −2.0 −1.0  0.0  1.0  2.0  3.0  4.0  0.0            6535.895
−1.289136472E+05 1.719528572E+02 2.646044387E+00−3.353068950E−04 1.742092740E−07
−2.902817829E−11 1.642182385E−15 0.000000000E+00 8.410597850E+04 4.130047418E+00
   6000.000  20000.000 7 −2.0 −1.0  0.0  1.0  2.0  3.0  4.0  0.0            6535.895
 4.432528010E+08−2.886018412E+05 7.737108320E+01−9.715281890E−03 6.649595330E−07
−2.230078776E−11 2.899388702E−16 0.000000000E+00 2.355273444E+06−6.405123160E+02
#
```

Appendix-Source Code

C

C.1 Code Description

Usually, shock wave propagation problems are described by classical Navier-Stokes equations or inviscid Euler equations and under the assumptions that the molecules are indistinguishable, small, hard spheres, collisions are elastic, and there are no inter- molecular forces so that the gas can be treated as a perfect gas. The general form of the equations governing 2D inviscid flows can be written as:

$$\frac{\partial}{\partial t}\begin{bmatrix}\rho\\ \rho u_x\\ \rho u_y\\ E\end{bmatrix}+\frac{\partial}{\partial x}\begin{bmatrix}\rho u_x\\ \rho u_x^2+p\\ \rho u_x u_y\\ (E+p)u_x\end{bmatrix}+\frac{\partial}{\partial y}\begin{bmatrix}\rho u_y\\ \rho u_y u_x\\ \rho u_y^2+p\\ (E+p)u_y\end{bmatrix}=0$$

where the pressure, p, is related to the equation of state

$$p=(\gamma-1)(E-\frac{1}{2}\rho(u_x^2+u_y^2))\gamma=1.4$$

A Riemann problem, consists of an initial value problem composed of a conservation equation together with piece wise constant data having a single discontinuity. The Riemann problem is very useful for the understanding of equations like Euler conservation equations because all properties, such as shocks and rarefaction waves, appear as characteristics in the solution. It also gives an exact solution to some complex nonlinear equations, such as the Euler equations. The current code solves a 2D Riemann problem over a computational domain (x,y)=[0,1]x[0,1], with initial conditions given by Fig. C.1 and Dirichlet boundary conditions. The simulation is run until t=0.3, the mesh is 200 x 200 elements and the CFL number equals 0.75.

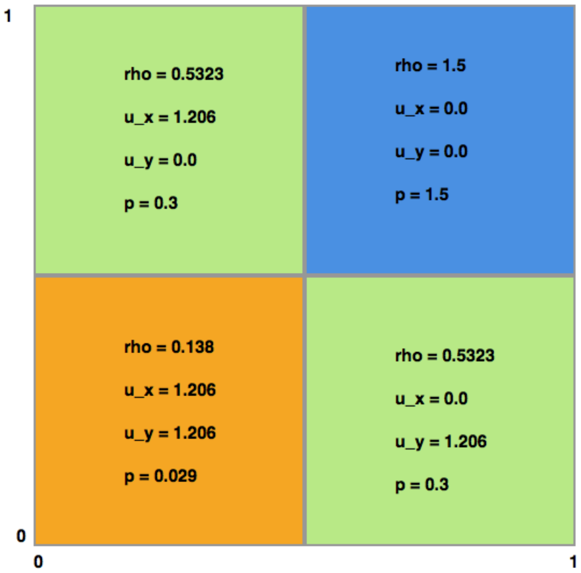

Fig. C.1.: Initial conditions used in the current CE/SE solver

C.2 Source Code

Listing C.1: Sample 2D CESE code

```
#include <iostream>
#include <cmath>
#include <time.h>

using namespace std;

const int M = 300;          // x direction  gridpoints
const int N = 300;          // y direction gridpoints
const double Cf = 0.75;             //  The desired CFL number
const double alpha = 6;             // alpha used to overcome the discontinuities
const double x_1 = 0;
const double x_2 = 1;
const double y_1 = 0;
const double y_2 = 1;
// Fluid properties
const double gama = 1.4;
//initial conditions
#define rho1 0.138
#define u1 1.206
#define v1 1.206
#define p1 0.029

#define rho2 0.5323
#define u2 0.0
#define v2 1.206
#define p2 0.3

#define rho3 1.5
#define u3 0.0
#define v3 0.0
#define p3 1.5

#define rho4 0.5323
#define u4 1.206
#define v4 0.0
#define p4 0.3

double T;     // Time of simulation

double U[M+1][N+1][4],U_p[M+1][N+1][4],dU_dT[M+1][N+1][4],F[M+1][N+1][4],G[M+1][N+1][4],dU_dX[M+1][N+1][4],
     dU_dY[M+1][N+1][4], dF_dT[M+1][N+1][4],dG_dT[M+1][N+1][4], dF_dY[M+1][N+1][4], dG_dX[M+1][N+1][4];

double dx=double(x_2-x_1)/double(M),dy=double(y_2-y_1)/double(N);
```

```
// Define the Courant Condition
double CFL (double U[M+1][N+1][4])
{
    int n,m;
    double max_vel, vel, p,v,u;
    max_vel=1E-8;
    for (m=1;m<=M;m++)
    {
        for (n=1;n<=N;n++)
        {
            u=U[m][n][1]/U[m][n][0];
            v=U[m][n][2]/U[m][n][0];
            p=(gama-1)*(U[m][n][3]-0.5*U[m][n][0]*(u*u+v*v));
            vel = sqrt(gama*p/U[m][n][0])+sqrt(u*u+v*v);
            if (vel>max_vel)max_vel=vel;
        }
    }
    return Cf*dx*dy/(dy*max_vel+dx*max_vel);
}

// Define W_function in function of alpha
double Wfunct(double value_plus, double value_min)
{
    double W;
    W=(pow(fabs(value_plus),alpha)*value_min+pow(fabs(value_min),alpha)*value_plus)/(pow(fabs(value_plus),
         alpha)+pow(fabs(value_min),alpha)+1e-8);
    return W;
}

// Define the initial Values
void Initial_Values(double U[M+1][N+1][4], double U_p[M+1][N+1][4], double dU_dX[M+1][N+1][4], double dU_dY[M
     +1][N+1][4]){
    int m,n,k;
    for (m=0; m<=M; m++) {

        for (n=0; n<N+1; n++) {
            // get the first quarter of the area ——— DONE
            if ((m<=M/2)&&(n<=N/2)) {
                U[m][n][0]=rho1;
                U[m][n][1]=rho1*u1;
                U[m][n][2]=rho1*v1;
                U[m][n][3]=p1/(gama-1)+0.5*rho1*(u1*u1+v1*v1);
            }
            // get the second quarter of the area ——— DONE
            if ((m>M/2)&&(n<=N/2)) {
                U[m][n][0]=rho2;
                U[m][n][1]=rho2*u2;
                U[m][n][2]=rho2*v2;
                U[m][n][3]=p2/(gama-1)+0.5*rho2*(u2*u2+v2*v2);
            }
            // get the third quarter of the area ——— DONE
            if ((m>M/2)&&(n>N/2)) {
                U[m][n][0]=rho3;
                U[m][n][1]=rho3*u3;
                U[m][n][2]=rho3*v3;
                U[m][n][3]=p3/(gama-1)+0.5*rho3*(u3*u3+v3*v3);
            }
            // get the fourth quarter of the area ——— DONE
            if ((m<=M/2)&&(n>N/2)) {
                U[m][n][0]=rho4;
                U[m][n][1]=rho4*u4;
                U[m][n][2]=rho4*v4;
                U[m][n][3]=p4/(gama-1)+0.5*rho4*(u4*u4+v4*v4);
            }
        }
    }

    // get initial Uprime
    for (m=0; m<=M; m++) {
        for (n=0; n<=N; n++) {
            for (k=0; k<4; k++) {
                U_p[m][n][k]=U[m][n][k];
            }
        }
    }
    // get intial dU_dX and dU_dY
    for (m=0; m<M; m++) {
        for (n=0; n<N; n++) {
            for (k=0; k<4; k++) {
```

```
                dU_dY[m][n][k]=dU_dX[m][n][k]=0;
            }
        }
    }
    for(k=0;k<4;k++){
        dU_dX[M][N][k]=0;
        dU_dY[M][N][k]=0;
    }
}

// Define the boundary conditions
void Boundaries (double U[M+1][N+1][4])
{
    int k,m,n;
    for(k=0;k<4;k++)
    {
        for (m=0; m<=M; m++) {
            U[m][0][k]=U[m][1][k];
            U[m][N][k]=U[m][N-1][k];
        }
        for (n=0; n<=N; n++) {
            U[0][n][k]=U[1][n][k];
            U[M][n][k]=U[M-1][n][k];
        }
    }
}

// Asign F from U
void get_F(double U[M+1][N+1][4], double F[M+1][N+1][4])
{
    int n,m ;
    double u, p,v;
    for (m=0; m<=M; m++)
    {
        for (n=0; n<=N; n++)
        {
            u=U[m][n][1]/U[m][n][0];
            v=U[m][n][2]/U[m][n][0];
            p=(gama-1)*(U[m][n][3]-0.5*(U[m][n][1]*U[m][n][1]+U[m][n][2]*U[m][n][2])/U[m][n][0]);
            F[m][n][0]=U[m][n][1];
            F[m][n][1]=U[m][n][0]*u*u+p;
            F[m][n][2]=U[m][n][0]*u*v;
            F[m][n][3]=(U[m][n][3]+p)*u;
        }
    }

}

// Asign G from U
void get_G(double U[M+1][N+1][4], double G[M+1][N+1][4])
{
    int n,m;
    double u, p,v;
    for (m=0; m<=M; m++)
    {
        for (n=0; n<=N; n++)
        {
            u=U[m][n][1]/U[m][n][0];
            v=U[m][n][2]/U[m][n][0];
            p=(gama-1)*(U[m][n][3]-0.5*(U[m][n][1]*U[m][n][1]+U[m][n][2]*U[m][n][2])/U[m][n][0]);
            G[m][n][0]=U[m][n][2];
            G[m][n][1]=U[m][n][0]*u*v;
            G[m][n][2]=U[m][n][0]*v*v+p;
            G[m][n][3]=(U[m][n][3]+p)*v;
        }
    }
}

// Get Dudt, dfdT, dgdt, etc....
void get_derivative_values (double U[M+1][N+1][4],double dU_dX[M+1][N+1][4], double dU_dY[M+1][N+1][4],double
      dU_dT[M+1][N+1][4],double dF_dT[M+1][N+1][4],double dG_dT[M+1][N+1][4],double dF_dY[M+1][N+1][4],double
      dG_dX[M+1][N+1][4])
{
    int n,m;
    double gama_minus_1,gama_minus_3,u,v,a1,a2,a3,a4,a5,a6;
    gama_minus_1=gama-1.0;
    gama_minus_3=gama-3.0;
    for(m=0;m<=M;m++)
    {
        for(n=0;n<=N;n++)
```

```
        {
            u=U[m][n][1]/U[m][n][0];
            v=U[m][n][2]/U[m][n][0];

            a1=(-gama_minus_3*u*u-gama_minus_1*v*v)/2;
            a2=(-gama_minus_3*v*v-gama_minus_1*u*u)/2;
            a3=gama*u*(U[m][n][3]/U[m][n][0])-gama_minus_1*(u*u*u+u*v*v);
            a4=-gama*(U[m][n][3]/U[m][n][0])+(3*u*u+v*v)*gama_minus_1/2;
            a5=gama*v*(U[m][n][3]/U[m][n][0])-gama_minus_1*(v*v*v+u*u*v);
            a6=-gama*(U[m][n][3]/U[m][n][0])+(3*v*v+u*u)*gama_minus_1/2;

            dU_dT[m][n][0]=-dU_dX[m][n][1]-dU_dY[m][n][2];
            dU_dT[m][n][1]=a1*dU_dX[m][n][0]+gama_minus_3*u*dU_dX[m][n][1]+gama_minus_1*v*dU_dX[m][n][2]-
                 gama_minus_1*dU_dX[m][n][3]+u*v*dU_dY[m][n][0]-v*dU_dY[m][n][1]-u*dU_dY[m][n][2];
            dU_dT[m][n][2]=u*v*dU_dX[m][n][0]-v*dU_dX[m][n][1]-u*dU_dX[m][n][2]+a2*dU_dY[m][n][0]+
                 gama_minus_1*u*dU_dY[m][n][1]+gama_minus_3*v*dU_dY[m][n][2]-gama_minus_1*dU_dY[m][n][3];
            dU_dT[m][n][3]=a3*dU_dX[m][n][0]+a4*dU_dX[m][n][1]+gama_minus_1*u*v*dU_dX[m][n][2]-gama*u*dU_dX[m
                 ][n][3]+a5*dU_dY[m][n][0]+gama_minus_1*u*v*dU_dY[m][n][1]+a6*dU_dY[m][n][2]-gama*v*dU_dY[m][
                 n][3];

            dF_dT[m][n][0]=dU_dT[m][n][1];
            dF_dT[m][n][1]=-a1*dU_dT[m][n][0]-gama_minus_3*u*dU_dT[m][n][1]-gama_minus_1*v*dU_dT[m][n][2]+
                 gama_minus_1*dU_dT[m][n][3];
            dF_dT[m][n][2]=-u*v*dU_dT[m][n][0]+v*dU_dT[m][n][1]+u*dU_dT[m][n][2];
            dF_dT[m][n][3]=-a3*dU_dT[m][n][0]-a4*dU_dT[m][n][1]-gama_minus_1*u*v*dU_dT[m][n][2]+gama*u*dU_dT[
                 m][n][3];

            dF_dY[m][n][0]=dU_dY[m][n][1];
            dF_dY[m][n][1]=-a1*dU_dY[m][n][0]-gama_minus_3*u*dU_dY[m][n][1]-gama_minus_1*v*dU_dY[m][n][2]+
                 gama_minus_1*dU_dY[m][n][3];
            dF_dY[m][n][2]=-u*v*dU_dY[m][n][0]+v*dU_dY[m][n][1]+u*dU_dY[m][n][2];
            dF_dY[m][n][3]=-a3*dU_dY[m][n][0]-a4*dU_dY[m][n][1]-gama_minus_1*u*v*dU_dY[m][n][2]+gama*u*dU_dY[
                 m][n][3];

            dG_dT[m][n][0]=dU_dT[m][n][2];
            dG_dT[m][n][1]=-u*v*dU_dT[m][n][0]+v*dU_dT[m][n][1]+u*dU_dT[m][n][2];
            dG_dT[m][n][2]=-a2*dU_dT[m][n][0]-gama_minus_1*u*dU_dT[m][n][1]-gama_minus_3*v*dU_dT[m][n][2]+
                 gama_minus_1*dU_dT[m][n][3];
            dG_dT[m][n][3]=-a5*dU_dT[m][n][0]-gama_minus_1*u*v*dU_dT[m][n][1]-a6*dU_dT[m][n][2]+gama*v*dU_dT[
                 m][n][3];

            dG_dX[m][n][0]=dU_dX[m][n][2];
            dG_dX[m][n][1]=-u*v*dU_dX[m][n][0]+v*dU_dX[m][n][1]+u*dU_dX[m][n][2];
            dG_dX[m][n][2]=-a2*dU_dX[m][n][0]-gama_minus_1*u*dU_dX[m][n][1]-gama_minus_3*v*dU_dX[m][n][2]+
                 gama_minus_1*dU_dX[m][n][3];
            dG_dX[m][n][3]=-a5*dU_dX[m][n][0]-gama_minus_1*u*v*dU_dX[m][n][1]-a6*dU_dX[m][n][2]+gama*v*dU_dX[
                 m][n][3];

        }
    }
}



// Get dudx for complete time step
void dU_dX_n(double U[M+1][N+1][4],double U_p[M+1][N+1][4],double dU_dX[M+1][N+1][4],double dU_dT[M+1][N
      +1][4],double dt)
{
    int m,n,k;
    double dU_dX_plus,dU_dX_min,dx;
    dx=(double(x_2-x_1))/double(M);
    for(m=1;m<=M;m++)
    {
        for(n=1;n<=N;n++)
        {
            for(k=0;k<4;k++)
            {
                dU_dX_plus=(U_p[m][n-1][k]+dU_dT[m][n-1][k]*dt/2+U_p[m][n][k]+dU_dT[m][n][k]*dt/2-2*U[m][n][k
                      ])/dx;
                dU_dX_min=-(U_p[m-1][n-1][k]+dU_dT[m-1][n-1][k]*dt/2+U_p[m-1][n][k]+dU_dT[m-1][n][k]*dt/2-2*U
                      [m][n][k])/dx;
                dU_dX[m][n][k]=Wfunct(dU_dX_plus, dU_dX_min);
            }
        }
    }
}

// Get dudy for complete time step
```

```
void dU_dY_n(double U[M+1][N+1][4],double U_p[M+1][N+1][4],double dU_dY[M+1][N+1][4],double dU_dT[M+1][N
      +1][4],double dt)
{
    int m,n,k;
    double dU_dY_plus,dU_dY_min,dy;
    dy=(double(y_2-y_1))/double(N);
    for(m=1;m<M;m++)
    {
        for(n=1;n<N;n++)
        {
            for(k=0;k<4;k++)
            {
                dU_dY_plus=(U_p[m][n][k]+dU_dT[m][n][k]*dt/2+U_p[m-1][n][k]+dU_dT[m-1][n][k]*dt/2-2*U[m][n][k
                      ])/dy;
                dU_dY_min=-(U_p[m-1][n-1][k]+dU_dT[m-1][n-1][k]*dt/2+U_p[m][n-1][k]+dU_dT[m][n-1][k]*dt/2-2*U
                      [m][n][k])/dy;
                dU_dY[m][n][k]=Wfunct(dU_dY_plus, dU_dY_min);
            }
        }
    }
}

// Get dudx for half time step
void dU_dX_p(double U[M+1][N+1][4],double U_p[M+1][N+1][4],double dU_dX[M+1][N+1][4],double dU_dT[M+1][N
      +1][4],double dt)
{
    int m,n,k;
    double dU_dX_plus,dU_dX_min,dx;
    dx=(double(x_2-x_1))/double(M);
    for(m=1;m<M;m++)
    {
        for(n=1;n<N;n++)
        {
            for(k=0;k<4;k++)
            {
                dU_dX_plus=(U[m+1][n+1][k]+dU_dT[m+1][n+1][k]*dt/2+U[m+1][n][k]+dU_dT[m+1][n][k]*dt/2-2*U_p[m
                      ][n][k])/dx;
                dU_dX_min=-(U[m][n+1][k]+dU_dT[m][n+1][k]*dt/2+U[m][n][k]+dU_dT[m][n][k]*dt/2-2*U_p[m][n][k])
                      /dx;
                dU_dX[m][n][k]=Wfunct(dU_dX_plus, dU_dX_min);
            }
        }
    }
}

// Get dudy for half time step

void dU_dY_p(double U[M+1][N+1][4],double U_p[M+1][N+1][4],double dU_dY[M+1][N+1][4],double dU_dT[M+1][N
      +1][4],double dt)
{
    int m,n,k;
    double dU_dY_plus,dU_dY_min,dy;
    dy=(double(y_2-y_1))/double(N);
    for(m=1;m<M;m++)
    {
        for(n=1;n<N;n++)
        {
            for(k=0;k<4;k++)
            {
                dU_dY_plus=(U[m+1][n+1][k]+dU_dT[m+1][n+1][k]*dt/2+U[m][n+1][k]+dU_dT[m][n+1][k]*dt/2-2*U_p[m
                      ][n][k])/dy;
                dU_dY_min=-(U[m][n][k]+dU_dT[m][n][k]*dt/2+U[m+1][n][k]+dU_dT[m+1][n][k]*dt/2-2*U_p[m][n][k])
                      /dy;
                dU_dY[m][n][k]=Wfunct(dU_dY_plus, dU_dY_min);
            }
        }
    }
}

void CE_SE (double U[M+1][N+1][4],double U_p[M+1][N+1][4],double dU_dX[M+1][N+1][4],double dU_dY[M+1][N
      +1][4],double dU_dT[M+1][N+1][4],double F[M+1][N+1][4],double dF_dY[M+1][N+1][4],double dF_dT[M+1][N
      +1][4],double G[M+1][N+1][4],double dG_dX[M+1][N+1][4],double dG_dT[M+1][N+1][4])
{
    int m,n,k;
    double dt,t,dx,dy,U1,G1,F1;
    dx=(double(x_2-x_1))/double(M);
    dy=(double(y_2-y_1))/double(N);
    t=0;
    Initial_Values(U, U_p, dU_dX, dU_dY);
    while(t<T)
```

```
    {
        dt=CFL(U);
        t=t+dt;
        printf("t=%f\n",t);
        Boundaries(U);
        get_F(U,F);
        get_G(U,G);
        get_derivative_values (U,dU_dX,dU_dY,dU_dT,dF_dT,dG_dT,dF_dY,dG_dX);
        // GET U
        for(m=0;m<M;m++) // To get U_prime
        {
            for(n=0;n<N;n++)
            {
                for(k=0;k<4;k++)
                {
                    U1=U[m][n][k]+0.25*dx*dU_dX[m][n][k]+0.25*dy*dU_dY[m][n][k]+U[m+1][n][k]-0.25*dx*dU_dX[m
                          +1][n][k]+0.25*dy*dU_dY[m+1][n][k]+U[m+1][n+1][k]-0.25*dx*dU_dX[m+1][n+1][k]-0.25*dy
                          *dU_dY[m+1][n+1][k]+U[m][n+1][k]+0.25*dx*dU_dX[m][n+1][k]-0.25*dy*dU_dY[m][n+1][k];

                    G1=G[m][n][k]+0.25*dx*dG_dX[m][n][k]+0.25*dt*dG_dT[m][n][k]+G[m+1][n][k]-0.25*dx*dG_dX[m
                          +1][n][k]+0.25*dt*dG_dT[m+1][n][k]-G[m+1][n+1][k]+0.25*dx*dG_dX[m+1][n+1][k]-0.25*dt
                          *dG_dT[m+1][n+1][k]-G[m][n+1][k]-0.25*dx*dG_dX[m][n+1][k]-0.25*dt*dG_dT[m][n+1][k];

                    F1=F[m][n][k]+0.25*dy*dF_dY[m][n][k]+0.25*dt*dF_dT[m][n][k]-F[m+1][n][k]-0.25*dy*dF_dY[m
                          +1][n][k]-0.25*dt*dF_dT[m+1][n][k]-F[m+1][n+1][k]+0.25*dy*dF_dY[m+1][n+1][k]-0.25*dt
                          *dF_dT[m+1][n+1][k]+F[m][n+1][k]-0.25*dy*dF_dY[m][n+1][k]+0.25*dt*dF_dT[m][n+1][k];

                    U_p[m][n][k]=0.25*U1+(0.25*dt/dy)*G1+(0.25*dt/dx)*F1;
                }
            }
        }
        dU_dX_p(U,U_p,dU_dX,dU_dT,dt);
        dU_dY_p(U,U_p,dU_dY,dU_dT,dt);
        get_F(U_p,F);
        get_G(U_p,G);
        get_derivative_values (U_p,dU_dX,dU_dY,dU_dT,dF_dT,dG_dT,dF_dY,dG_dX);

        for(m=1;m<M;m++) // To get U
        {
            for(n=1;n<N;n++)
            {
                for(k=0;k<4;k++)
                {
                    U1=U_p[m-1][n-1][k]+0.25*dx*dU_dX[m-1][n-1][k]+0.25*dy*dU_dY[m-1][n-1][k]+U_p[m][n-1][k
                          ]-0.25*dx*dU_dX[m][n-1][k]+0.25*dy*dU_dY[m][n-1][k]+U_p[m][n][k]-0.25*dx*dU_dX[m][n
                          ][k]-0.25*dy*dU_dY[m][n][k]+U_p[m-1][n][k]+0.25*dx*dU_dX[m-1][n][k]-0.25*dy*dU_dY[m
                          -1][n][k];

                    G1=G[m-1][n-1][k]+0.25*dx*dG_dX[m-1][n-1][k]+0.25*dt*dG_dT[m-1][n-1][k]+G[m][n-1][k
                          ]-0.25*dx*dG_dX[m][n-1][k]+0.25*dt*dG_dT[m][n-1][k]-G[m][n][k]+0.25*dx*dG_dX[m][n][k
                          ]-0.25*dt*dG_dT[m][n][k]-G[m-1][n][k]-0.25*dx*dG_dX[m-1][n][k]-0.25*dt*dG_dT[m-1][n
                          ][k];

                    F1=F[m-1][n-1][k]+0.25*dy*dF_dY[m-1][n-1][k]+0.25*dt*dF_dT[m-1][n-1][k]-F[m][n-1][k
                          ]-0.25*dy*dF_dY[m][n-1][k]-0.25*dt*dF_dT[m][n-1][k]-F[m][n][k]+0.25*dy*dF_dY[m][n][k
                          ]-0.25*dt*dF_dT[m][n][k]+F[m-1][n][k]-0.25*dy*dF_dY[m-1][n][k]+0.25*dt*dF_dT[m-1][n
                          ][k];

                    U[m][n][k]=0.25*U1+(0.25*dt/dy)*G1+(0.25*dt/dx)*F1;
                }
            }
        }
        Boundaries(U);
        dU_dX_n(U,U_p,dU_dX,dU_dT,dt);
        dU_dY_n(U,U_p,dU_dY,dU_dT,dt);

    }
}
void Output(double U[M+1][N+1][4])
{
    int m, n;
    double x,y,dx,dy;
    dx=(double(x_2-x_1))/double(M);
    dy=(double(y_2-y_1))/double(N);
    FILE *fp;
    double rho,u,v,p;
    fp=fopen("result.dat","w+");
    fprintf(fp,"%2.30s\n %20.60s\n %20.18s\t %2.3d\t %2.18s\t %2.3d\t %2.18s\n","TITLE = \"2D-EULER.dat\"","
          variables = \"x\", \"y\", \"rho\", \"u\", \"v\", \"p\"","zone i=", M+1,"j=",N+1,"f=point");
    for(m=0;m<M+1;m++)
```

```
    {
        for(n=0;n<N+1;n++)
        {
            x=x_1+m*dx;
            y=y_1+n*dy;
            rho=U[m][n][0];
            u=U[m][n][1]/U[m][n][0];
            v=U[m][n][2]/U[m][n][0];
            p=(gama-1)*(U[m][n][3]-0.5*U[m][n][0]*(u*u+v*v));
            fprintf(fp,"%20.5f\t %20.5f\t %20.5f\t %20.5f\t %20.5f\t %20.5f\n",x,y,rho,u,v,p);
        }
    }
    fclose(fp);
}
// Write the output file


// Implement the code
int main()
{
    std::cout << "Define the simulation time => ";
    std::cin >> T;
    clock_t start,finish;
    double duration;
    start=clock();
    CE_SE(U,U_p,dU_dX,dU_dY,dU_dT,F,dF_dY,dF_dT,G,dG_dX,dG_dT);
    Output(U);
    finish=clock();
    duration=(double)(finish-start)/CLOCKS_PER_SEC;
    cout << "Complete in \n" << duration << "s \n";
    return 0;
}
```

Bibliography

[1] R.D. Launius and D.R. Jenkins. *Coming Home: Reentry and Recovery from Space*. NASA, 2012 (cit. on p. 1).

[2] J.D. Anderson. *Modern Compressible Flow with Historical Perspective*. McGraw-Hill Education, 2003 (cit. on p. 2).

[3] J.D. Anderson. *Hypersonic and high temperature gas dynamics*. American Institute of Aeronautics and Astronautics, 2000 (cit. on p. 2).

[4] S.C. Chang. „The Method of Space-Time Conservation Element and Solution Element-a New Approach for Solving the Navier-Stokes and Euler Equations". In: *Journal of Computational Physics* 119 (1995), pp. 295–324 (cit. on pp. 4, 5, 21).

[5] Z.C. Zhang, S. Yu, X.Y. Wang, S.C. Chang, and P. Jorgenson. „The space-time CE/SE method for the Navier-Stokes equations in three spatial dimensions". In: *Fluids 2000 Conference and Exhibit, AIAA 2000-2331* (2000), pp. 1–7 (cit. on pp. 4, 5).

[6] S.C. Chang, X.Y. Wang, and C.Y. Chow. „The Space-Time Conservation Element and Solution Element Method: A New High-Resolution and Genuinely Multidimensional Paradigm for Solving Conservation Laws". In: *Journal of Computational Physics* 156 (1999), pp. 89–136 (cit. on pp. 4, 5).

[7] Z.C. Zhang, S.T.J. Yu, and S.C. Chang. „A Space-Time Conservation Element and Solution Element Method for Solving the Two- and Three-Dimensional Unsteady Euler Equations Using Quadrilateral and Hexahedral Meshes". In: *Journal of Computational Physics* 175.1 (2002), pp. 168–199 (cit. on p. 4).

[8] S.C. Chang. „New Developments in the Method of Space-Time Conservation Element and Solution Element - Applications to the Euler and Navier-Stokes Equations". In: 106226 (2011), pp. 1–5 (cit. on p. 5).

[9] H. Shen, C.Y. Wen, K.X. Liu, and D.L. Zhang. „Robust high-order space-time conservative schemes for solving conservation laws on hybrid meshes". In: *Journal of Computational Physics* 281 (2015), pp. 375–402 (cit. on pp. 5, 22, 26).

[10] H. Shen, C.Y. Wen, and H. Saldivar Massimi. „Application of CE/SE Method to Study Hypersonic Non-equilibrium Flows over Spheres“. In: *19th AIAA International Space Planes and Hypersonic Systems and Technologies Conference* (2014), pp. 1–16 (cit. on p. 5).

[11] H. Saldivar Massimi, H. Shen, and C.Y. Wen. „Numerical Simulation of Ionized Hypersonic Flows using the Space-Time CE/SE Method“. In: *20th AIAA International Space Planes and Hypersonic Systems and Technologies Conference*. International Space Planes and Hypersonic Systems and Technologies Conferences. American Institute of Aeronautics and Astronautics, July 2015 (cit. on p. 5).

[12] H. Saldivar Massimi, H. Shen, and C.Y. Wen. „Study of Hypersonic Dissociating Flows over Spheres using the Space-Time CE/SE Method“. In: *30th International Symposium on Shock Waves* (2015) (cit. on p. 5).

[13] O. Knab, H. Frühauf, and E. W. Messerschmid. „Theory and validation of the physically consistent coupled vibration-chemistry-vibration model“. In: *Journal of Thermophysics and Heat Transfer* 9.2 (1995), pp. 219–226 (cit. on pp. 5, 15, 16, 18).

[14] C. Park. „Assessment of two-temperature kinetic model for ionizing air“. In: *Journal of Thermophysics and Heat Transfer* 3.3 (1989), pp. 233–244 (cit. on pp. 5, 15).

[15] C.R. Wilke. „A viscosity equation for gas mixtures“. In: *Journal of Chemical Physics* 18 (1950), pp. 517–519 (cit. on p. 12).

[16] F.G. Blottner, M. Johnson, and M. Ellis. *Chemicaly Reacting Viscous Flow Program for Multi-Component Gas Mixtures*. Tech. rep. Sandia Labs., Albuquerque, N. Mex., 1971 (cit. on p. 13).

[17] L.C. Scalabrin. „Numerical Simulaiton of weakly ionized hypersonic flow over reentry capsules“. In: *Education* 130.4 (2007), p. 2508 (cit. on p. 13).

[18] W.G.Vincenti and C.H. Kruger. *Introduction to Physical Gas Dynamics*. Krieger Publishing Company, 1982 (cit. on pp. 13, 18).

[19] C. Park. „Radiation enhancement by nonequilibrium in earth's atmosphere“. In: *Journal of Spacecraft and Rockets* 22.1 (1985), pp. 27–36 (cit. on p. 13).

[20] P.A. Gnoffo and R.S. McCandless. „Three-dimensional AOTV flowfields in chemical nonequilibrium“. In: (1986) (cit. on p. 15).

[21] C.P. Li. *Implicit methods for Computing chemically reacting flows* (cit. on p. 15).

[22] C. Park. „Problems of rate chemistry in the flight regimes of aeroassisted orbital transfer vehicles“. In: (1985) (cit. on p. 15).

[23] J.H. Lee. „Basic governing equations for the flight regimes of aeroassisted orbital transfer vehicles“. In: (1985) (cit. on pp. 15, 18).

[24] C. Park. „The Limits of Two-Temperature Kinetic Model in Air“. In: *48th AIAA Aerospace Sciences Meeting Including the New Horizons Forum and Aerospace Exposition*. Aerospace Sciences Meetings. American Institute of Aeronautics and Astronautics, Jan. 2010 (cit. on p. 16).

[25] C. Park. „Assessment of two-temperature kinetic model for ionizing air“. In: *Journal of Thermophysics and Heat Transfer* 3.3 (1989), pp. 233–244 (cit. on p. 16).

[26] B.J. McBride, M.J. Zehe, and S. Gordon. „NASA Glenn coefficients for calculating thermodynamic properties of individual species“. In: (2002) (cit. on p. 16).

[27] C. Park. *Nonequilibrium hypersonic aerothermodynamics*. Wiley, 1990 (cit. on pp. 16, 19, 52).

[28] P. Hammerling, J.D. Teare, and B. Kivel. „Theory of radiation from luminous shock waves in nitrogen“. In: *Physics of Fluids (1958-1988)* 2.4 (1959), pp. 422–426 (cit. on p. 16).

[29] P.V. Marrone and C.E. Treanor. „Chemical relaxation with preferential dissociation from excited vibrational levels“. In: *Physics of Fluids (1958-1988)* 6.9 (1963), pp. 1215–1221 (cit. on p. 16).

[30] H. Koo, V. Raman, and P.L. Varghese. „Direct numerical simulation of supersonic combustion with thermal nonequilibrium“. In: *Proceedings of the Combustion Institute* 35.2 (2015), pp. 2145–2153 (cit. on p. 17).

[31] R.C. Millikan and D.R. White. „Systematics of vibrational relaxation“. In: *The Journal of chemical physics* 39.12 (1963), pp. 3209–3213 (cit. on p. 18).

[32] D. Hash, J. Olejniczak, M. Wright, et al. „Fire ii calculations for hypersonic nonequilibrium aerothermodynamics code verification: Dplr, laura, and us3d“. In: *45th AIAA Aerospace Sciences Meeting and Exhibit, Reno, NV, Paper No. AIAA-2007-605*. 2007 (cit. on p. 19).

[33] S.G. Rock, G.V. Candler, and H.G. Hornung. „Analysis of thermochemical nonequilibrium models for carbon dioxide flows“. In: *AIAA journal* 31.12 (1993), pp. 2255–2262 (cit. on p. 19).

[34] Z.C. Zhang, S.T.J. Yu, and S.C. Chang. „A space-time conservation element and solution element method for solving the two-and three-dimensional unsteady Euler equations using quadrilateral and hexahedral meshes“. In: *Journal of Computational Physics* 175.1 (2002), pp. 168–199 (cit. on p. 29).

[35] S.C. Chang and X.Y. Wang. „Multi-Dimensional courant number insensitive CE/SE euler solvers for applications involving highly nonuniform meshes“. In: *Powered Flight- The Next Century* (2003) (cit. on p. 37).

[36] C.L. Chang. „Three-dimensional Navier-Stokes calculations using the modified space-time CESE method“. In: *AIAA paper* 5818 (2007), p. 2007 (cit. on pp. 37, 55).

[37] R. Chandra. *Parallel programming in OpenMP*. Morgan kaufmann, 2001 (cit. on p. 39).

[38] C.Y. Wen. „Hypervelocity flow over spheres“. PhD thesis. California Institute of Technology, 1994 (cit. on pp. 44, 49–51, 56).

[39] C.Y. Wen and H.G. Hornung. „Non-equilibrium dissociating flow over spheres“. In: *Journal of Fluid Mechanics* 299 (1995), pp. 389–405 (cit. on pp. 45–47, 49–51, 56, 57, 66).

[40] R. K Lobb. *Experimental measurement of shock detachment distance on spheres fired in air at hypervelocities*. Tech. rep. DTIC Document, 1962 (cit. on p. 45).

[41] F. Zander, R.J. Gollan, P.A. Jacobs, and R.G. Morgan. „Hypervelocity shock standoff on spheres in air“. In: *Shock Waves* 24.2 (2014), pp. 171–178 (cit. on pp. 52, 59).

[42] G.V. Candler and R.W. MacCormack. „Computation of weakly ionized hypersonic flows in thermochemical nonequilibrium“. In: *Journal of Thermophysics and Heat Transfer* 5.3 (1991), pp. 266–273 (cit. on p. 52).

[43] U. Ghia, K.N. Ghia, and C.T. Shin. „High-Re solutions for incompressible flow using the Navier-Stokes equations and a multigrid method“. In: *Journal of computational physics* 48.3 (1982), pp. 387–411 (cit. on p. 53).

[44] M.J. Zhang, S.T. Yu, and S.C. Chang. „Solving the Navier-Stokes Equaitons by the CESE Method“. In: *42nd AIAA Aerospace Sciences Meeting and Exhibit, Reno, NV, Paper No. AIAA-2004-075* (2004) (cit. on p. 54).

[45] R.J. Hakkinen, I. Greber, L. Trilling, and S.S. Abarbanel. „The interaction of an oblique shock wave with a laminar boundary layer“. In: (1959) (cit. on p. 54).

[46] K. Matsuo, S. Kawagoe, and K. Kage. „The interaction of a reflected shock wave with the boundary layer in a shock tube“. In: *Bulletin of JSME* 17.110 (1974), pp. 1039–1046 (cit. on p. 54).

[47] Y.S. Weber, E.S. Oran, J.P. Boris, and J.D. Anderson. „The numerical simulation of shock bifurcation near the end wall of a shock tube“. In: *Physics of Fluids (1994-present)* 7.10 (1995), pp. 2475–2488 (cit. on p. 54).

[48] P.A. Gnoffo and J.A. White. „Computational aerothermodynamic simulation issues on unstructured grids“. In: *AIAA paper* 2371 (2004), p. 2004 (cit. on pp. 55, 64).

[49] O. Knab, H.H. Frühauf, and E.W. Messerschmid. „Theory and validation of the physically consistent coupled vibration-chemistry-vibration model“. In: *Journal of thermophysics and heat transfer* 9.2 (1995), pp. 219–226 (cit. on pp. 55, 56, 65).

[50] CD-adapco. *STAR-CD Version 3.26 User Manual*. 2005.

[51] S. Kottwitz. *LaTeX Cookbook*. Packt Publishing, 2015.

[52] J. Olejniczak, G.V. Candler, H.G. Hornung, and C.Y Wen. „Experimental evaluation of vibration-dissociation coupling models“. In: *6th Joint Thermophysics and Heat Transfer Conference* (1994).